Next generation lithium ion batteries for electrical vehicles

Next generation lithium ion batteries for electrical vehicles

Edited by
Chong Rae Park

In-Tech
intechweb.org

Published by In-Teh

In-Teh
Olajnica 19/2, 32000 Vukovar, Croatia

www.intechweb.org
Additional copies can be obtained from:
publication@intechweb.org

First published April 2010
Printed in India

Technical Editor: Zeljko Debeljuh
Cover designed by Dino Smrekar

Next generation lithium ion batteries for electrical vehicles,
Edited by Chong Rae Park

p. cm.
ISBN 978-953-307-058-2

Preface

During the last twenty years since the first commercialization of lithium ion batteries (LIBs), there has been ever continuing improvements in their performance, such as specific charge/discharge capacity, cycle stability, and safety, according to the practical demands from various end-uses. As a result LIBs play a key role at present as the heart of mobile electronic appliances, being the representatives of the information era and/or economics. However, it is a situation that newly emerged end-uses of LIBs ranging from cordless heavy duty electrical appliances such as handy drills and mini-robots to electrical vehicles (EVs) and/or hybrid electrical vehicles (HEVs) require much more enhanced performance of LIBs than ever. Particularly, to cope with the global climate change issue, much attention has been being drawn to the realization of EVs and HEVs, which would be eventually possible with the advent of LIBs with both high energy density and high power density. This implies that it is a right time to consider new design concept, based on the fundamental operation principle of LIBs, for the component materials of LIBs, including anode, cathode, and separator. The new design concept can be manifested by a variety of different means, for example either by the modifications on morphology, composition, and surface and/or interface of presently existent component materials or by designing completely new component materials.

There have been numerous excellent books on LIBs based on various different viewpoints. But, there is little book available on the state of the art and future of next generation LIBs, particularly eventually for EVs and HEVs. This book is therefore planned to show the readers where we are standing on and where our R&Ds are directing at as much as possible. This does not mean that this book is only for the experts in this field. On the contrary this book is expected to be a good textbook for undergraduates and postgraduates who get interested in this field and hence need general overviews on the LIBs, especially for heavy duty applications including EVs or HEVs.

The first three chapters are mainly concerned with the performance improvements through modifications of morphology, composition, and surface and/or interface of the existent component materials, and the second three chapters describe the design of component materials of either new type or new composition, and an example of possible application of high performance LIBs: Chapter 1 encompasses the state of the art and suggest desirable future direction of anodes development for electrical vehicles, which was based on the deeper understanding of the operation principle of LIBs, Chapter 2 is concerned with the improvements in the safety and thermo-chemical stability of cathodes, with additional information on various influential factors on the thermo-chemical stability, and Chapter 3 shows how the ionic conductivity of the olefinic separator can be improved via surface modification by plasma grafting. In consecution, Chapter 4 introduces thin film type LIBs

in all-solid-state, Chapter 5 describes a new cathode with NASICON open framework nanostructure, and finally Chapter 6 shows how a high performance LIBs can be successfully used for an energy source for a contact wireless railcar.

I hope people as many as possible would find this e-book very helpful reference in their works, and user friendly accessible on their mobile electronics operated by long life LIBs, which would be a short-term manifestation of the R&D efforts on LIBs described in this book. However, in a long term, all effort to enhance both the energy density and the power density of LIBs would never be stopped until a new energy device, which may be called as 'Capattery' because it has both high power density, indicative of the characteristics of capacitors, and high energy density, the characteristics of LIBs, is developed. Indeed, in relation to this, we are now witnessing numerous researches trying to increase either the energy density of capacitors or the power density of LIBs.

Finally I would like to express my thanks to all the authors who contributed to this book, to colleagues who gave invaluable advice to make this book in good quality and to Mr. Vedran Kordic who managed all the practical problems related with the collection and compilation of articles in due course.

Seoul, Korea
March, 2010

Chong Rae Park

Contents

1

Towards high performance anodes with fast charge/discharge rate for LIB based electrical vehicles

Hong Soo Choi and Chong Rae Park*
Carbon Nanomaterials Design Lab., Global Research Lab,
Research Institute of Advanced Materials,
Seoul National University (Department of Materials Science and Engineering)
Korea

1. Introduction

The increasing environmental problems nowadays, such as running out of fossil fuels, global warming, and pollution impact give a major impetus to the development of electrical vehicles (EVs) or hybrid electrical vehicles (HEVs) to substitute for the combustion engine-based vehicles. (Howell, 2008; Tarascon & Armand, 2001) However, full EVs that are run with electrical device only are not yet available due to the unsatisfied performance of battery. The automakers have thus focused on the development of HEVs, which are operated with dual energy sources, viz. the internal combustion heat of conventional fuels and electricity from electrical device without additional electrical charging process. As a transient type, the plug-in HEVs (PHEVs) are drawing much attention of the automakers since it is possible for the PHEVs to charge the battery in the non-use time. In addition, PHEVs have the higher fuel efficiency because the fuel can be the main energy source on the exhaustion of the battery.

Lithium ion batteries (LIBs) may be the one of the first consideration as an energy storage system for electrical vehicles because of higher energy density, power density, and cycle property than other comparable battery systems (Tarascon & Armand, 2001) (see Figure 1). However, in spite of these merits, the commercialized LIBs for HEVs should be much improved in both energy storage capacities such as energy density and power density, and cycle property including capacity retention and Coulombic efficiency in order to meet the requirements by U.S. department of energy (USDOE) (Howell, 2008) as listed in Table 1.

Figure 2 contrasts, on the basis of 40 miles driving range, the USDOE's performance requirements of the anode in LIBs for PHEVs with the performance of the currently commercialized LIBs (Arico et al., 2005). It is clearly seen that the power density of currently available anodes is far below the DOE's requirement although the energy density has already got over the requirement. Power density is the available power per unit time which is given by the following equation (1).

$$\text{Power density} = Q \times \Delta V \tag{1}$$

Here, Q is charge density (A/kg) which is directly related to the C/D rate, and ΔV is potential difference per unit time (V/s). This equation obviously shows that the higher power density can be achieved when the faster C/D rate is available. Therefore, the focus of the current researches for LIB anodes is on increasing the C/D rate and hence power density without aggravation of cycle property. Thus, we will limit the scope of this review to discussing the state of the art in the LIB anodes particularly for PHEVs.

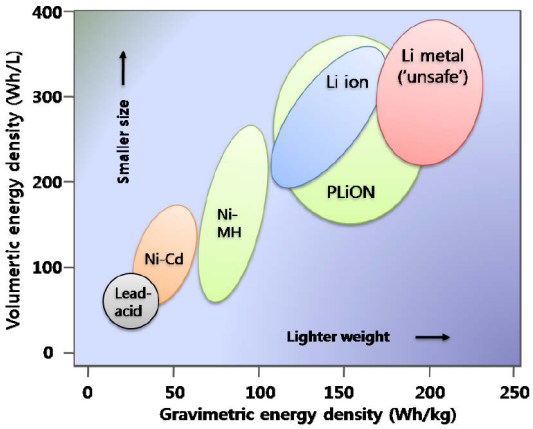

Fig. 1. Comparison of the different battery technologies in terms of volumetric and gravimetric energy density (Tarascon & Armand, 2001).

Characteristics at the End of Life		High Power /Energy Ratio Battery	High Energy /Power Ratio Battery
Reference Equivalent Electric Range	miles	10	40
Peak Pulse Discharge Power (2 sec/10 sec)	kW	50/45	46/38
Peak Region Pulse Power (10 sec)	kW	30	25
Available Energy for CD (Charge Depleting) Mode, 10 kW Rate	kWh	3.4	11.6
Available Energy in Charge Sustaining (CS) Mode	kWh	0.5	0.3
CD Life	Cycles	5,000	5,000
CS HEV Cycle Life, 50 Wh Profile	Cycles	300,000	300,000
Calendar Life, 35°C	year	15	15
Maximum System Weight	kg	60	120
Maximum System Volume	Liter	40	80
System Recharge Rate at 30°C	kW	1.4 (120V/15A)	1.4 (120V/15A)
Unassisted Operating & Charging Temperature	°C	-30 to +52	-30 to +52
Maximum System Price @ 100k units/yr	$	$1,700	$3,400

Table 1. USDOE's battery performance requirements for PHEVs (Howell, **2008**)

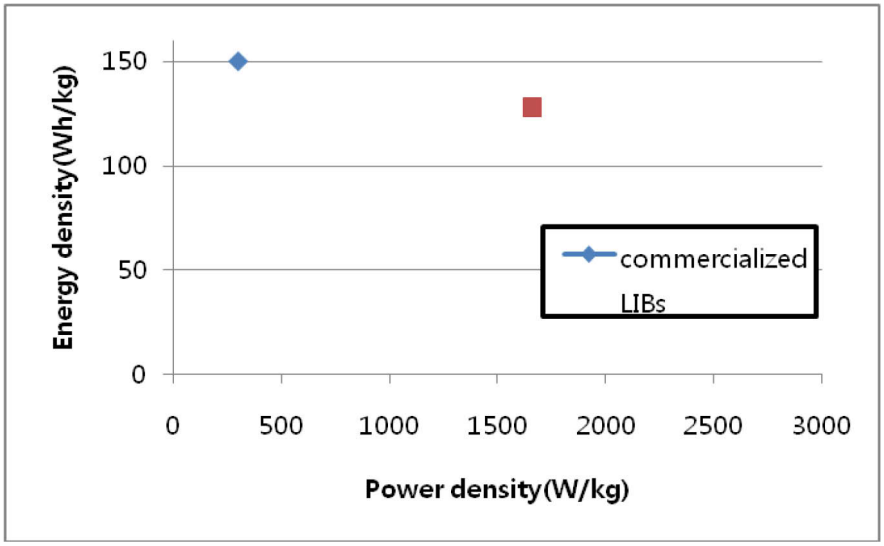

Fig. 2. Energy storage performance of the commercialized LIBs and the USDOE's goal.
*Each energy density and power density of the goal from DOE is calculated on the basis of 40 mile run of PHEVs. The mass of anode is assumed to be 25 % of whole battery mass, and ratio of active material in the anode is assumed to be 80% of anode mass. Working voltage of the batteries is assumed to be 3V.

2. Performance deterioration of the carbon anodes with fast C/D rate

2.1 Performance limitation of carbon anodes for electrical vehicles

The commercial anode material of LIBs is carbon materials, which have replaced the earlier lithium metal and lithium-metal composites, and categorized into graphite, hard carbon and soft carbon with a crystalline state. (Julien & Stoynov, 1999; Wakihara, 2001) Most widely used carbon-based material is graphite that is cheap, and has high Coulombic efficiency and 372 mAh/g of theoretical specific capacity (Arico et al., 2005). The C/D process of the graphite anode is based on the intercalation and deintercalation of Li ions with 0.1~0.2 V of redox potential (Wakihara, 2001). This C/D mechanism can be a basis of the cell safety, because the intercalated Li ions are not deposited on the surface of the graphite anode preventing dendrite formation during charging process. The intercalation of Li ions between graphene galleries provides a good basis for excellent cycle performance due to a small volume change. Also, 0.1~0.2 V of Li^+ redox potential, close to potential of Li metal, contributes to sufficiently high power density for electrical vehicles.

However, as can be seen in Figure 3, untreated natural graphite shows capacity deterioration with increasing cycle numbers, particularly as the charging rate increases. On the application of LIBs to PHEVs, this capacity deterioration with fast C/D rate can be detrimental because the battery should survive fast C/D cycles depending on the duty cyles such as uphill climbing and acceleration of the vehicle.

There have naturally been a variety of researches to overcome the weakness of graphite anode or to find substitute materials for graphites. Before introducing such research activities, below are briefly reviewed the origins of capacity deterioration with fast C/D rate of graphites and/or graphite based composite anodes.

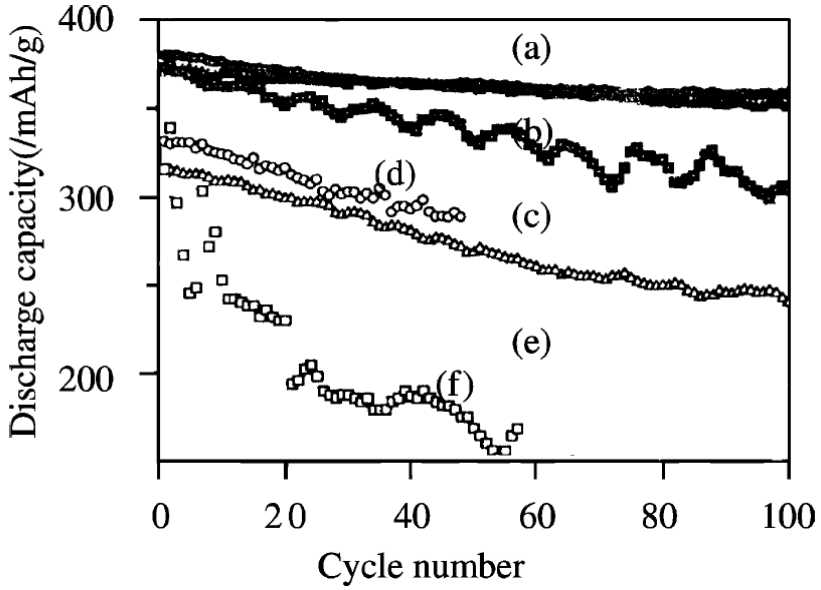

Fig. 3. Cycling performance of natural graphite (curves d, e and f) and Al-treated sample (curves a, b and c): circles, triangles and rectangles represent 0.2 C, 0.5 C and 1 C rate, respectively. (Kim et al., 2001)

3. Origins of performance deterioration of the graphite anode with fast C/D rate

The electrochemical performance of the anode material of LIBs is best described by Nernst equation of half-cell reaction as shown by equation (2). (Bard & Faulkner, 2001) A general half-cell reaction on the surface of the active material of the anode is

$$v_O O + ne \rightleftharpoons v_R R \tag{2}$$

where v_O and v_R are stoichiometric coefficients for oxidant and reductant, respectively, in this reaction. At equilibrium, the energy obtainable from equation (2) is given by the passed charge times the reversible potential difference. Therefore, the reaction on the surface of the active material in the anode is described by equation (3)

$$\Delta G = -nFE \tag{3}$$

where ΔG is Gibbs free energy of the reaction, n is the number of the passed electrons per reacted Li atom, F is the charge of a mole of electron (about 96500 C), and E is electromotive force (emf) of the cell reaction. This equation highlights the kinetic nature of electron transportation, being expressed by E of the electrostatic quantity, and the thermodynamics nature of redox reaction of Li ions, ΔG.

Based on equation (2), the following equation (4) can be developed.

$$E_{anode} = E_{anode}^{0} - \left(\frac{RT}{nF}\right) \ln \frac{A_{anodic}}{A_{cathodic}} \quad (4)$$

Here, E_{anode} and E_{anode}^{0} are the anode half-cell potential and standard half-cell potential, respectively, R is the ideal gas constant (8.314 J/molK^{-1}), and A_{anodic} and $A_{cathodic}$ are the chemical activities of anodic and cathodic reactions, respectively.
The C/D process of LIBs, as shown in Figure 4, includes (1) the redox reactions on the surface of the electrodes and (2) charge (including both ions and electrons) transfer process.

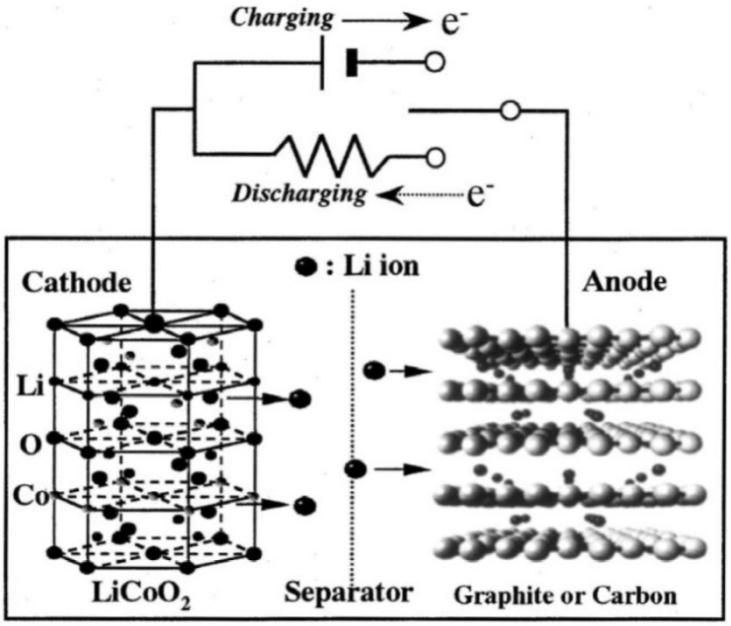

Fig. 4. Charging-discharging mechanism of Li ion secondary battery (Endo et al., 2000).

Basically, based on generally accepted assumption of negligible mass transfer in the electrolyte due to the presence of excess supporting electrolytes in the LIBs, the rate of charge transfer on the surface of the electrode can be generally described with the Butler-Volmer equation (Bard & Faulkner, 2001; Julien & Stoynov, 1999) (equation 5) that contains the natures of both electrons and ions although the detail mechanism is slightly different with kinds of active materials: for example, diffusion and intercalation of Li ions for graphite (Endo et al., 2000) whereas diffusion and alloying for elemental metals (Tarascon & Armand, 2001).

$$i = i_0 \left[e^{\alpha_O f\eta} - e^{-\alpha_R f\eta} \right] \quad (5)$$

where i_0 is exchange current, which indicates the zero net current at equilibrium with Faradaic activity, α_O and α_R are transfer coefficient of oxidation and reduction reactions, respectively, indicating the symmetry of the energy barrier, f=F/RT (F : Faraday constant), and η (=E-E_{eq}) is overpotential, being the measure of the potential difference between thermodynamically determined potential at equilibrium (E_{eq}) and experimentally measured redox potential (E) due to electrochemical reaction with electrons and ions.
The equation itself shows clearly that to enhance C/D performance of LIB anodes the kinetics of electron and ion transportation on and/or in the anode material should be improved.

3.1 Important factors influencing the C/D performance of LIB carbon anodes

The practical LIB system consists of active materials, e.g. graphites, conducting materials, e.g. carbon black, and binder materials, e.g. polyvinylidenefluoride (PVDFs). In this kind of structure the kinetics of electron and ion transportations is influenced by many different factors. From a viewpoint of electron transportation, the movements of electrons from current collector to active materials and from the surface to the inside the active materials are crucial. In this sense, the electron conductivities of the conductive materials including carbon blacks and active materials connected by the binder including PVDFs become very important factors determining the C/D performance of LIB anodes.
On the other hand, Li ions move from the cathode through electrolytes to the surface and then diffuse into the graphites. It is therefore very important that the electrolytes and the active materials should have excellent ion conductivity to minimize the internal resistance of the cell. However, the ionic conductivity of the electrolyte used in practical LIBs is about 10^{-2} S/cm, which is quite lower value than that of aqueous electrolytes. (Wakihara, 2001) Moreover, as the reduction reaction of Li ions occurs on the surface of the active materials the physico-chemical nature of the active materials is another important influencing parameter on the C/D performance of the LIB anodes.
The fabrication factors of the anode, for example, mixing ratio, thickness of electrode, and etc., can also influence the kinetics of electron and ion transportation because these variables affect the formation of percolation pathway of electrons and/or ions. Indeed, Dominko et al. (2001) showed that good contact between each component materials of the electrode, which was achieved by homogeneous distribution of carbon blacks, is an important factor for the performance of LIBs as shown in Figure 5.
In the case of fast C/D rate circumstance as in electrical vehicles whereby rapid charge transfer occurs, the above-mentioned fabrication variables may become important factors, although those are negligibly small in slow rate C/D process. However, to avoid the diversion of the present review, we will limit our discussion on the influential factors directly related to the active materials themselves.

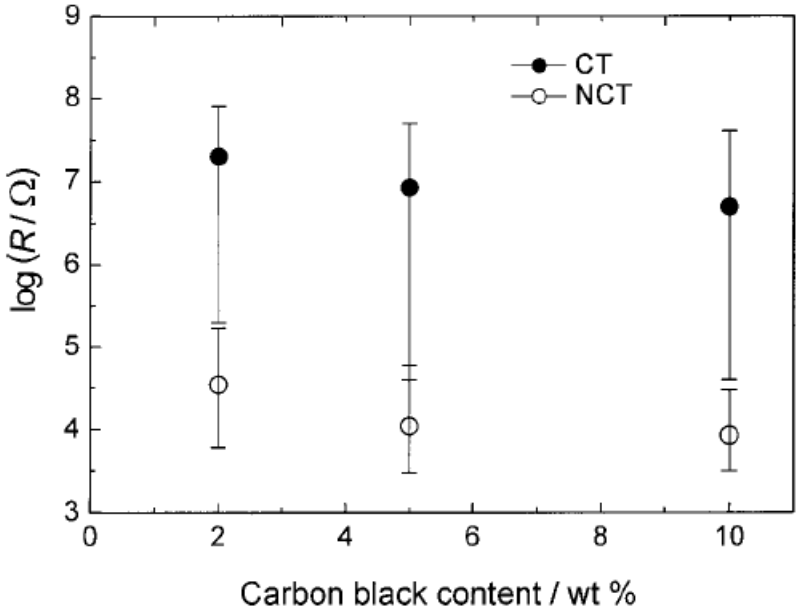

Fig. 5. Dependence of microcontact resistances (R) around active particles on carbon black content. Each bar represents the span of many (10~20) resistance measurements on various particles on the surface of the same pellet. Circles represent average values of the given series. (Dominko et al., 2001)

3.2 Origin of performance deterioration of carbon anodes with fast C/D rates

Despite that a fast rechargeable performance is one of the most important properties required for electrical vehicles the presently available commercialized LIBs show a poor performance in the fast charge/discharge circumstances. For example, the graphite anode shows decay in the specific capacity to ~350 mA/g at over 1C C/D rate (see Figure 3). We will briefly deliberate on the possible origins of this performance deterioration of carbon anodes with fast C/D rates.

3.2.1 Poor electron transportation with fast C/D rates

In the case of fast C/D process, the electron transportation can be influenced by different factors from those for normal or slow C/D rates. For example, poor electron transportation in the anode may arise from three different origins, viz. (1) contact problem between the current collect and the electrode component, (2) low electronic conductivity of the electrode components, and (3) low electronic conductivity of active material.

(1) Poor contact at the interface of the electrode

There are two kinds of the concerned interfaces in the LIB electrodes, viz. the interfaces between the current collect and the electrode components and between the components of the electrode. Since these interfaces play a role of electron transportation pathway, good

contact at the interfaces can lead to excellent cell performance. In particular, under a fast C/D process, there can be a large volume deformation of the active materials, which originates from lithiation and delithiation. If there exists a hysteresis in the volume deformation, then the interfacial contact cannot be ensured, which directly leads to deterioration of the electrode performance. Indeed, as can be seen in Figure 6, this phenomenon is common to the case of elemental metal electrodes, such as Si, Sn, and Sb, even under slow C/D rate circumstances. (Julien & Stoynov, 1999)

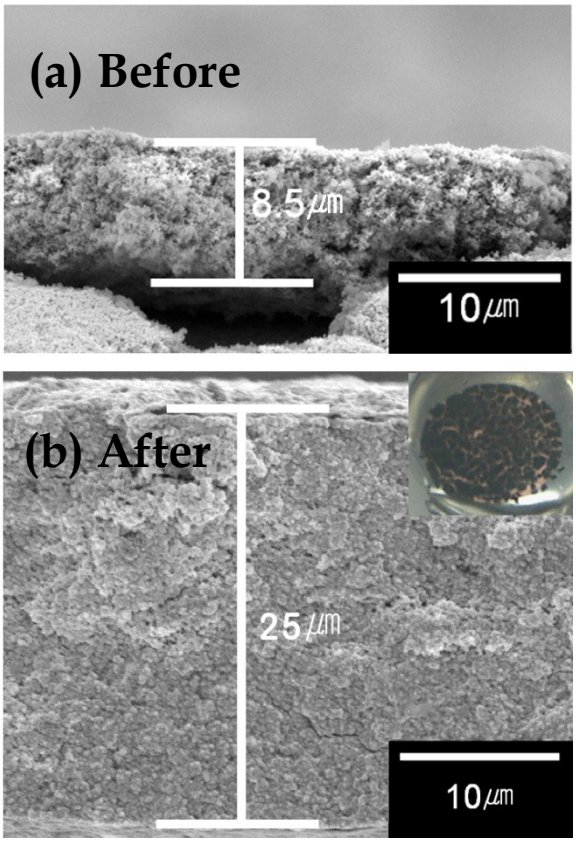

Fig. 6. The volume deformation before (a) and after (b) 1 cycle of C/D process with 50 mA/g charging rate and the resultant cracks (inset of (b)) of the Si-nanoparticle based anode.

In the case of carbon anodes, the volume deformation is not so big as that of metallic anode but still an influential factor of the fast C/D performance. (Yazami, 1999)(also see Figure 3.) Figure 7 illustrates the expansion of the space between graphene sheets during C/D process and the formation of thin film on the surface of graphites due to the deposition of electrolyte decomposition products (Figure 7(b), and the resultant performance deterioration (Figure 7(a)). (Besenhard et al., 1995)

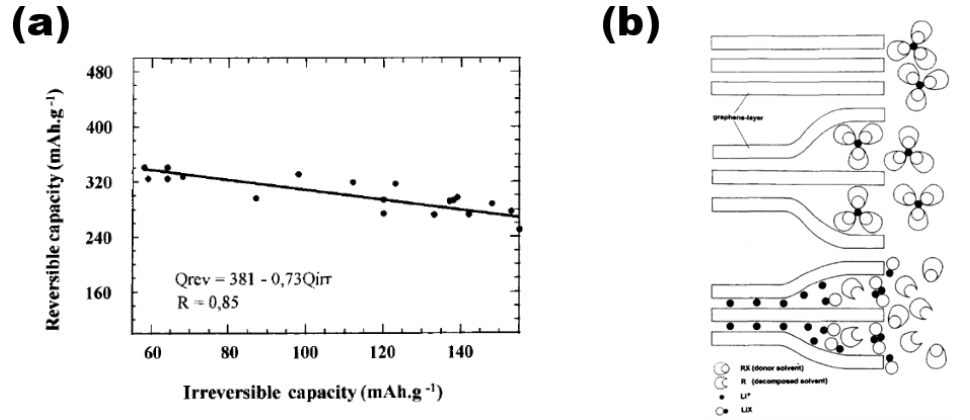

Fig. 7. (a) Q_{rev} vs. Q_{irr} linear dependence for Li/1 M $LiPF_6$; EC(1):DMC(1):DME(2) /Graphite cells under cycle rate of 0.2C at the ambient temperature. (Yazami, 1999) (b) Schematic illustration of the film forming mechanism via decomposition of $Li(solv)_yC_n$. (Besenhard et al., 1995)

(2) Low electronic conductivity of the component materials of carbon anode

The electronic conductivity (κ) of the graphite anode system can be generally described by the following equation (Bard & Faulkner, 2001)

$$\kappa = F\Sigma |z_e| u_e C_e \tag{6}$$

where z_e is the charge of electron, u_e is the mobility of electron, and C_e is the concentration of electron. As predicted by equation (6), the electronic conductivity is directly related to the electron mobility in the system, which varies with many factors such as morphology and surface nature of the active material. In most of commercial carbon anode systems, granular graphites of which electronic conductivity is about 10^{-1}~10^{-4} S/cm are intermixed with conducting carbon blacks of the conductivity of about 10^{-2} S/cm (Brett & Brett, 1993) and polyvyniliden fluorides (PVDFs) that have the conductivity of about 10^{-13} S/cm (Ji & Jiang, 2006). It is therefore necessary to considerably improve the electronic conductivity of the component materials of carbon anodes. Table 2 shows the electronic conductivity of various carbon materials used in the commercialized LIBs.

3.2.2 Poor ionic transportation in the carbon anode with fast C/D rate

As with the issue of electron transportation, the ionic conductivity is a counter factor governing the performance deterioration with fast C/D rate. During C/D process of LIBs, Li ions travel from the cathode via electrolytes to the surface of the anode. The efficiency of the electrode performance is therefore strongly influenced by the efficiency of the charge transfer from one to another component material of the electrode as described by Butler-Volmer equation. Especially, under fast C/D rate conditions, the ions have to transfer fast enough to maximize its partition to the redox reactions on the anode surface. In this sense, the electrolytes should have excellent charge transfer efficiency. Also, after reaching of the

ions to the anode surface, the effective participation of the ions to the redox reaction is governed by the physico-chemical surface nature of the carbon active material.

	Resistivity (Ω.cm)
HOPG (highly ordered pyrrolytic graphite), a-axis	4×10^{-4}
HOPG (highly ordered pyrrolytic graphite), c-axis	0.17
Randomly oriented graphite (Ultracarbon UF-4s grade)	1×10^{-3}
Carbon black (Spheron-6)	0.05

Table 2. Electronic conductivity of various carbon materials (Brett & Brett, 1993)

Basically, the ionic charge flux in an electrolyte can be described by equation (7) because Li ions far away from the electrode migrate by mass transfer mechanism due to almost zero concentration gradient in bulk solution.

$$J_{Li^+} = |z_i| F u_i C_i \frac{d\Phi}{dx} \tag{7}$$

where z_i is the charge of Li ion, F is Faraday constant, u_i is the mobility of Li ion, th term of $F \times u_i = \kappa$ is the ionic conductivity in the electrolyte, C_i is the concentration of Li ions, and $d\Phi/dx$ is the potential difference between the electrodes. That is, in a given LIB system, the Li ion flux depends on the Li ion concentration and the ionic conductivity in the electrolytes. In actual uses of LIBs, excess amount of nonelectroactive supporting electrolyte, for example $LiBF_6$, is being used in order to minimize ionic mass transfer by migration and concurrently to maximize the charge transfer by diffusion. This excess supporting electrolyte helps to decrease the solution resistance and improve the accuracy of working electrode potential, and consequently guarantees an uniform ionic strength irrespective of some fluctuation in the amount of ions. (Bard & Faulkner, 2001) To achieve fast ionic transfer in the electrolyte, it is therefore important to secure a continuous ionic pathway to the surface of active materials in the anode system.

On the surface of the active material, graphite, the kinetics of surface positive charge transfer follows Butler-Volmer equation. This kinetics also follows diffusion migration theory due to the uses of supporting electrolyte and ultramicroelectrode (UME) of small-sized active materials. At a steady state or a quasi-steady state of UMEs, the surface current of UMEs can be described by equation (8). (Bard & Faulkner, 2001)

$$i = nFAm_iC_i \tag{8}$$

Here, A is the surface area of the UME, m_i is the mass transfer coefficient, and C_i is the ionic concentration on the surface of the UME. As the surface area, A, and the mass transfer coefficient, m_i, vary with morphology of UMEs, it is important to control shape and size of the active materials so that the shortest charge diffusion path can be ensured. Indeed, the charge transfer time per each Li ion in the electrode, T, is directly related to the diffusion

path (d_i) as shown in equation (9), being based on the interstitial diffusion. (Bard & Faulkner, 2001; Porter & Easterling, 1991)

$$T = \frac{d_i^2}{\alpha^2 D_i} \tag{9}$$

Here, D_i is the diffusion coefficient of Li ion and α is the number of available vacant interstitial sites in the active material lattice, of which number varies with the micro-structure of the active material.
From the above-mentioned theoretical consideration, we can conjecture two approaches to maximizing ion transportations: one is to ensure effective ionic pathways to the active materials in the anode and the other is to increase the ionic transfer rate on and in the active materials. These two goals can be achieved by (1) morphology control and (2) surface modification of the active materials, and (3) appropriate fabrication to ensure homogeneous distribution and good interfacial contact of conducting materials and the active materials in the anode system. The recently developed nanostructured active materials are expected to be effective for high rate of ionic transfer due to huge 'surface area/volume' ratio and short ionic diffusion path. However, many researches using nanoparticles, for example Si nanoparticles (Wang et al., 2004), proved that this approach is not always working because the nanostructured materials tend to aggregate each other, leading to decreasing of accessible surface areas to electrolytes.

4. Strategies for the material-design of high performance anode with fast C/D rate

In order to achieve good anode performance with fast C/D rate of LIBs for PHEVs, a variety of approaches have been proposed. Below are described the strategies of those researches, most of which are concerned with the aforementioned fundamental issues, viz. the enhancement of electron transportation kinetics and the achievement of high ionic conductivity in the electrode system.

4.1 To enhance the kinetics of electron transportation

The works on the enhancement of electron transportation kinetics can be categorized into three groups: one group is on the morphology control of active materials, another on the surface modification of active materials, and the other on the synthesis of hybrid and/or composite anode materials.

4.1.1 Morphology control of the active materials

To have short diffusion path and high transportation rate of electrons without substitution or additional treatment of the active material, morphology control techniques have been adopted (Chan et al., 2008; Cho et al., 2007; Fang et al., 2009; Hu et al., 2007; Kim et al., 2006; Lampe-Onnerud et al., 2001; Park et al., 2007; Subramanian et al., 2006; Takamura et al., 1999; Tao et al., 2007; Wang et al., 2009; Wang et al., 2008; Zaghib et al., 2003) to fabricate 1D fibrous structures, 2D sheets or films, and 3D porous or specified structures of the active material (Tao et al., 2007). The commercialized graphites are of spherical shape whereby 2D-

laminate structure works for intercalation of Li ions in C/D process. (Endo et al., 2000; Tarascon & Armand, 2001; Wakihara, 2001; Wu et al., 2003) In recent, extensive researches have been expended to finding possible ways of utilizing graphenes as a new class of 2D structure anode material due to its impressive electrical properties. (Makovicka et al., 2009; Nuli et al., 2009; Wang et al., 2009; Yoo et al., 2008)

Generally, 1D fibrous structure is considered an effective system which strengthens the interfacial contacts in the anode system. (Cho et al., 2007; Kim et al., 2006; Xia et al., 2003) For instance, silicon nanowires directly grown on the current collector can enhance the LIBs anode performance under high C/D rates. Figure 8 illustrates that the 1D Si nanowires have the capacity of about 2000 mAh/g even at 1C rate (about 4200 mA/g of C/D rate), arising from the efficient electron pathway secured from good interfacial contact between 1D Si nanowires and the current collector. (Chan et al., 2008) The carbon nanofiber network was also found to exhibit good anodic performance at high C/D rates, (Kim et al., 2006) which originates from good interfacial contacts between the component materials of the anode system and also between the active materials ensuring effective electronic conductivity.

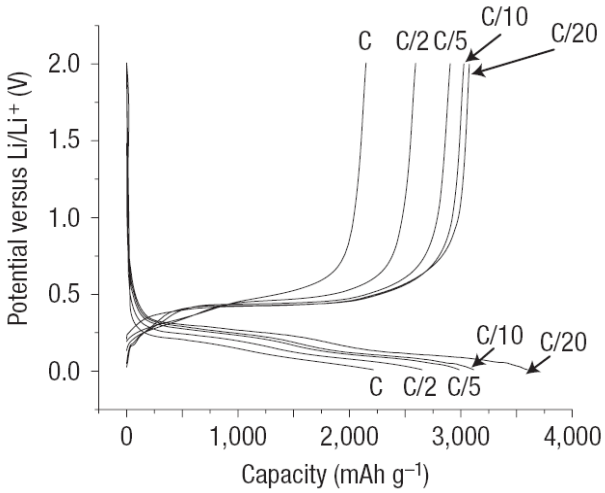

Fig. 8. The voltage profiles of Si nanowires at various C/D rates. (Chan et al., 2008)

In recent, representative 2D carbon structure, graphenes are receiving spot lights due to a large surface to volume ratio and high conductivity. Wang et al. (2009) synthesized graphene nanosheets by reducing graphite oxide and tested anodic performance under 1C C/D rate (about 700 mA/g). The graphene anode indeed exhibited excellent anodic performance at high C/D rate, viz. about 460 mAh/g of reversible specific capacity until 100th cycle as shown in Figure 9.

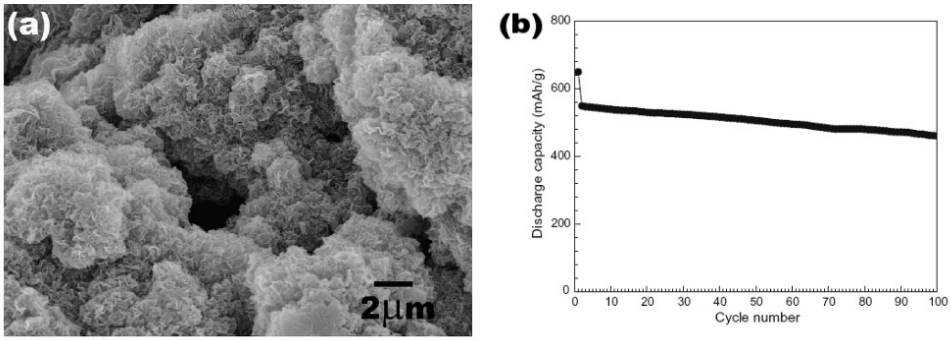

Fig. 9. FE-SEM image of loose graphene nanosheets (a) and discharge capacity (lithium storage) of graphene nanosheet electrode as a function of cycle number at 1C (about 700 mA/g). (Wang et al., 2009)

As for 3D structured anode materials (Tao et al., 2007), porous 3D structure was reported to be helpful to connect the electron pathway effectively. (Long et al., 2004) For example, hierarchical porous carbon structure showed very impressive anodic performance at high C/D rate (Hu et al., 2007) (see Figure 10). This level of anodic performance at high C/D rate is thought to be possible due to good electron pathway and effective Li ions transport via channel-like pores.

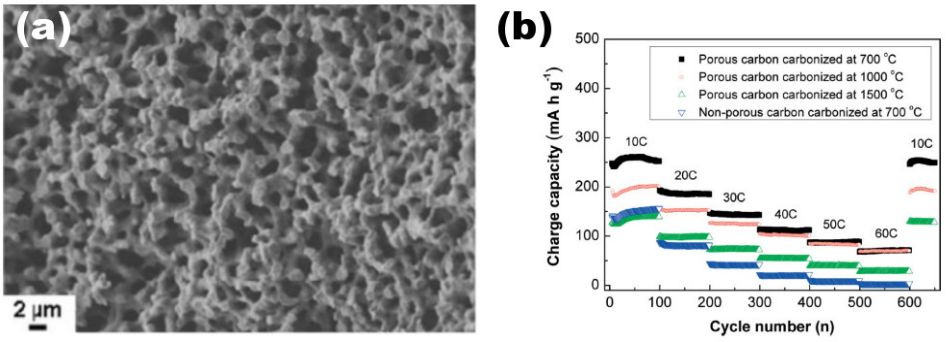

Fig. 10. SEM image of nanocast carbon (carbonized at 700 °C) replica (a) and rate performance of the porous carbon samples carbonized at different temperatures and non-porous carbon from mesophase pitch (carbonized at 700 °C). (Hu et al., 2007)

4.1.2 Surface modifications of active materials

Another way of enhancing electron transportation in the anode system is through surface modifications which are categorized into two groups: one is to coat conducting material on to the surface of the active materials and the other is to dope heteroatoms into metallic oxide anodes to increase electronic conductivity.

(1) Coating of conducting material

To coat conducting material is one of the most widely used surface modifications to enhance the high rate capability of the LIBs anode materials. There are two kinds of mainly adopted conducting materials, viz. carbon materials (Dominko et al., 2007; Kim et al., 2009; Kim et al., 2009; Lou et al., 2009; Sharma et al., 2003; Wang et al., 2007; Zhang et al., 2008) and various metals and their oxides (Choi et al., 2004; Fu et al., 2006; Guo et al., 2002; Kottegoda et al., 2002; Nobili et al., 2008; Takamura et al., 1999; Veeraraghavan et al., 2002; Wang et al., 2003; Zhang et al., 2007), such as Al, Au, Ag, Co and Cu. In the case of carbon materials, hydrothermal reaction and gas phase reaction of various organic carbon precursors, for instance, citrate (Dominko et al., 2007), sugar (Wang et al., 2007), glucose (Zhang et al., 2008), ethylene glycol (Kim et al., 2009), Super P MMM carbon (Sharma et al., 2003), and propylene(Kim et al., 2009), have been used to introduce the carbon coating on the surface of the active materials. In the case of metal coating, CVD method and evaporation method have been mainly used due to easy controllability of the properties of the coated metals.

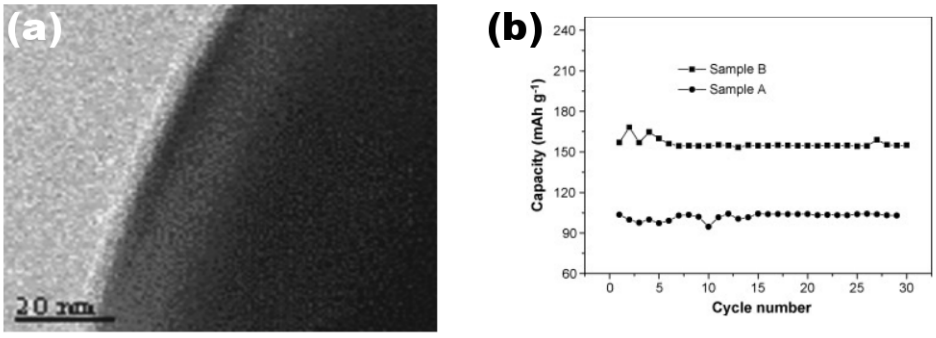

Fig. 11. TEM image of carbon-coated (a) and the relationship of the reversible capacity of the virgin (sample A) and carbon-coated $Li_4Ti_5O_{12}$ (sample B) at 0.1 C with cycle number (b). (Wang et al., 2007)

Carbon coating has been usually applied to metal or metal oxide anodes to give good electronic conductivity and stability as well as barrier property to the formation of SEI layer (Cui et al., 2007; Derrien et al., 2007; Zhang et al., 2008). For example, $Li_4Ti_5O_{12}$ has been considered as an attractive anode candidate for HEVs or EVs because of stable theoretical specific capacity of approximately 170 mAh/g and zero strain and negligible volume deformation during C/D process. This material exhibits however poor C/D performance at high rates due to very low electronic conductivity of about 10^{-13} S/cm (Dominko et al., 2007). The carbon coating on this $Li_4Ti_5O_{12}$ increased twice as high as the specific capacity at 0.1C C/D rate than uncoated one (see Figure 11). The carbon-coated SnO_2 nanospheres also

showed much enhanced specific capability of 200 mAh/g at 3000 mA/g C/D rate. (Lou et al., 2009) In this case, carbon layer additionally prevented volume expansion of SnO_2 by over 250 %.

Metal coating guarantees the faster charge transfer on the surface of the active materials due to high electronic conductivity of metals. In addition, SEI layers on the coated metals, especially, Cu and Sn, have lower resistivity and higher Li ion de-solvation rate. (Nobili et al., 2008) Therefore, metals have been used to coat graphites or other metals. For example, when a commercial graphite anode was coated with silver and/or nickel, the C/D performance of the anode at high charging rate was improved together with much enhanced discharge capacity as can be seen in Figure 12. (Choi et al., 2004)

(a)

	Elemental analysis (wt.%)		BET surface area (m^2/g)
	Ag (wt.%)	Ni (wt.%)	
S0	–	–	1.9923
S1	2.67	–	2.7650
S2	5.22	–	3.7522
S3	–	2.46	4.7694
S4	1.18	1.11	3.6809

S0: raw synthetic graphite (MCMB); S1: 2.67 wt.% of silver-coated graphite; S2: 5.22 wt.% of silver-coated graphite; S3: 2.46 wt.% nickel-coated graphite S4: 1.18 wt.% of silver and 1.11 wt.% of nickel-coated graphite. Heat treatment temperature was the same for the all samples.

(b)

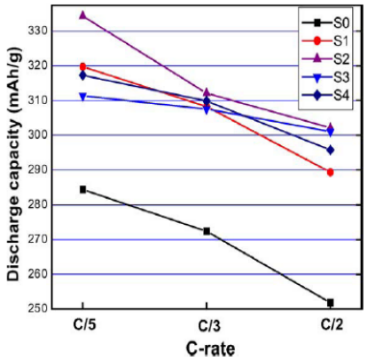

Fig. 12. Elemental analysis and BET surface area of metal-coated graphites (a) and effect of metal-coated graphites on maximum discharge capacity at various C-rates. 1M $LiPF_6$ in EC:EMC:DMC (1:1:1) (Choi et al., 2004)

(2) Doping methods

Doping heteroatoms into metal oxide and/or graphite anodes is another effective way to increase electronic conductivity (Chen et al., 2001; Coustier et al., 1999; Endo et al., 1999; Huang et al., 2005; Li et al., 2009; Miyachi et al., 2007; Park et al., 2008; Qi et al., 2009; Santos-Pe et al., 2001; Wen et al., 2008; Zhao et al., 2008) of the LIB anode materials. This surface modification turned out effective particularly for improving the electronic conductivity of metal oxide materials, such as SnO_2 (Santos-Pe et al., 2001), SiO (Miyachi et al., 2007), $Li_4Ti_5O_{12}$ (Chen et al., 2001; Huang et al., 2005; Li et al., 2009; Park et al., 2008; Qi et al., 2009; Wen et al., 2008; Zhao et al., 2008), V_2O_5 (Coustier et al., 1999), and etc, via increased charge carrier density and hopping probability of electrons. Indeed, N-doped $Li_4Ti_5O_{12}$, which was prepared by heat treating $Li_4Ti_5O_{12}$ under NH_3 atmosphere to introduce conductive TiN thin film on the surface, exhibited much enhanced anode performance at high C/D rate as can be seen in Figure 13. (Park et al., 2008) In the various metal (Fe, Ti, Ni)-doped SiO anodes the doped metal formed effective electron conductive path on the active material, which helps fast reversible redox reaction between Si^{4+} and Si at high C/D rates. (Miyachi et al., 2007)

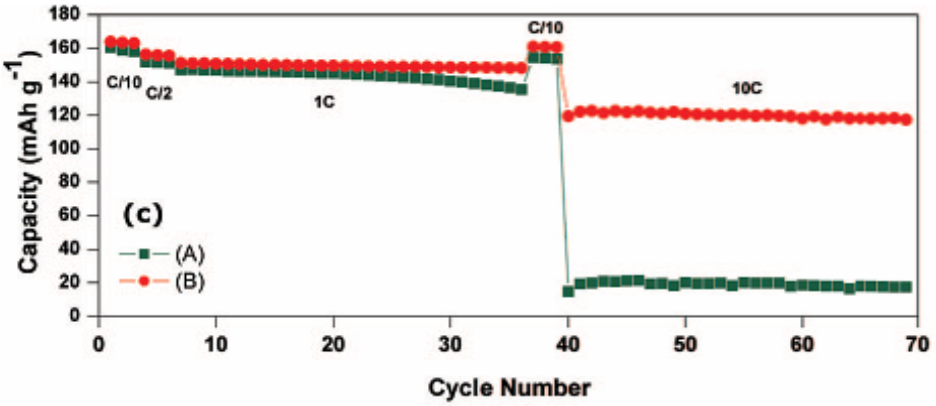

Fig. 13. Reversible capacities of (A) pristine and (B) 10 min-nitridated $Li_4Ti_5O_{12}$ with different charge/discharge current densities during cycling. (Park et al., 2008)

4.1.3 Synthesis of composite active material

The synthesis of composite anode materials has been most commonly adopted to overcome drawbacks of the current LIB anodes, for example, suppression of large volume expansion. (Tarascon & Armand, 2001) This approach was found also effective in enhancing the electron transportation rate. The approaches to synthesizing composites can be categorized into three groups: one is the carbon based composites (Chao et al., 2008; Cui et al., 2009; Gao et al., 2007; Hanai et al., 2005; Ji & Zhang, 2009; Lee et al., 2008; Lee et al., 2000; Lee et al., 2009; Li et al., 2009; Park et al., 2006; Park & Sohn, 2009; Park et al., 2007; Skowronski & Knofczynski, 2009; Veeraraghavan et al., 2002; Wang et al., 2008; Wang et al., 2008; Wen et al., 2008; Wen et al., 2003; Yao et al., 2008; Yin et al., 2005; Yoon et al., 2009; Yu et al., 2008; Zheng et al., 2008), another is the metallic composites (Ahn et al., 1999; Guo et al., 2007; Guo et al., 2009; Hanai et al., 2005; Hibino et al., 2004; Huang et al., 2008; Huang et al., 2005; Vaughey et al., 2003; Wang et al., 2008; Yan & et al., 2007; Yang et al., 2006; Yin et al., 2004; Zhang et al., 2009), and the other is the composites incorporated with conductive addictives.

(1) Carbon based composites

The carbon based composites are of two types: the composite with carbon active material (Cui et al., 2009; Ji & Zhang, 2009; Lee et al., 2000; Park et al., 2006; Park & Sohn, 2009; Park et al., 2007; Skowronski & Knofczynski, 2009; Veeraraghavan et al., 2002; Wang et al., 2008; Wang et al., 2008; Yao et al., 2008) and the composite with carbon conductive material (Chao et al., 2008; Gao et al., 2007; Hanai et al., 2005; Hibino et al., 2004; Lee et al., 2008; Lee et al., 2009; Li et al., 2009; Wen et al., 2008; Wen et al., 2003; Yin et al., 2005; Yoon et al., 2009; Yu et al., 2008; Zheng et al., 2008). In the former case, other conductive materials are used to enhance the electron transportation. If such conductive materials are active with Li ions, like as Co (Wang et al., 2008), Sn (Lee et al., 2000; Park & Sohn, 2009; Veeraraghavan et al., 2002), Sb (Park & Sohn, 2009; Park et al., 2007) and Fe_3O_4 (Cui et al., 2009; Wang et al., 2008), the conductive materials can also play a role as the active material with carbon. As an example of the composite with carbon active material, Wang et al. (2008) prepared a composite of carbon fiber/Fe_3O_4 using electrospinning technique. Because Fe_3O_4 has high theoretical

specific capacity of 924 mAh/g and high electronic conductivity, the composite exhibited the specific capacity of about 1000 mAh/g at 200 mA/g of C/D rate.
On the other hand, in the latter case, carbon materials are usually coated on and/or incorporated into the matrix of metallic or insulating or semiconducting active materials. For carbon-coated metal composites, carbon is used as a matrix or template to suppress the volume expansion of and maintain electron pathways in the anode. In this case, metal is the anodic active material, and at the same time, enhance the electron transportation of the carbon material. Indeed, SnSb/C composites synthesized by Park and Sohn (2009) using high energy mechanical milling show the reversible specific capacity of 500 mAh/g over at 2C rate due to enhanced electronic conductivity by SnSb nanocrystallines (see Figure 14)

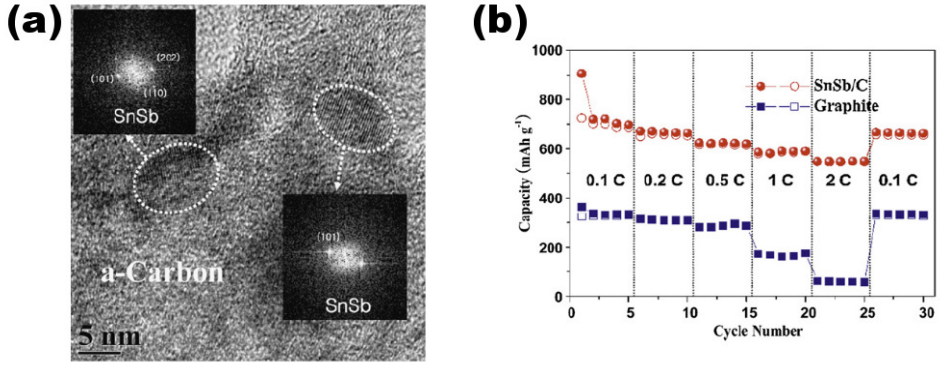

Fig. 14. TEM image with the corresponding lattice spacing of the SnSb/C nanocomposite (a) and the discharge and charge capacity vs. cycle number for the SnSb/C nanocomposite and graphite (MCMB) electrodes at various C rates (SnSb/C: 1C-700 mA/g, graphite: 1C-320 mA/g). (Park & Sohn, 2009)

The carbon-coated insulating materials that have high storage capacity of Li ions, for example, Si (Hanai et al., 2005; Wen et al., 2003), SiO (Chao et al., 2008), $Li_4Ti_5O_{12}$ (Yu et al., 2008), and etc. also show much enhanced anodic performance due to improved electronic conductivity by carbon component in the composite. Indeed, SiO/carbon cryogel (CC) composites showed the specific discharge capacity of 450 mAh/g over at 600 mA/g of C/D rate. This enhanced anodic performance at high C/D rate was attributed to high electronic conductivity and continuous porosity giving increased porosity and improved contact with electrolytes. (Hasegawa et al., 2004) On the other hand, the carbon-incorporated composite system whereby carbon addictives, for example carbon nanotube (CNT) (Lee et al., 2008; Lee et al., 2009; Yin et al., 2005; Zheng et al., 2008), are incorporated into metal oxide system is another simple way to enhancing the electron transportation in the anode system. In this case, there are no additional treatments that may influence the anodic performance of the oxide materials, so this method can thus be applied to the thermally sensitive anode materials. Zheng et al. (2008) used CNTs to increase the high rate performance of CuO anode. As CNTs have high chemical stability, large surface area, strong mechanical strength, and high electronic conductivity, they integrated CNTs and CuO into nanomicrospheres to have enhanced performance at fast C/D rates as shown in Figure 15.

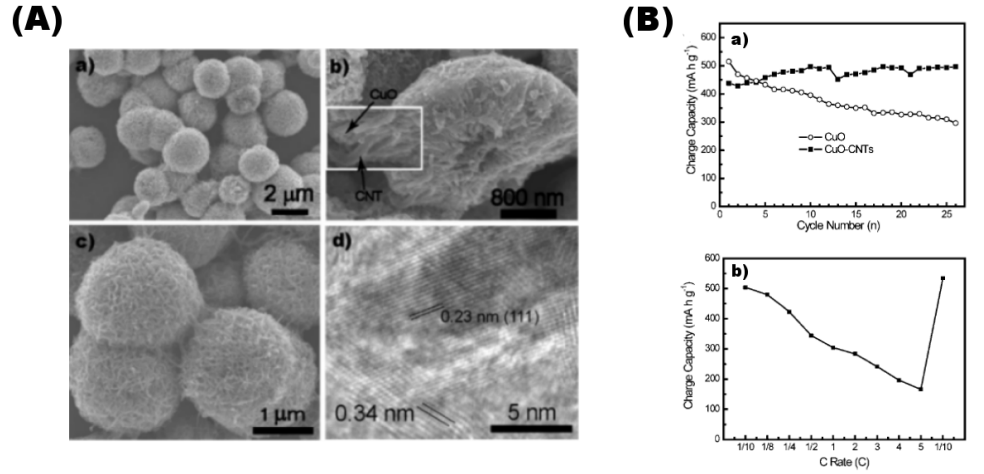

Fig. 15. (A) (a, c) SEM images of CuO-CNT nanomicrospheres and (b) crashed CuO-CNT nanomicrosphere, (d) HRTEM image of CuO-CNT nanomicrospheres. The inset in (b) shows the CuO crystals and the inserted CNTs. (B) (a) variation in charge capacity with cycle number for CuO and CuO-CNT nanomicrospheres at a rate of 0.1C. (b) C/D rate performance of CuO-CNT nanomicrospheres. (Zheng et al., 2008)

(2) Metallic composites

There are various metals which can alloy with lithium and perform as anode material of LIBs: for example, Sb, Sn, P and Bi as they are have very high specific capacity of Li ions, but very poor cycle performance due to large volume expansion. (Park & Sohn, 2009) As this huge volume change during C/D process in the anode material causes cracks and disintergration that cause poor electronic contact, (Kasavajjula et al., 2007; Ryu et al., 2004) the metallic composites have been studied to overcome such problems. The composites can be prepared through one of the following reactions:

$$AB + xLi^+ + xe^- \leftrightarrow Li_xA + B$$
$$AB + xLi^+ + xe^- \leftrightarrow Li_xAB$$

With the composites synthesized via the first reaction, the component B that is not reactive with Li ions provides a buffer for the huge volume expansion of component A, caused by alloying with Li ions. (Tarascon et al., 2003; Wachtler et al., 2002) Also, the component B can enhance the charge transfer reaction on the surface of the active materials due to high electronic conductivity. In the case of the composites obtained from the second reaction, both A and B components can conduct as active materials. After a few cycles, this reaction results in the first reaction. (Gillot et al., 2005; Souza et al., 2002) Hence many researches utilized this reaction to enhance the high rate capability of the metallic composites as an anode of LIBs. (Guo et al., 2007; Guo et al., 2009; Hanai et al., 2005; Park & Sohn, 2009; Vaughey et al., 2003; Yan & et al., 2007; Yin et al., 2004) For instance, Guo et al. (2009) introduced nickel/tin composites via reduction reaction and calcinations, which demonstrated the enhanced anodic performance at high C/D rates (see Figure 16).

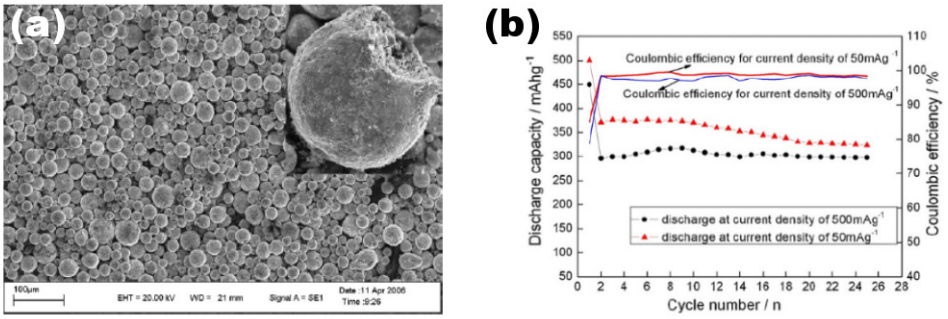

Fig. 16. SEM image of $NiSn_x$ alloy composites (a) and cycling performance of $NiSn_x$ alloy composites at different current densities (b). (Guo et al., 2009)

The metallic additives can also be used to increase the electronic conductivity of insulating or semiconducting metal oxide anodes. (Huang et al., 2008; Huang et al., 2005; Zhang et al., 2009) Thorugh the incorporation of nanostructured metals into the anode matrix with low electronic conductive can effectively enhance the electron transportation due to the intrinsically high electronic conductivity of the additive metals. (Ahn et al., 1999; Yang et al., 2006)

4.2. To achieve high ion transportation

As aforementioned, high and rapid ion transfer in the anode system can be achieved by introducing good ionic pathway to the active materials and increasing the ionic transfer rate on and in the active materials by achieving large surface area (A), good ionic transfer property (m_i), and short ionic pathway in the active material (d_i) through morphology control and surface modification of the active materials.

4.2.1 Morphology control of active materials

The main objectives of morphology control are to introduce continuous ionic pathways to the surface of the active materials by increasing accessible areas to electrolytes and decreasing the ionic diffusion path inside the active materials. Various nanostructured active materials have thus been studied, such as 0D-hollow spheres (Guo et al., 2009; Kim & Cho, 2008; Liu et al., 2009; Tang et al., 2009; Wang et al., 2007; Xiao et al., 2009; Zhou et al., 2009), 1D-tubular or rod-like structures (Adelhelm et al., 2009; Chan et al., 2008; Fang et al., 2009; Li et al., 2009; Park et al., 2007; Qiao et al., 2008; Subramanian et al., 2006; Wang et al., 2005; Wen et al., 2007), 2D-nanosheets (Graetz et al., 2004; Ohara et al., 2004; Tang et al., 2008), and 3D-porous structures (Guo et al., 2007; Hu et al., 2007; Liu et al., 2008; Long et al., 2004; Singhal et al., 2004; Yu et al., 2007; Zhang et al., 2009).

The 0D-hollow spheres have characteristics of large surface area, low density, and short diffusion path inside the active material. (Zhou et al., 2009) In contrast to filled 0D-nanosphere, the hollow spheres provide sufficient accessible areas to electrolytes even with the aggregated forms. Moreover the inner empty space plays a role as a buffer to the volume expansion of the active materials. For example, the vesicle-like hollow spheres of

V_2O_5/SnO_2, prepared by Liu et al. (2009), exhibited the specific capacity of 673 mAh/g at 250 mA/g C/D rate even after 50th cycling (see Figure 17).

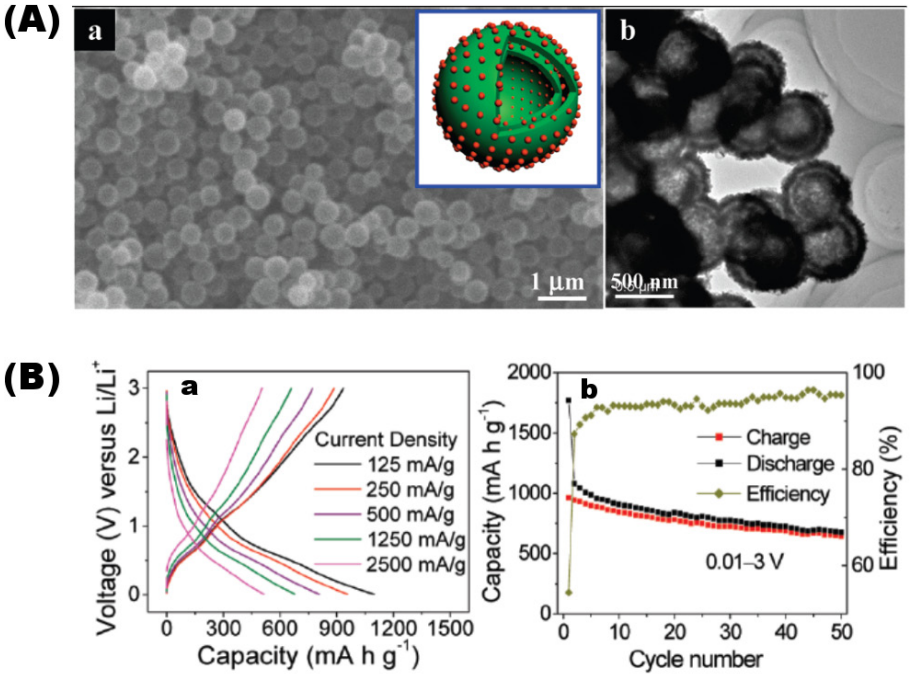

Fig. 17. SEM micrographs of V_2O_5-SnO_2 vesicle-like nanocapsules (The inset is a schematic structure of the nanocapsule. The red spheres represent SnO_2 nanocrystals, and the green double shells represent V_2O_5 matrix) (A-a). Low-magnification TEM image of V_2O_5-SnO_2 nanocapsules (A-b). Charge/discharge curves at different current densities (B-a). Capacity (left) and efficiency (right) versus cycle number at a current density of 250 mA/g (B-b). (Liu et al., 2009)

Tubular and/or rod-like 1D nanostructured materials are also effective in increasing accessible surface area and reducing the ion diffusion path. Especially, an array of 1D nanostructured anodes can be effectively introduced on a plate using AAO or anodizing method. (Xia et al., 2003) This structure is very effective to preventing aggregation of nanostructured materials and hence increasing the electrolyte-accessible surface areas. (Chan et al., 2008) In the case of tubular structure, vacancy plays the same role as in the hollow spheres. Indeed, an array of TiO_2 directly grown on a plate by Fang et al. (2009) using anodic oxidation method exhibited the specific capacity of 140 and 170 mAh/g at 10 and 30 A/g of C/D rates, respectively, as shown in Figure 18.

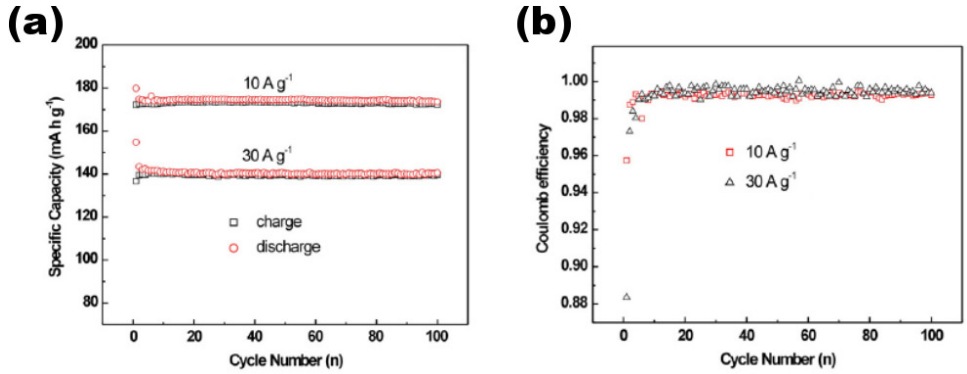

Fig. 18. Cycle performance (a) and Coulomb efficiency (b) of an array of 1D TiO_2 electrode at current densities of 10 and 30 A/g. (Fang et al., 2009)

The 2D nanostructured anodes, viz. of sheet or thin-film type, have drawn much attention with an expectation of increasing surface area. However, this type of structure exhibited poor anodic performance at high C/D rate. In some cases, 2D nanosheet structure was used as a platform to introduce 3D porous structure. (Tang et al., 2008) In the case of 3D porous structure, it is very important to introduce a continuous phase of porosity for effective ionic pathways to the surface of the active material. Most of 3D porous structures with continuous pore phase can be prepared via chemical reactions including sol-gel reaction, CVD, and electrodeposition, which are conducted under controlled conditions. When combined with template techniques such as porous membranes, colloidal crystals, micelles, and etc., these chemical reactions allow the formation of hierarchical network structure with size-controlled continuous pore phase. (Long et al., 2004) Yu et al. (2007) recently reported that Li_2O–CuO–SnO_2 composites with porous spherical multideck-cage morphology show the specific capacity of 800 mAh/g over at 1C C/D rate (see Figure 19).

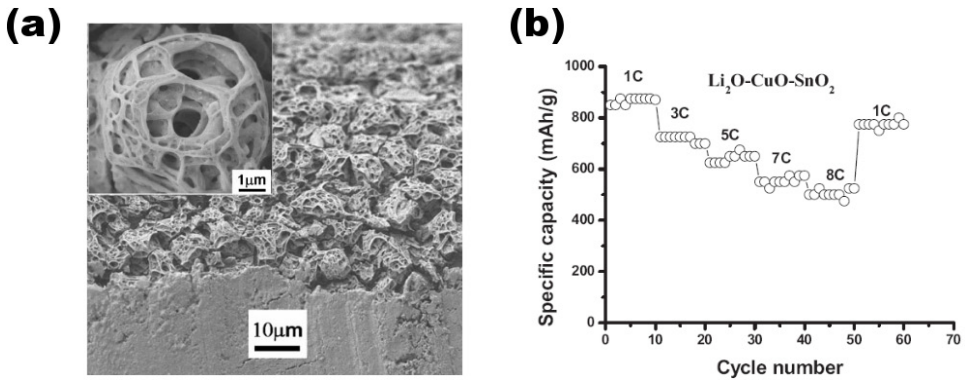

Fig. 19. SEM micrographs of as-deposited Li_2O–CuO–SnO_2 (a) and cycle performance results at various C/D rates(b). (Hu et al., 2007)

4.2.2 Surface modification of the active materials

Positive charge transfer property of the surface of the active material is another essential factor to enhance the ionic transportation. High rate positive charge, Li ions, transfer can be achieved by increasing mass transfer coefficient, which varies with the morphologies of the anode materials. To modify the surface of the active material, doping and/or encapsulation methods are widely adopted. For example, Mo doped MnV_2O_6 ($Mn_{1-x}Mo_{2x}V_{2(1-x)}O_6$ (x = 0, 0.4)) prepared by Hara et al. (2002) using conventional solid-state reaction showed the specific capacity of about 1000 mAh/g at 1C (350 mA/g) C/D rate, which is higher by 200 mAh/g over than the pristine MnV_2O_6 sample (Figure 20). This improvement was possible because Mn vacancies introduced by Mo doping (Kozlowski et al., 1980) can enhance the Li ion diffusion on the surface of MnV_2O_6.

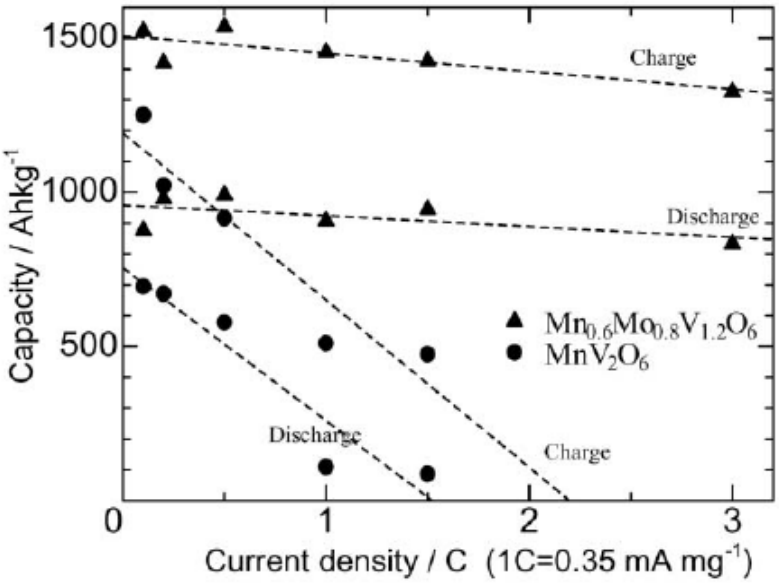

Fig. 20. Variation of charge-discharge capacity of $Mn_{1-x}Mo_{2x}V_{2(1-x)}O_6$ (x = 0, 0.4) with current density. (Hara et al., 2002)

Surface encapsulation can also increase the Li ion transfer rate on the surface of the active material. Recently, Kim et al. (2008) introduced cyanoethyl polyvinylalcohol (cPVA)-modified graphites as a fast rechargeable anode material. Generally, graphite is not appropriate active material for fast C/D rate batteries due to intercalation based C/D mechanism and SEI problem during C/D process. Accordingly, they tried to encapsulate the graphite with cPVA to generate an electrolyte-philic surface. These cPVA-encapsulated graphites showed much enhanced high rate capability due to high polar –CN groups in the cPVA, which give high ionic conductivity of around 7 mS/cm.

5. Design guidelines for next generation anode materials for EVs

The currently available carbon anodes have exhibited somewhat limited performance from a viewpoint of their application to EVs. As we discussed earlier, electron transportation can be enhanced by increasing the electronic mobility in the active material (u_e) and securing continuous electron pathways. Also, ion transportation can be improved by fabricating active materials with high mass transfer coefficient (m_i), large accessible surface area (A), short diffusion length (d_i), and continuous ion pathways. When considered all these parameters together, we may be able to imagine desirable microstructure of the high performance anode for EVs as shown in Figure 21 whereby three dimensionally developed porous microstructures of highly electron conductive materials.

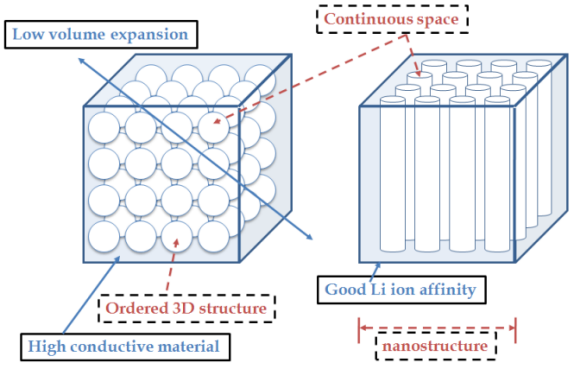

Fig. 21. Schematic of desirable microstructure of next generation high performance anodes for Evs.

In this sense, it is indeed interesting to note recently reported Si nanotubes, which have the ordered 3D porous nanostructure and exhibited the specific capacity of 2800 mAh/g at 1C rate upto 200th cycles due to extremely enhanced Li ion transportation kinetics. (Park et al., 2009) On the other hand, to enhance the affinity and hence transfer rate of Li ions to the surface of the active materials, it is necessary to suppress and/or minimize the formation of solid electrolyte interface (SEI) layer that has been known to deteriorate the cycle performance of carbon anodes (Wang et al., 2001). Indeed, the equation (10), which is the modified Butler-Volmer equation (5), tells that the resistance of SEI layer (R_{SEI}) decreases the driving force of the overpotential (η), leading to decrease of specific capacity in the active materials. One possible way to prevent and/or suppress the formation of SEI layers on the surface of the active materials is to find materials that exhibit Li/Li^+ redox potential window over 0.7 V, which is the formation potential of SEI layer. In recent, $Li_4Ti_5O_{12}$ has been reported to have the Li/Li^+ redox potential at about 1.5 V (Yao et al., 2008) Also, $Li_4Ti_5O_{12}$ has higher Li ion diffusion coefficient than carbon materials, which helps fast ion transportation. (Takai et al., 1999) However, there still remain many issues to be solved for this material, including increasing specific energy density considerably.

$$i=i_0\left[e^{\alpha_O f(\eta-i/R_{SEI})}-e^{-\alpha_R f(\eta-i/R_{SEI})}\right] \quad (10)$$

6. Conclusion

There have been numerous studies on the design and development of novel high performance LIB anodes, which would be applicable to several types of electrical vehicles, HEVs, PHEVs, or full EVs. Then, through a survey of those studies from the viewpoints of the C/D mechanism of Li ions, including currently available carbon based anode systems, we could find that maximizing both ion and electron transportations in the anode system should be most importantly considered in the design and development of novel anodes for HEVs, PHEVs or EVs.

Many different approaches were found to be possible to achieve such goals of the novel anodes, especially with high performance at high C/D rates. That is, both good electron transportation pathways and short ion diffusion pathways can be endowed with the morphology control by adopting various nanotechnologies. In addition, through morphology control, accessible surface areas to electrolytes can be much increased, which leads to much improved anodic performance at high C/D rates. On the other hand, the surface modification of the anode materials through various methods can also contribute to enhancing electron transfer rates on and inside the active materials and ion diffusion rates.

Although there are many novel anode materials that were reported to show high rate capability of LIBs, it still needs further and farther works on design and developing novel anode materials with much higher performance at high C/D rates. However, whatsoever they would be both ion and electron transportation rates should be concurrently maximized. Having been considered the current status of the developed anode materials, much more effort has to be expended to enhancing the ion transportation rate. (Fang et al., 2009; Hu et al., 2006) For the development of novel LIB anode materials with practical significance for EVs or HEVs, other important factors should also be considered, such as safety factors, cost, mass production possibility, and etc.

7. Acknowledgement

This work was supported by the Ministry of Education, Science and Technology, Korea through reseach institute of advanced materials **(RIAM)** and global research laboratory **(GRL)** program.

8. References

Adelhelm, P.; Hu, Y. S.; Antonietti, M.; Maier, J. & Smarsly, B. M. (2009). Hollow Fe-containing carbon fibers with tubular tertiary structure: preparation and Li-storage properties. *Journal of Materials Chemistry*, Vol. 19, No. 11, February 2009, pp. 1616-1620, ISSN 0959-9428

Ahn, S.; Kim, Y.; Kim, K. J.; Kim, T. H.; Lee, H. & Kim, M. H. (1999). Development of high capacity, high rate lithium ion batteries utilizing metal fiber conductive additives. *Journal of Power Sources*, Vol. 81-82, No. September 1999, pp. 896-901, ISSN 0378-7753

Arico, A. S.; Bruce, P.; Scrosati, B.; Tarascon, J. M. & Van Schalkwijk, W. (2005). Nanostructured materials for advanced energy conversion and storage devices. *Nature Materials*, Vol. 4, No. 5, May 2005, pp. 366-377, ISSN 1476-1122

Bard, A. J. & Faulkner, L. R. (2001). *Electrochemical Methods : Fundamentals and Applications*, John Wiley & Sons, Inc., ISBN 0-471-04372-9, Austin

Besenhard, J. O.; Winter, M.; Yang, J. & Biberacher, W. (1995). Filming mechanism of lithium-carbon anodes in organic and inorganic electrolytes. *Journal of Power Sources*, Vol. 54, No. 2, Aprill 1995, pp. 228-231, ISSN 0378-7753

Brett, C. M. A. & Brett, A. M. O. (1993). *Electrochemistry : Principles, Methods, and Applications*, Oxford University Press, ISBN 0-19-855389-7, Oxford

Chan, C. K.; Peng, H. L.; Liu, G.; McIlwrath, K.; Zhang, X. F.; Huggins, R. A. & Cui, Y. (2008). High-performance lithium battery anodes using silicon nanowires. *Nature Nanotechnology*, Vol. 3, No. 1, January 2008, pp. 31-35, ISSN 1748-3387

Chao, Y.-J.; Yuan, X. & Ma, Z.-F. (2008). Preparation and characterization of carbon cryogel (CC) and CC-SiO composite as anode material for lithium-ion battery. *Electrochimica Acta*, Vol. 53, No. 9, March 2008, pp. 3468-3473, ISSN 0013-4686

Chen, C. H.; Vaughey, J. T.; Jansen, A. N.; Dees, D. W.; Kahaian, A. J.; Goacher, T. & Thackeray, M. M. (2001). Studies of Mg-Substituted $Li_{4-x}Mg_xTi_5O_{12}$ Spinel Electrodes (0 <= x <= 1) for Lithium Batteries. *Journal of the Electrochemical Society*, Vol. 148, No. 1, January 2001, pp. A102-A104, ISSN 0013-4651

Cho, H. G.; Kim, Y. J.; Sung, Y. E. & Park, C. R. (2007). The enhanced anodic performance of highly crimped and crystalline nanofibrillar carbon in lithium-ion batteries. *Electrochimica Acta*, Vol. 53, No. 2, December 2007, pp. 944-950, ISSN 0013-4686

Choi, W. C.; Byun, D.; Lee, J. K. & Cho, B. w. (2004). Electrochemical characteristics of silver- and nickel-coated synthetic graphite prepared by a gas suspension spray coating method for the anode of lithium secondary batteries. *Electrochimica Acta*, Vol. 50, No. 2-3, November 2004, pp. 523-529, ISSN 0013-4686

Coustier, F.; Jarero, G.; Passerini, S. & Smyrl, W. H. (1999). Performance of copper-doped V_2O_5 xerogel in coin cell assembly. *Journal of Power Sources*, Vol. 83, No. 1-2, October 1999, pp. 9-14, ISSN 0378-7753

Cui, G.; Hu, Y.-S.; Zhi, L.; Wu, D.; Lieberwirth, I.; Maier, J. & M?len, K. (2007). A One-Step Approach Towards Carbon-Encapsulated Hollow Tin Nanoparticles and Their Application in Lithium Batteries13. *Small*, Vol. 3, No. 12, November 2007, pp. 2066-2069, ISSN 1613-6829

Cui, Z.-M.; Jiang, L.-Y.; Song, W.-G. & Guo, Y.-G. (2009). High-Yield Gas-Liquid Interfacial Synthesis of Highly Dispersed Fe_3O_4 Nanocrystals and Their Application in Lithium-Ion Batteries. *Chemistry of Materials*, Vol. 21, No. 6, February 2009, pp. 1162-1166, ISSN 0897-4756

Derrien, G.; Hassoun, J.; Panero, S. & Scrosati, B. (2007). Nanostructured Sn-C Composite as an Advanced Anode Material in High-Performance Lithium-Ion Batteries. *Advanced Materials*, Vol. 19, No. 17, August 2007, pp. 2336-2340, ISSN 1521-4095

Dominko, R.; Gaberscek, M.; Bele, A.; Mihailovic, D. & Jamnik, J. (2007). Carbon nanocoatings on active materials for Li-ion batteries. *Journal of the European Ceramic Society*, Vol. 27, No. 2-3, 2007, pp. 909-913, ISSN 0955-2219

Dominko, R.; Gaberscek, M.; Drofenik, J.; Bele, M. & Pejovnik, S. (2001). A Novel Coating Technology for Preparation of Cathodes in Li-Ion Batteries. *Electrochemical and Solid-State Letters*, Vol. 4, No. 11, November 2001, pp. A187-A190, ISSN 1099-0062

Endo, M.; Kim, C.; Karaki, T.; Nishimura, Y.; Matthews, M. J.; Brown, S. D. M. & Dresselhaus, M. S. (1999). Anode performance of a Li ion battery based on graphitized and B-doped milled mesophase pitch-based carbon fibers. *Carbon*, Vol. 37, No. 4, June 1999, pp. 561-568, ISSN 0008-6223

Endo, M.; Kim, C.; Nishimura, K.; Fujino, T. & Miyashita, K. (2000). Recent development of carbon materials for Li ion batteries. *Carbon*, Vol. 38, No. 2, 2000, pp. 183-197, ISSN 0008-6223

Fang, H. T.; Liu, M.; Wang, D. W.; Sun, T.; Guan, D. S.; Li, F.; Zhou, J. G.; Sham, T. K. & Cheng, H. M. (2009). Comparison of the rate capability of nanostructured amorphous and anatase TiO_2 for lithium insertion using anodic TiO_2 nanotube arrays. *Nanotechnology*, Vol. 20, No. 22, June 2009, pp. -, ISSN 0957-4484

Fu, L. J.; Liu, H.; Li, C.; Wu, Y. P.; Rahm, E.; Holze, R. & Wu, H. Q. (2006). Surface modifications of electrode materials for lithium ion batteries. *Solid State Sciences*, Vol. 8, No. 2, February 2006, pp. 113-128, ISSN 1293-2558

Gao, J.; Ying, J.; Jiang, C. & Wan, C. (2007). High-density spherical $Li_4Ti_5O_{12}$/C anode material with good rate capability for lithium ion batteries. *Journal of Power Sources*, Vol. 166, No. 1, March 2007, pp. 255-259, ISSN 0378-7753

Gillot, F.; Boyanov, S.; Dupont, L.; Doublet, M. L.; Morcrette, A.; Monconduit, L. & Tarascon, J. M. (2005). Electrochemical reactivity and design of NiP_2 negative electrodes for secondary Li-lon batteries. *Chemistry of Materials*, Vol. 17, No. 25, December 2005, pp. 6327-6337, ISSN 0897-4756

Graetz, J.; Ahn, C. C.; Yazami, R. & Fultz, B. (2004). Nanocrystalline and Thin Film Germanium Electrodes with High Lithium Capacity and High Rate Capabilities. *Journal of the Electrochemical Society*, Vol. 151, No. 5, March 2004, pp. A698-A702, ISSN 0013-4651

Guo, H.; Zhao, H.; Jia, X.; Li, X. & Qiu, W. (2007). A novel micro-spherical $CoSn_2$/Sn alloy composite as high capacity anode materials for Li-ion rechargeable batteries. *Electrochimica Acta*, Vol. 52, No. 14, April 2007, pp. 4853-4857, ISSN 0013-4686

Guo, H.; Zhao, S.; Zhao, H. & Chen, Y. (2009). Synthesis and electrochemical performance of novel loose structured submicro/micro-sized $NiSn_x$ alloy composites for lithium batteries. *Electrochimica Acta*, Vol. 54, No. 16, June 2009, pp. 4040-4044, ISSN 0013-4686

Guo, K.; Pan, Q.; Wang, L. & Fang, S. (2002). Nano-scale copper-coated graphite as anode material for lithium-ion batteries. *Journal of Applied Electrochemistry*, Vol. 32, No. 6, June 2002, pp. 679-685, ISSN 0021-891X

Guo, Y.-G.; Hu, Y.-S.; Sigle, W. & Maier, J. (2007). Superior Electrode Performance of Nanostructured Mesoporous TiO_2 (Anatase) through Efficient Hierarchical Mixed Conducting Networks. *Advanced Materials*, Vol. 19, No. 16, July 2007, pp. 2087-2091, ISSN 1521-4095

Guo, Z. P.; Du, G. D.; Nuli, Y.; Hassan, M. F. & Liu, H. K. (2009). Ultra-fine porous SnO_2 nanopowder prepared via a molten salt process: a highly efficient anode material for lithium-ion batteries. *Journal of Materials Chemistry*, Vol. 19, No. 20, March 2009, pp. 3253-3257, ISSN 0959-9428

Hanai, K.; Liu, Y.; Imanishi, N.; Hirano, A.; Matsumura, M.; Ichikawa, T. & Takeda, Y. (2005). Electrochemical studies of the Si-based composites with large capacity and good cycling stability as anode materials for rechargeable lithium ion batteries. *Journal of Power Sources*, Vol. 146, No. 1-2, August 2005, pp. 156-160, ISSN 0378-7753

Hara, D.; Ikuta, H.; Uchimoto, Y. & Wakihara, M. (2002). Electrochemical properties of manganese vanadium molybdenum oxide as the anode for Li secondary batteries. *Journal of Materials Chemistry*, Vol. 12, No. 8, August 2002, pp. 2507-2512, ISSN 0959-9428

Hasegawa, T.; Mukai, S. R.; Shirato, Y. & Tamon, H. (2004). Preparation of carbon gel microspheres containing silicon powder for lithium ion battery anodes. *Carbon*, Vol. 42, No. 12-13, July 2004, pp. 2573-2579, ISSN 0008-6223

Hibino, M.; Abe, K.; Mochizuki, M. & Miyayama, M. (2004). Amorphous titanium oxide electrode for high-rate discharge and charge. *Journal of Power Sources*, Vol. 126, No. 1-2, February 2004, pp. 139-143, ISSN 0378-7753

Howell, D. (2008). "Progress Report for Energy Storage Research and Development." from http://www1.eere.energy.gov/vehiclesandfuels/pdfs/program/2008_energy_storage.pdf.

Hu, Y.-S.; Adelhelm, P.; Smarsly, B. M.; Hore, S.; Antonietti, M. & Maier, J. (2007). Synthesis of Hierarchically Porous Carbon Monoliths with Highly Ordered Microstructure and Their Application in Rechargeable Lithium Batteries with High-Rate Capability. *Advanced Functional Materials*, Vol. 17, No. 12, July 2007, pp. 1873-1878, ISSN 1616-3028

Hu, Y.-S.; Kienle, L.; Guo, Y.-G. & Maier, J. (2006). High Lithium Electroactivity of Nanometer-Sized Rutile TiO_2. *Advanced Materials*, Vol. 18, No. 11, April 2006, pp. 1421-1426, ISSN 1521-4095

Huang, S.; Wen, Z.; Gu, Z. & Zhu, X. (2005). Preparation and cycling performance of Al^{3+} and F^- co-substituted compounds $Li_4Al_xTi_{5-x}F_yO_{12-y}$. *Electrochimica Acta*, Vol. 50, No. 20, July 2005, pp. 4057-4062, ISSN 0013-4686

Huang, S.; Wen, Z.; Lin, B.; Han, J. & Xu, X. (2008). The high-rate performance of the newly designed $Li_4Ti_5O_{12}$/Cu composite anode for lithium ion batteries. *Journal of Alloys and Compounds*, Vol. 457, No. 1-2, June 2008, pp. 400-403, ISSN 0925-8388

Huang, S.; Wen, Z.; Zhu, X. & Yang, X. (2005). Research on $Li_4Ti_5O_{12}/Cu_xO$ Composite Anode Materials for Lithium-Ion Batteries. *Journal of the Electrochemical Society*, Vol. 152, No. 7, May 2005, pp. A1301-A1305, ISSN 0013-4651

Ji, L. & Zhang, X. (2009). Manganese oxide nanoparticle-loaded porous carbon nanofibers as anode materials for high-performance lithium-ion batteries. *Electrochemistry Communications*, Vol. 11, No. 4, April 2009, pp. 795-798, ISSN 1388-2481

Ji, Y. & Jiang, Y. (2006). Increasing the electrical conductivity of poly(vinylidene fluoride) by KrF excimer laser irradiation. *Applied Physics Letters*, Vol. 89, No. 22, 2006, pp. 221103-221103, ISSN 0003-6951

Julien, C. & Stoynov, Z. (1999). *Materials for Lithium-Ion Batteries*, Kluwer Academic Publishers, ISBN 0-7923-6650-6, Dordrecht

Kasavajjula, U.; Wang, C. S. & Appleby, A. J. (2007). Nano- and bulk-silicon-based insertion anodes for lithium-ion secondary cells. *Journal of Power Sources*, Vol. 163, No. 2, January 2007, pp. 1003-1039, ISSN 0378-7753

Kim, C.; Yang, K. S.; Kojima, M.; Yoshida, K.; Kim, Y. J.; Kim, Y. A. & Endo, M. (2006). Fabrication of electrospinning-derived carbon nanofiber webs for the anode material of lithium-ion secondary batteries. *Advanced Functional Materials*, Vol. 16, No. 18, December 2006, pp. 2393-2397, ISSN 1616-301X

Kim, H. & Cho, J. (2008). Template Synthesis of Hollow Sb Nanoparticles as a High-Performance Lithium Battery Anode Material. *Chemistry of Materials*, Vol. 20, No. 5, February 2008, pp. 1679-1681, ISSN 0897-4756

Kim, H. S.; Chung, K. Y. & Cho, B. W. (2009). Electrochemical properties of carbon-coated Si/B composite anode for lithium ion batteries. *Journal of Power Sources*, Vol. 189, No. 1, April 2009, pp. 108-113, ISSN 0378-7753

Kim, H. S.; Chung, Y. H.; Kang, S. H. & Sung, Y.-E. (2009). Electrochemical behavior of carbon-coated SnS_2 for use as the anode in lithium-ion batteries. *Electrochimica Acta*, Vol. 54, No. 13, May 2009, pp. 3606-3610, ISSN 0013-4686

Kim, S. S.; Kadoma, Y.; Ikuta, H.; Uchimoto, Y. & Wakihara, M. (2001). Electrochemical performance of natural graphite by surface modification using aluminum. *Electrochemical and Solid State Letters*, Vol. 4, No. 8, August 2001, pp. A109-A112, ISSN 1099-0062

Kottegoda, I. R. M.; Kadoma, Y.; Ikuta, H.; Uchimoto, Y. & Wakihara, M. (2002). Enhancement of Rate Capability in Graphite Anode by Surface Modification with Zirconia. *Electrochemical and Solid-State Letters*, Vol. 5, No. 12, December 2002, pp. A275-A278, ISSN 1099-0062

Kozlowski, R.; Ziólkowski, J.; Mocala, K. & Haber, J. (1980). Defect structures in the brannerite-type vanadates. I. Preparation and study of $MN_{1-x}\phi_xV_{2-2x}Mo_{2x}O_6$ ($0 <= x <= 0.45$). *Journal of Solid State Chemistry*, Vol. 35, No. 1, November 1980, pp. 1-9, ISSN 0022-4596

Lampe-Onnerud, C.; Shi, J.; Onnerud, P.; Chamberlain, R. & Barnett, B. (2001). Benchmark study on high performing carbon anode materials. *Journal of Power Sources*, Vol. 97-98, No. July 2001, pp. 133-136, ISSN 0378-7753

Lee, J.-H.; Kim, G.-S.; Choi, Y.-M.; Park, W. I.; Rogers, J. A. & Paik, U. (2008). Comparison of multiwalled carbon nanotubes and carbon black as percolative paths in aqueous-based natural graphite negative electrodes with high-rate capability for lithium-ion batteries. *Journal of Power Sources*, Vol. 184, No. 1, September 2008, pp. 308-311, ISSN 0378-7753

Lee, J. Y.; Zhang, R. & Liu, Z. (2000). Dispersion of Sn and SnO on carbon anodes. *Journal of Power Sources*, Vol. 90, No. 1, September 2000, pp. 70-75, ISSN 0378-7753

Lee, S.-Y.; Park, J.; Park, P.; Kim, J.; Ahn, S.; Lee, K.-J.; Lee, H.-D.; Park, J.-S.; Kim, D.-H. & Jeong, Y. (2009). Effect of MWCNT on the performances of the rounded shape natural graphite as anode material for lithium-ion batteries. *Journal of Solid State Electrochemistry*, Vol. No. July 2009, pp. ISSN 1433-0768

Li, C.; Yin, X.; Chen, L.; Li, Q. & Wang, T. (2009). Porous Carbon Nanofibers Derived from Conducting Polymer: Synthesis and Application in Lithium-Ion Batteries with High-Rate Capability. *The Journal of Physical Chemistry C*, Vol. 113, No. 30, July 2009, pp. 13438-13442, ISSN 1932-7447

Li, M. Q.; Qu, M. Z.; He, X. Y. & Yu, Z. L. (2009). Effects of electrolytes on the electrochemical performance of Si/graphite/disordered carbon composite anode for lithium-ion batteries. *Electrochimica Acta*, Vol. 54, No. 19, July 2009, pp. 4506-4513, ISSN 0013-4686

Li, X.; Qu, M. & Yu, Z. (2009). Structural and electrochemical performances of $Li_4Ti_{5-x}Zr_xO_{12}$ as anode material for lithium-ion batteries. *Journal of Alloys and Compounds*, Vol. In Press, Corrected Proof, No. August 2009, pp. ISSN 0925-8388

Liu, J.; Li, Y.; Huang, X.; Li, G. & Li, Z. (2008). Layered Double Hydroxide Nano- and Microstructures Grown Directly on Metal Substrates and Their Calcined Products for Application as Li-Ion Battery Electrodes. *Advanced Functional Materials*, Vol. 18, No. 9, April 2008, pp. 1448-1458, ISSN 1616-3028

Liu, J.; Xia, H.; Xue, D. & Lu, L. (2009). Double-Shelled Nanocapsules of V_2O_5-Based Composites as High-Performance Anode and Cathode Materials for Li Ion Batteries. *Journal of the American Chemical Society*, Vol. 131, No. 34, August 2009, pp. 12086-12087, ISSN 0002-7863

Long, J. W.; Dunn, B.; Rolison, D. R. & White, H. S. (2004). Three-Dimensional Battery Architectures. *Chemical Reviews*, Vol. 104, No. 10, August 2004, pp. 4463-4492, ISSN 0009-2665

Lou, X. W.; Li, C. M. & Archer, L. A. (2009). Designed Synthesis of Coaxial SnO_2@carbon Hollow Nanospheres for Highly Reversible Lithium Storage. *Advanced Materials*, Vol. 21, No. 24, March 2009, pp. 2536-2539, ISSN 1521-4095

Makovicka, J.; Sedlarikova, M.; Arenillas, A.; Velicka, J. & Vondrak, J. (2009). Expanded graphite as an intercalation anode material for lithium systems. *Journal of Solid State Electrochemistry*, Vol. 13, No. 9, Sep 2009, pp. 1467-1471, ISSN 1432-8488

Miyachi, M.; Yamamoto, H. & Kawai, H. (2007). Electrochemical Properties and Chemical Structures of Metal-Doped SiO Anodes for Li-Ion Rechargeable Batteries. *Journal of the Electrochemical Society*, Vol. 154, No. 4, February 2007, pp. A376-A380, ISSN 0013-4651

Nobili, F.; Dsoke, S.; Mancini, M.; Tossici, R. & Marassi, R. (2008). Electrochemical investigation of polarization phenomena and intercalation kinetics of oxidized graphite electrodes coated with evaporated metal layers. *Journal of Power Sources*, Vol. 180, No. 2, June 2008, pp. 845-851, ISSN 0378-7753

Nuli, Y. N.; Zhang, P.; Guo, Z. P.; Liu, H. K.; Yang, J. & Wang, J. L. (2009). Nickel-cobalt oxides/carbon nanoflakes as anode materials for lithium-ion batteries. *Materials Research Bulletin*, Vol. 44, No. 1, January 2009, pp. 140-145, ISSN 0025-5408

Ohara, S.; Suzuki, J.; Sekine, K. & Takamura, T. (2004). A thin film silicon anode for Li-ion batteries having a very large specific capacity and long cycle life. *Journal of Power Sources*, Vol. 136, No. 2, October 2004, pp. 303-306, ISSN 0378-7753

Park, C.-M.; Kim, Y.-U.; Kim, H. & Sohn, H.-J. (2006). Enhancement of the rate capability and cyclability of an Mg-C composite electrode for Li secondary batteries. *Journal of Power Sources*, Vol. 158, No. 2, August 2006, pp. 1451-1455, ISSN 0378-7753

Park, C.-M. & Sohn, H.-J. (2009). A mechano- and electrochemically controlled SnSb/C nanocomposite for rechargeable Li-ion batteries. *Electrochimica Acta*, Vol. 54, No. 26, November 2009, pp. 6367-6373, ISSN 0013-4686

Park, C.-M.; Yoon, S.; Lee, S.-I.; Kim, J.-H.; Jung, J.-H. & Sohn, H.-J. (2007). High-Rate Capability and Enhanced Cyclability of Antimony-Based Composites for Lithium Rechargeable Batteries. *Journal of the Electrochemical Society*, Vol. 154, No. 10, July 2007, pp. A917-A920, ISSN 0013-4651

Park, K. S.; Benayad, A.; Kang, D. J. & Doo, S. G. (2008). Nitridation-Driven Conductive $Li_4Ti_5O_{12}$ for Lithium Ion Batteries. *Journal of the American Chemical Society*, Vol. 130, No. 45, November 2008, pp. 14930-+, ISSN 0002-7863

Park, M.-S.; Wang, G.-X.; Kang, Y.-M.; Wexler, D.; Dou, S.-X. & Liu, H.-K. (2007). Preparation and Electrochemical Properties of SnO_2 Nanowires for Application in Lithium-Ion Batteries. *Angewandte Chemie International Edition*, Vol. 46, No. 5, December 2007, pp. 750-753, ISSN 1521-3773

Park, M. H.; Kim, M. G.; Joo, J.; Kim, K.; Kim, J.; Ahn, S.; Cui, Y. & Cho, J. (2009). Silicon Nanotube Battery Anodes. *Nano Letters*, Vol. 9, No. 11, November 2009, pp. 3844-3847, ISSN 1530-6984

Porter, D. A. & Easterling, K. E. (1991). *Phase Transformations in Metals and Alloys*, Chapman & Hall, ISBN 0-7487-5741-4, London

Qi, Y.; Huang, Y.; Jia, D.; Bao, S.-J. & Guo, Z. P. (2009). Preparation and characterization of novel spinel $Li_4Ti_5O_{12-x}Br_x$ anode materials. *Electrochimica Acta*, Vol. 54, No. 21, August 2009, pp. 4772-4776, ISSN 0013-4686

Qiao, H.; Wang, Y.; Xiao, L. & Zhang, L. (2008). High lithium electroactivity of hierarchical porous rutile TiO_2 nanorod microspheres. *Electrochemistry Communications*, Vol. 10, No. 9, September 2008, pp. 1280-1283, ISSN 1388-2481

Ryu, J. H.; Kim, J. W.; Sung, Y. E. & Oh, S. M. (2004). Failure modes of silicon powder negative electrode in lithium secondary batteries. *Electrochemical and Solid State Letters*, Vol. 7, No. 10, September 2004, pp. A306-A309, ISSN 1099-0062

Santos-Pe, J.; Brousse, T.; S?chez, L.; Morales, J. & Schleich, D. M. (2001). Antimony doping effect on the electrochemical behavior of SnO_2 thin film electrodes. *Journal of Power Sources*, Vol. 97-98, No. July 2001, pp. 232-234, ISSN 0378-7753

Sharma, N.; Shaju, K. M.; Subba Rao, G. V.; Chowdari, B. V. R.; Dong, Z. L. & White, T. J. (2003). Carbon-Coated Nanophase $CaMoO_4$ as Anode Material for Li Ion Batteries. *Chemistry of Materials*, Vol. 16, No. 3, December 2003, pp. 504-512, ISSN 0897-4756

Singhal, A.; Skandan, G.; Amatucci, G.; Badway, F.; Ye, N.; Manthiram, A.; Ye, H. & Xu, J. J. (2004). Nanostructured electrodes for next generation rechargeable electrochemical devices. *Journal of Power Sources*, Vol. 129, No. 1, April 2004, pp. 38-44, ISSN 0378-7753

Skowronski, J. M. & Knofczynski, K. (2009). Catalytically graphitized glass-like carbon examined as anode for lithium-ion cell performing at high charge/discharge rates. *Journal of Power Sources*, Vol. 194, No. 1, October 2009, pp. 81-87, ISSN 0378-7753

Souza, D. C. S.; Pralong, V.; Jacobson, A. J. & Nazar, L. F. (2002). A reversible solid-state crystalline transformation in a metal phosphide induced by redox chemistry. *Science*, Vol. 296, No. 5575, June 2002, pp. 2012-2015, ISSN 0036-8075

Subramanian, V.; Zhu, H. & Wei, B. (2006). High Rate Reversibility Anode Materials of Lithium Batteries from Vapor-Grown Carbon Nanofibers. *The Journal of Physical Chemistry B*, Vol. 110, No. 14, March 2006, pp. 7178-7183, ISSN 1520-6106

Takai, S.; Kamata, M.; Fujine, S.; Yoneda, K.; Kanda, K. & Esaka, T. (1999). Diffusion coefficient measurement of lithium ion in sintered $Li_{1.33}Ti_{1.67}O_4$ by means of neutron radiography. *Solid State Ionics*, Vol. 123, No. 1-4, August 1999, pp. 165-172, ISSN 0167-2738

Takamura, T.; Sumiya, K.; Suzuki, J.; Yamada, C. & Sekine, K. (1999). Enhancement of Li doping/undoping reaction rate of carbonaceous materials by coating with an evaporated metal film. *Journal of Power Sources*, Vol. 81-82, No. September 1999, pp. 368-372, ISSN 0378-7753

Tang, Y.; Yang, L.; Fang, S. & Qiu, Z. (2009). $Li_4Ti_5O_{12}$ hollow microspheres assembled by nanosheets as an anode material for high-rate lithium ion batteries. *Electrochimica Acta*, Vol. 54, No. 26, November 2009, pp. 6244-6249, ISSN 0013-4686

Tang, Y. F.; Yang, L.; Qiu, Z. & Huang, J. S. (2008). Preparation and electrochemical lithium storage of flower-like spinel $Li_4Ti_5O_{12}$ consisting of nanosheets. *Electrochemistry Communications*, Vol. 10, No. 10, October 2008, pp. 1513-1516, ISSN 1388-2481

Tao, Z.; Liang, J. & Chen, J. (2007). Template-Directed Materials for Rechargeable Lithium-Ion Batteries. *Chemistry of Materials*, Vol. 20, No. 3, December 2007, pp. 667-681, ISSN 0897-4756

Tarascon, J. M. & Armand, M. (2001). Issues and challenges facing rechargeable lithium batteries. *Nature*, Vol. 414, No. 6861, November 2001, pp. 359-367, ISSN 0028-0836

Tarascon, J. M.; Morcrette, M.; Dupont, L.; Chabre, Y.; Payen, C.; Larcher, D. & Pralong, V. (2003). On the Electrochemical Reactivity Mechanism of $CoSb_3$ vs. Lithium. *Journal of the Electrochemical Society*, Vol. 150, No. 6, June 2003, pp. A732-A741, ISSN 0013-4651

Vaughey, J. T.; Fransson, L.; Swinger, H. A.; Edstrom, K. & Thackeray, M. M. (2003). Alternative anode materials for lithium-ion batteries: a study of Ag_3Sb. *Journal of Power Sources*, Vol. 119, No. June 2003, pp. 64-68, ISSN 0378-7753

Veeraraghavan, B.; Durairajan, A.; Haran, B.; Popov, B. & Guidotti, R. (2002). Study of Sn-Coated Graphite as Anode Material for Secondary Lithium-Ion Batteries. *Journal of the Electrochemical Society*, Vol. 149, No. 6, April 2002, pp. A675-A681, ISSN 0013-4651

Veeraraghavan, B.; Paul, J.; Haran, B. & Popov, B. (2002). Study of polypyrrole graphite composite as anode material for secondary lithium-ion batteries. *Journal of Power Sources*, Vol. 109, No. 2, July 2002, pp. 377-387, ISSN 0378-7753

Wachtler, M.; Winter, M. & Besenhard, J. O. (2002). Anodic materials for rechargeable Li-batteries. *Journal of Power Sources*, Vol. 105, No. 2, March 2002, pp. 151-160, ISSN 0378-7753

Wakihara, M. (2001). Recent developments in lithium ion batteries. *Materials Science & Engineering R-Reports*, Vol. 33, No. 4, June 2001, pp. 109-134, ISSN 0927-796X

Wang, B. L.; Chen, Q.; Hu, J.; Li, H.; Hu, Y. F. & Peng, L. M. (2005). Synthesis and characterization of large scale potassium titanate nanowires with good Li-intercalation performance. *Chemical Physics Letters*, Vol. 406, No. 1-3, April 2005, pp. 95-100, ISSN 0009-2614

Wang, G. J.; Gao, J.; Fu, L. J.; Zhao, N. H.; Wu, Y. P. & Takamura, T. (2007). Preparation and characteristic of carbon-coated $Li_4Ti_5O_{12}$ anode material. *Journal of Power Sources*, Vol. 174, No. 2, December 2007, pp. 1109-1112, ISSN 0378-7753

Wang, G. X.; Ahn, J. H.; Yao, J.; Bewlay, S. & Liu, H. K. (2004). Nanostructured Si-C composite anodes for lithium-ion batteries. *Electrochemistry Communications*, Vol. 6, No. 7, July 2004, pp. 689-692, ISSN 1388-2481

Wang, G. X.; Shen, X. P.; Yao, J. & Park, J. (2009). Graphene nanosheets for enhanced lithium storage in lithium ion batteries. *Carbon*, Vol. 47, No. 8, Jul 2009, pp. 2049-2053, ISSN 0008-6223

Wang, L.; Yu, Y.; Chen, P.-C. & Chen, C.-H. (2008). Electrospun carbon-cobalt composite nanofiber as an anode material for lithium ion batteries. *Scripta Materialia*, Vol. 58, No. 5, 2008, pp. 405-408, ISSN 1359-6462

Wang, L.; Yu, Y.; Chen, P. C.; Zhang, D. W. & Chen, C. H. (2008). Electrospinning synthesis of C/Fe_3O_4 composite nanofibers and their application for high performance lithium-ion batteries. *Journal of Power Sources*, Vol. 183, No. 2, September 2008, pp. 717-723, ISSN 0378-7753

Wang, S. Q.; Zhang, J. Y. & Chen, C. H. (2007). Dandelion-like hollow microspheres of CuO as anode material for lithium-ion batteries. *Scripta Materialia*, Vol. 57, No. 4, August 2007, pp. 337-340, ISSN 1359-6462

Wang, Y.; Zhang, Y.-F.; Liu, H.-R.; Yu, S.-J. & Qin, Q.-Z. (2003). Nanocrystalline NiO thin film anode with MgO coating for Li-ion batteries. *Electrochimica Acta*, Vol. 48, No. 28, December 2003, pp. 4253-4259, ISSN 0013-4686

Wen, Z.; Huang, S.; Yang, X. & Lin, B. (2008). High rate electrode materials for lithium ion batteries. *Solid State Ionics*, Vol. 179, No. 27-32, 2008, pp. 1800-1805, ISSN 0167-2738

Wen, Z.; Wang, Q.; Zhang, Q. & Li, J. (2007). In Situ Growth of Mesoporous SnO_2 on Multiwalled Carbon Nanotubes: A Novel Composite with Porous-Tube Structure as Anode for Lithium Batteries. *Advanced Functional Materials*, Vol. 17, No. 15, August 2007, pp. 2772-2778, ISSN 1616-3028

Wen, Z. S.; Yang, J.; Wang, B. F.; Wang, K. & Liu, Y. (2003). High capacity silicon/carbon composite anode materials for lithium ion batteries. *Electrochemistry Communications*, Vol. 5, No. 2, February 2003, pp. 165-168, ISSN 1388-2481

Wu, Y. P.; Rahm, E. & Holze, R. (2003). Carbon anode materials for lithium ion batteries. *Journal of Power Sources*, Vol. 114, No. 2, March 2003, pp. 228-236, ISSN 0378-7753

Xia, Y. N.; Yang, P. D.; Sun, Y. G.; Wu, Y. Y.; Mayers, B.; Gates, B.; Yin, Y. D.; Kim, F. & Yan, Y. Q. (2003). One-dimensional nanostructures: Synthesis, characterization, and applications. *Advanced Materials*, Vol. 15, No. 5, March 2003, pp. 353-389, ISSN 0935-9648

Xiao, L.; Li, J.; Li, Q. & Zhang, L. (2009). One-pot template-free synthesis, formation mechanism, and lithium ions storage property of hollow SnO_2 microspheres. *Journal of Solid State Electrochemistry*, Vol. No. June 2009, pp. ISSN 1433-0768

Yan, Y. & et al. (2007). Nanoporous cuprous oxide/lithia composite anode with capacity increasing characteristic and high rate capability. *Nanotechnology*, Vol. 18, No. 5, January 2007, pp. 055706, ISSN 0957-4484

Yang, X. L.; Wen, Z. Y.; Huang, S. H.; Zhu, X. J. & Zhang, X. F. (2006). Electrochemical performances of silicon electrode with silver additives. *Solid State Ionics*, Vol. 177, No. 26-32, October 2006, pp. 2807-2810, ISSN 0167-2738

Yao, W.; Yang, J.; Wang, J. & Tao, L. (2008). Synthesis and electrochemical performance of carbon nanofiber-cobalt oxide composites. *Electrochimica Acta*, Vol. 53, No. 24, October 2008, pp. 7326-7330, ISSN 0013-4686

Yao, X. L.; Xie, S.; Nian, H. Q. & Chen, C. H. (2008). Spinel $Li_4Ti_5O_{12}$ as a reversible anode material down to 0 V. *Journal of Alloys and Compounds*, Vol. 465, No. 1-2, October 2008, pp. 375-379, ISSN 0925-8388

Yazami, R. (1999). Surface chemistry and lithium storage capability of the graphite-lithium electrode. *Electrochimica Acta*, Vol. 45, No. 1-2, September 1999, pp. 87-97, ISSN 0013-4686

Yin, J. T.; Wada, M.; Kitano, Y.; Tanase, S.; Kajita, O. & Sakai, T. (2005). Nanostructured Ag-Fe-Sn/carbon nanotubes composites as anode materials for advanced lithium-ion batteries. *Journal of the Electrochemical Society*, Vol. 152, No. 7, June 2005, pp. A1341-A1346, ISSN 0013-4651

Yin, J. T.; Wada, M.; Tanase, S. & Sakai, T. (2004). Nanocrystalline Ag-Fe-Sn anode materials for Li-ion batteries. *Journal of the Electrochemical Society*, Vol. 151, No. 4, February 2004, pp. A583-A589, ISSN 0013-4651

Yoo, E.; Kim, J.; Hosono, E.; Zhou, H.; Kudo, T. & Honma, I. (2008). Large reversible Li storage of graphene nanosheet families for use in rechargeable lithium ion batteries. *Nano Letters*, Vol. 8, No. 8, Aug 2008, pp. 2277-2282, ISSN 1530-6984

Yoon, S.; Ka, B. H.; Lee, C.; Park, M. & Oh, S. M. (2009). Preparation of Nanotube TiO_2-Carbon Composite and Its Anode Performance in Lithium-Ion Batteries. *Electrochemical and Solid-State Letters*, Vol. 12, No. 2, December 2009, pp. A28-A32, ISSN 1099-0062

Yu, H.; Zhang, X.; Jalbout, A. F.; Yan, X.; Pan, X.; Xie, H. & Wang, R. (2008). High-rate characteristics of novel anode $Li_4Ti_5O_{12}$/polyacene materials for Li-ion secondary batteries. *Electrochimica Acta*, Vol. 53, No. 12, May 2008, pp. 4200-4204, ISSN 0013-4686

Yu, Y.; Chen, C.-H. & Shi, Y. (2007). A Tin-Based Amorphous Oxide Composite with a Porous, Spherical, Multideck-Cage Morphology as a Highly Reversible Anode Material for Lithium-Ion Batteries. *Advanced Materials*, Vol. 19, No. 7, March 2007, pp. 993-997, ISSN 1521-4095

Zaghib, K.; Song, X.; Guerfi, A.; Rioux, R. & Kinoshita, K. (2003). Purification process of natural graphite as anode for Li-ion batteries: chemical versus thermal. *Journal of Power Sources*, Vol. 119-121, No. June 2003, pp. 8-15, ISSN 0378-7753

Zhang, C. Q.; Tu, J. P.; Yuan, Y. F.; Huang, X. H.; Chen, X. T. & Mao, F. (2007). Electrochemical performances of Ni-coated ZnO as an anode material for lithium-ion batteries. *Journal of the Electrochemical Society*, Vol. 154, No. 2, December 2007, pp. A65-A69, ISSN 0013-4651

Zhang, P.; Guo, Z. P.; Kang, S. G.; Choi, Y. J.; Kim, C. J.; Kim, K. W. & Liu, H. K. (2009). Three-dimensional Li_2O-NiO-CoO composite thin-film anode with network structure for lithium-ion batteries. *Journal of Power Sources*, Vol. 189, No. 1, April 2009, pp. 566-570, ISSN 0378-7753

Zhang, W.-M.; Hu, J.-S.; Guo, Y.-G.; Zheng, S.-F.; Zhong, L.-S.; Song, W.-G. & Wan, L.-J. (2008). Tin-Nanoparticles Encapsulated in Elastic Hollow Carbon Spheres for High-Performance Anode Material in Lithium-Ion Batteries. *Advanced Materials*, Vol. 20, No. 6, February 2008, pp. 1160-1165, ISSN 1521-4095

Zhang, W.-M.; Wu, X.-L.; Hu, J.-S.; Guo, Y.-G. & Wan, L.-J. (2008). Carbon Coated Fe_3O_4 Nanospindles as a Superior Anode Material for Lithium-Ion Batteries. *Advanced Functional Materials*, Vol. 18, No. 24, November 2008, pp. 3941-3946, ISSN 1616-3028

Zhao, H.; Li, Y.; Zhu, Z.; Lin, J.; Tian, Z. & Wang, R. (2008). Structural and electrochemical characteristics of $Li_{4-x}Al_xTi_5O_{12}$ as anode material for lithium-ion batteries. *Electrochimica Acta*, Vol. 53, No. 24, October 2008, pp. 7079-7083, ISSN 0013-4686

Zheng, S.-F.; Hu, J.-S.; Zhong, L.-S.; Song, W.-G.; Wan, L.-J. & Guo, Y.-G. (2008). Introducing Dual Functional CNT Networks into CuO Nanomicrospheres toward Superior Electrode Materials for Lithium-Ion Batteries. *Chemistry of Materials*, Vol. 20, No. 11, June 2008, pp. 3617-3622, ISSN 0897-4756

Zhou, J.; Song, H.; Chen, X.; Zhi, L.; Yang, S.; Huo, J. & Yang, W. (2009). Carbon-Encapsulated Metal Oxide Hollow Nanoparticles and Metal Oxide Hollow Nanoparticles: A General Synthesis Strategy and Its Application to Lithium-Ion Batteries. *Chemistry of Materials*, Vol. 21, No. 13, May 2009, pp. 2935-2940, ISSN 0897-4756

2

Thermo-chemical process associated with lithium cobalt oxide cathode in lithium ion batteries

Chil-Hoon Doh[+] and Angathevar Veluchamy*
[+]*Korea Electrotechnology Research Institute, Republic of Korea,*
**Central ElectrochemicalResearch Institute, India*

1. Introduction

The concept of galvanic couple and the development of battery and fuel cells made possible the direct current (DC) producing devices for practical applications. Even though, existing aqueous electrolyte based power sources such as lead acid, nickel metal-hydride, nickel-cadmium, alkaline/dry zinc based batteries and magnesium systems reached mature level of technology, the lithium based non-aqueous cell system (Plitcha et al., 1987) is able to penetrate and steadily expand its market share. Notwithstanding high cost, the lithium cells became the candidate of choice for miniature application and also for futuristic power pack for electric vehicle propulsion owing to its light weight, high voltage, high energy density and low self discharge characteristics. Present day lithium rechargeable cells are constructed usually by coupling a graphite anode and any one of the cathodes among lithium cobaltate(Li_xCoO_2), lithium manganese spinel ($Li_xMn_2O_4$), Lithium iron phosphate Li_xFePO_4(Olivine) and lithium Nickelate (Li_xNiO_2) in an air tight pouch or in a metal container. Assisted by potential difference between the anode and cathode electricity (electrons) flows from LiC_6(lithium intercalated graphite) anode to the cathode through an external load accompanying simultaneously Li^+ ion de-intercalation from the anode and intercalation at the cathode, maintains charge neutrality in the electrodes for which the electrolyte plays the role of transporting Li^+ ions.

2. Problem description

Among the lithium batteries available in the market, one with Li_xCoO_2 cathode and graphite anode is acclaimed widely as a source of power for portable electronics. This cell system is considerably stable and provides acceptable calendar/cycle life at room temperature during normal operating conditions. However, under abuse conditions such as thermal (heating), mechanical (crushing) or electrical (overcharge), the temperature of the cell rises due to the chemical reactions between the organic solvent and electrode materials leading to cell

failure/explosion. The chemical reaction is prompted because of the coexistence of 1) combustible organic solvent with inorganic salt electrolyte 2) lithiated graphite anode and 3) partially delithiated Li_xCoO_2 cathode in the charged state. The graphite anode intercalate fairly well during the initial cycles. As the cycle proceeds, the available intercalating sites in the graphite slowly decreases and the lithium deposition over the surface of the anode increases during charging process. Such a situation prompts non-even lithium deposition or even dendrite growth over the graphite surface. When the battery is in the charged state the cathode remains in a delithiated state. Flow of current over and above the tolerable/standard charged state causes instability to the cathode which starts to release oxygen into the electrolyte. Thus released oxygen reacts exothermally with the lithium plated over the graphite anode and increases the temperature of the cell making the cathode to release oxygen further. The cell which was in the dormant state in the absence of oxygen and heat now becomes an explosive device in the event the cell is met with any abuse.

In the recent past the widespread recall of laptop batteries affected nearly 10 million products when it was found that some batteries in notebook computers got overheated and in some cases caught fire (ANSI News, 2006). There were also sporadic reports on the explosion of cell phones that contained lithium ion batteries. In consequence, safety became the password of lithium ion battery and it became mandatory for any particular company to evaluate and assure the quality of their product. In order to evaluate and improve the safety standards of lithium ion batteries, abuse tests procedures have been formulated by establishments such as Underwriter's Laboratories, UL-1642 (Under writer's Laboratories, 1995), United States Advanced Battery Consortium (USABC), Electrochemical Storage System Abuse Test Procedure Manual (Spotnitz & Franklin, 2003), and Japan Storage Battery Associations (JBA) (Tobishima & Yamaki, 1999).
This chapter presents reviews related to solid electrolyte interphase (SEI) film which provides stability to the electrode active materials, thermal study on electrode materials, on cell safety, additives to electrolyte, dopants & coatings to electro-active materials and coatings to electrodes. Also presents the contributions of the authors on the cell safety through experimental work, the mechanism underlying the cell safety, suggestions and conclusion for providing safe and long life Li-ion batteries.

3. Thermal stability–State of the art

3.1 Solid electrolyte interphase (SEI) film

In the ambient temperature, the charged battery exhibits phenomenal stability owing to solid electrolyte interphase film (SEI), a protective layer formed over the electrode particles during initial charging process (Aubach et al., 1997). This thin film is reported to be an electronically resistive, allows easy diffusion of lithium ions for providing cycle life characteristics (Ota et al., 2002). The stability of this film determines calendar life and risk free handling of the battery whereas its stability depends on operating temperature, charging current/voltages, electrolyte-solvent environment and extent of battery abuse.
Several researchers made in-depth study to understand the nature of the SEI film, electrode material properties, abuse test behavior of the batteries and also suggested precautionary measures to be followed for safe handling of the battery. The battery becomes hazardous when there arises flow of surge current into or out of the charged cell to cause SEI film break

down resulting in direct contact of the electrolyte with the electrode materials initiating exothermic chemical reactions ultimately leading to failure, bursting or bulging of the battery (Doh et al., 2008).

The authors in (Richard & Dahn, 1999) point out that at elevated temperatures, the SEI film is not stable which is why a rechargeable lithium battery with a lithium metal anode is unsafe. Present day primary lithium batteries use lithium foil anode while rechargeable batteries employ graphite anodes. In (Ota et al., 2003) the authors discuss on the nature of SEI layer in poly propylene carbonate(PC)-based electrolyte containing ethylene sulphite (ES) additive based on different sulphur oxidation states with sulfur K-edge X-ray absorption near-edge structure spectroscopy (S K-edge XANES), X-ray photo electron spectroscopy(XPS) and time-of-flight–secondary ion mass spectrometry(TOF-SIMS). The authors noted an inorganic film made of Li_2SiO_3, organic film, $ROSO_2Li$ on the graphite anode and also alkyl sulphide species over the cathode.

The main chemical species present in the interphase layer has been characterized through novel XPS combined with both core peaks and valance band analysis (Dedryvere et al., 2007). The authors noted cell potential dependent surface films on both positive and negative electrodes at different successive voltage ranges. In the negative electrode between 3 and 3.8 V the main species formed is Li_2CO_3 along with small but a significant quantity of CH_3OCO_2Li. Over the positive electrode a deposit of LiF is observed which upon interaction with proton (formed due to oxidation of the solvent with the cathode) forms H_2F_2. The acidic species HF_2^- formed from H_2F_2 then reacts with Li_2CO_3 present in SEI film making it more fragile.

The authors in (Leroy et al., 2007) reported through XPS studies for the four lithium salts $LiPF_6$, $LiBF_4$, LiTFSI and LiBETI that are most preferred for Li-ion batteries. In all four cases the formation of carbonate species in the SEI film has been attributed to the reduction of solvents. At the first stage identified a large deposit of Li_2CO_3 and $ROCO_2Li$ at 3.8 V. In comparison to other salts a high deposit of LiF is observed for $LiPF_6$ at the end of charging. An increase of acidity observed at the end of charging has been attributed to the formation of acid species like HF or HF_2^- which is supposed to react with Li_2CO_3 of the SEI film.

Through ^{7}LiNMR studies (Wang et al., 2001) monitored quantitatively the growth of the SEI over the surface of active materials of the positive electrode which consists mainly lithiated materials. The report in (Lin et al., 2001) states that for batteries operating at low temperature there is an increase of the impedance of SEI with state of charge of graphite electrode. Also the report by (Zheng et al., 1999) states that there is an increase in the instability of the SEI film for the cells operating at high temperature ~70°C.

3.2 Electrode materials

In (MacNeil and Dahn, 2001) the thermal decomposition of $Li_{0.5}CoO_2$ by accelerated rate calorimetry(ARC) and X-ray diffraction(XRD) has been reported which states that the oxygen loss from the cathode remains above 200°C. However, the reaction of $Li_{0.5}CoO_2$ with ethylene carbonate: diethyl carbonate (EC: DEC) solvents starts at a temperature as low as 130°C which is much lower than the decomposition temperature of $Li_{0.5}CoO_2$. The reduction of $Li_{0.5}CoO_2$ to CoO or even to Co is found to be based on the reducing power of the solvent. The increase of $LiPF_6$ salt concentration seems to slow down the solvent combustion reaction, and the cathode-electrolyte reaction in practical Li-ion cells. The study shows that

more thermally stable cells based on $LiCoO_2$ cathode could be made using higher concentration of $LiPF_6$ salt (near 1.5M).
The authors (Richard and Dahn, 1999) report through ARC experiments that for MCMB with $LiBF_4$ the self heating begins early (50°C) compared to MCMB with $LiPF_6$ (70°C) for the same solvent composition (EC: DEC = 1:1). When MCMB sample containing $LiPF_6$ (EC:DEC=33:67) was heated directly to 150°C , the self-heating starts at a rate approximately equal to 100°C/min. The authors also stress the usefulness of knowledge on self-heating process for the understanding of the abuse behaviors of practical cells.
An important observation made by (McNeil and Dahn, 2002) is that when the electrode mass is low compared to the mass of the solvent a large exothermic reaction occurs above 300°C forming a large amount of Co metal as compared to other species. The amount of cobalt carbonate formed becomes less as most of CoO is reduced to Co. When the electrode mass is larger than the mass of the solvent, the solvent becomes insufficient to reduce fully the higher valent cobalt to Co metal.
The temperature dependency of the heat generation between 283 and 333 K (Saito et al, 1997) shows an exothermic peak and an endothermic peak at around 4V caused by a phase transition of the positive electrode material Li_xCoO_2 between the hexagonal and monoclinic structures observed at around x = 0.5. At the point of phase change cathode also faces instability. Also the authors (Reimer & Dahn, 1992) describe that the temperature rise of battery is due mainly to two factors one the electrochemical reactions and the other associated polarization. The overcharges are the sign of cathode degradation and electrolyte decomposition at high voltages. As lithium is removed from Li_xCoO_2, oxidation of Co^{3+} to an unstable oxidation state Co^{4+} follows. Large concentration of Co^{4+} is most likely to destroy the cathode crystallinity, finally the cell reversibility.
In (Yamaki et al., 2003) the authors made an in-depth study of the lithium battery electrodes. From high temperature XRD it was found that chemically delithiated $Li_{0.49}CoO_2$ exhibited exothermic peak at 190°C possibly caused by structural changes from a layered R-3*m* to spinel (F*d*3*m*) unaccompanied by oxygen evolution. From DSC measurements for reaction of $Li_{0.49}CoO_2$ with electrolyte the authors reported two peaks, one at 190°C, due mainly to the decomposition of the solvent with the active cathode surface and the other at 230°C caused by oxygen release from $Li_{0.49}CoO_2$. The reaction of lithiated graphite with electrolyte showed several exothermic peaks. One small peak at 140°C for the reaction between PVdF binders coated lithiated graphite and electrolyte resulting in SEI film formation, another sharp peak at 280°C attributed to break down of SEI film followed by direct reaction between lithiated graphite and electrolyte.
In (Zhang et al., 1998) investigated through DSC the intrinsic reactivity of Li_xNiO_2, Li_xCoO_2, $Li_xMn_2O_4$, and Li_xC_6, at different values of x. This experiment shows the reactivity between the active material and electrolyte as exthothermic reaction. The amplitude of reaction depends on the availability of M^{4+}, particularly where M = Ni or Co and that Mn^{4+} exhibits less oxidizing capability relative to others. Both Li_xNiO_2 and Li_xCoO_2 exhibited strong reactivity with the onset temperatures in the range 200 to 230°C as x was decreased, suggesting that control of stoichiometry is very important for achieving cell safety. Lithiated carbon in the presence of electrolyte produced DSC exotherms in two temperature ranges. The first was a low energy peak with onset temperatures at approximately 120 - 140°C which appeared to be due to surface passivation of the lithiated carbon materials. The second peak started at about 230°C and may have involved the PVDF binder materials of the electrode.

3.3 Abuse test behavior of the cells

The following passage presents an overview of the literature available on abuse behavior of lithium ion batteries. In (Wainwright, 1995) the author illustrated through spot weld tests for a cell with Li_xCoO_2/DME combination a violent venting when x = 0.4 but could not vent for x = 0.5, even when the spot heating was sufficient to melt and breach the container. In (Fouchard et al, 1994) the authors bring out the response of AA size lithium ion cells on heating in an oven and reported that the thermal stability of the cathode increased with increasing lithiation of the cathode.

In (Kitoh & Nemoto, 1999) the authors noted that upon external short circuiting of the lithium ion cell the temperature reached ~100°C followed by a sudden drop in current. The drop in current was attributed to melting and shut down function of the separators. During nail penetration test (nail speed 1mm/s), the cell vented immediately. After the nail was inserted the cell did not ignite but reached a maximum temperature, 380°C.

In (Maleki et al., 1999), the thermal stability study of fully charged 550mAh prismatic lithium ion cell and the components inside the cell showed that the self-heating exothermic reactions starts at 123°C, and thermal runaway at 167°C. The report also brings out that the total exothermic heat generation of the NE and PE materials is 697 and 407 J/g respectively. The heat generation of NE and PE materials washed with diethyl carbonate, dried at ~ 65°C under vacuum are significantly lower than unwashed samples. Lithium plating increases the heat generation of the NE material at temperatures near lithium melting point. Comparison of heat generation profiles from DSC and ARC tests indicates the thermal runaway of the cell as close as to the decomposition temperature range of the unwashed PE materials. The authors conclude that the heat generation from the decomposition of PE materials and reaction of that with electrolyte initiates thermal runaway in a Li-ion cell subjected to thermal or other abuse exposures.

In (Biensan et al., 1999) all parameter identified from the DSC studies suggested that the reaction kinetics at the negative electrode, the binder nature (fluorinated or not), the state of charge of positive materials are the deciding ones for ascertaining the maximum safety voltage of the cell. Through nail tests on 4/5A size cells reported the safe voltage for a cell with cobalt oxide cathode is higher than that of nickel oxide cathode and with non fluorinated binder than with polyvinylidene fluoride binder.

(Tobishima and Yamaki, 1999) reported swelling on overcharge of 600mAh cells with aluminum can charged to 1C and 1.5C for which the safety vent did not open or smoke. On the other hand for a cell charged at 2C rate, the safety vent and anode cap housing welded ultrasonically opened simultaneously. The authors describe that as the overcharge current increases the heat output increases since joule heat output is proportional to i^2R(i= current, R= Resistance). Again if the graphite is not sufficiently porous to intercalate during charging then the lithium deposits on its surface, cause a drastic reduction in thermal stability. The thermal stability test on a commercial cell with 1270mAh capacity the cell smoked only at 155°C which led them to conclude that the thermal stability limit for lithium cells is not lower than 150°C. Upon nail penetration test a commercial prismatic cell does not smoke when charged at normal charging voltage to reach 835mAh. However, the cell smoked when charged 0.03V higher than the standard voltage to reach 863mAh. During crush test a cell charged to its standard capacity (720mAh) did not smoke but the same cell with 200% overcharged smoked, the possible reason presented being the deposition of lithium metal as fine particles on the graphite surface anode.

Dahn (Dahn, 2001), has reported that for a 18650-size cell embedded with thermo couple when pierced by a a nail to the depth of <4.5 mm the cell temperature exceeded 600°C while for a fast , deep nail penetration(7.5 mm) the cell temperature did not exceed 140°C.
The overcharge and short circuit behavior of 1.5Ah prismatic lithium-ion cells presented in (Leising et al., 2001) showed that during short circuit test the inner temperature of the cell reached 132°C attributed for the shutdown temperature (132°C, melting point of polypropylene separator) and the outer surface of the cell measured was only 94°C. The salient features of their experiments are: (I), the thermal runaway not only depended on the state of charge of the cell but also on the amount of cathode material. (II), the battery rupture occurs when the cell temperature exceeds 190°C suggesting that the melting of the lithium metal may be the key factor responsible for rupture of the cells and (III), the cells assembled with lithium removed Li_xCoO_2 cathode and graphite anode upon overcharge tests (no lithium could plate on the anode) showed significantly higher temperature (~280°C) and (IV), the abused cell maintains a temperature difference of over 80°C between the interior and external surface.
The heat generated during overcharging was measured by a twin type heat conduction calorimeter at constant charging current at different charging rates (Saito et al, 2001) which gives values of heat flow especially the inner temperature difference between the sample vessel and reference vessel. The heat flow seems to be almost proportional to the current passed during the overcharge test for 18650-size cells. The authors measured the heat released for $LiMn_2O_4$ and $LiCoO_2$ cells at 0.2C rate for 160- 180% overcharging current.
Venugopal (Venugopal, 2001) showed that the vulnerability of battery is due to battery abuse which becomes less severe due to shutdown function of polyolefin separator membranes where the melting of the separator prevents the ionic flow through the pores, thereby minimizes the passage of current thus stopping the cell thermal runaway.
In (Spotnitz & Franklin, 2003) the abuse test on lithium-ion cells through modeling showed that the fluorinated binder plays relatively unimportant role in thermal runaway. In an overcharged cell even though the graphite is in well intercalated state the lithium prefers to react with solvent rather than the binder though there exists an intimate contact between lithium and the binder. Their result also shows that rapid and localized heat generation during nail test and crush test could activate well all the chemical reaction in the cell. In (Liu et al., 2001) it is observed that the gel polymer electrolyte provides less flammable environment within the cell
Wu et al., (2004) reported by soft-nail penetration on laminated aluminum packaged commercial lithium ion battery. The reports state that an internal short is more dangerous than an external short, because the former (soft-nail test) induces an enormous heat instantaneously and locally to cause thermal runaway of the electrolyte and electrode materials. Their experiment showed that all separators except polypropylene (PP) separator showed distinct shut down especially for batteries with more than 200 cycles, implying usage of PP may result in fire. The reported exothermic values for anode are 54 & 95.5 J/g and for the cathode 60 & 103 J/g for 10 and 200 cycles respectively. Changes in the cathode open circuit potential (OCP) reveals a decreasing amount of lithium content after cycling which is related to decreasing thermal stability. The decomposition temperature decreases for Li_xCoO_2 as the x value decreases. The decline in the thermal stability of the cell on overcharge is also due to both removal of lithium ions from the cathode and deposition over anode surface.

4. Abuse preventive measures

4.1 Gas evolution as Current Interrupter

In (Abe, 2006) reported the development of electro-conduction membrane (ECM), an alternative to solid electrolyte interphase (SEI) film. The electro-conductivity of ECM improves cathode cycleability, formerly known as overcharge protection proofs. For example, Benzene derivatives (biphenyl and o-terphenyl) and heterocylic compounds (furon, thiophene, N-methyl pyrrole and 3, 4-ethylenedioxythiophene), by virtue of their lower oxidation potentials than those of electrolyte solvents, decompose on the cathode surface and form thin film. The author describes biphenyl compound could serve well as overcharge proof since the gas generated at higher voltage (decomposition at 4.5V verses Li/Li+) is released through the cell safety cap. Yoshino reports the use of cyclohexyl benzene which evolves hydrogen and activates current interrupter device (CID) and shuts off the cell current. The application of biphenyl (Moli/NEC) and pyrocarbonate (SONY— evolves CO_2) were also reported in (Yoshio, 2001, 2002).

4.2 Flame retardant as additive to electrolyte

Blomgren (Blomgren, 2003) discusses on the additives which serves to lower the flammability (Flame retardants-FRs) of the electrolyte. The author points out that flames generally require the presence of materials which promote chain reactions for self-sustaining, hence majority of workers sought materials that can break the chain reactions (known as chain breakers) to avoid battery failures. It is reported (Wang et al., 2001) that the thermal stability is improved by the use of Trimethyl phosphate (TMP) containing electrolyte and for the one with 1 mol/dm^3 $LiPF_6$/EC + PC + DEC +TMP (30 + 30 + 20 + 20) electrolyte composition the cell exhibited good thermal stability. They state that the use of a minimum of TMP in a disordered carbon negatives improves further the thermal behaviors. In several cases the FRs brings adverse impacts on the cell performances due to their extra weight fraction in the electrode. Comparatively costly FRs such as fluorinated alkyl phosphates and hexamethoxy cyclotriphosphazene are more promising with minimal impacts on cell performances. The report in (Xiang et al., 2007) states that a cost effective, highly efficient retardant additive dimethyl methylphosphonate (DMMP) to 1M$LiPF_6$/EC+DEC electrolyte system provides total non-flammability for a 10wt. %DMMP addition. The addition of DMMP causes little damage on the cell electrochemical performance and more promising for safety to lithium ion batteries.

4.3 Redox shuttle

The molecule which oxidizes to form a radical cation at high cell voltage at the positive electrode diffuse to the negative electrode where it reduces into neutral molecule and shuttles back to the positive electrode, a phenomenon called as redox shuttles. In (Chen et al., 2005) it is pointed out that a chemical redox shuttle additive to the electrolyte is shown to provide overcharge protection. The molecule 2, 5 diterbutyl-1, 4-dimethoxy benzene, provides overcharge and overdischarge protection for hundreds of charge-discharge cycles in both single cells and series connected cells. Yoshino (Yoshino, 2001, 2002) has described several of these materials for application in lower currents. The materials such as veratrole(Sony), difluoroanisole (LG chemical), bipyridyl(Sanyo) and biphenyl carbonate(Sanyo and Ube) were used beneficially in lithium ion batteries.

4.4 Dopants and coatings

The electro active particles or the electrodes are modified to achieve high cycle life and hazard free batteries. One way is doping a part of 'Co' in $LiCoO_2$ with some other metal (Needham et al., 2007 & Veluchamy et al., 2001) the other one is coating on the surface of $LiCoO_2$ particles (Kim et al., .2005; Nozaki, et al., 2009; Cho, 2004) and the third one is giving polymer coating **(**Oyama et al., 2009). Usually the electrode materials are modified by incorporating carbons, $AlPO_4$, SnO_2, Al_2O_3, ZrO_2 and TiO_2 during or after the synthesis usually through heat treatment. For example, Lee et al., (2007) reported that Li-ion cells with olivine $LiCoPO_4$ grown over $LiCoO_2$, showed only 10% swelling at 4.4V, whereas those containing bare sample showed 200% volume increase during storage at 90°C for 5h. In addition nail penetration test results of the cell containing Olivine, $LiCoPO_4$, grown in $LiCoO_2$ at 4.4V, did not exhibit thermal runaway with a cell surface temperature of ~80°C. However, the cell containing bare $LiCoO_2$ showed a burnt-off of the pouch cell with a temperature reaching above 500°C. Cho described in (Cho, 2004) the dependence of thermal stability of $LiCoO_2$ cathode to the coating thickness of $AlPO_4$ over the cathode. As the thickness is increased the cell safety improved even for a 2C rate overcharged cell with no signs of thermal runaway. The author believed that the development of such coating acts as a replacement for protection circuit mode (**PCM**) for lithium ion battery (PCM consists of a material with a positive temperature coefficient and protective circuits that blocks overcharging above 4.35V, over discharging below 2V, and overcurrent above 1C)

4.5 Other physical devices

A patent by (Okutoh & Tadashi, 2001) describes that a flat sheet of lead taken out from a positive temperature coefficient (PTC) element incorporated inside the battery is connected to a protection circuit element for detecting any abnormality from overcharging, overdischarging, overcurrent, and unusual temperature to cut-off the current passing through the cell. Positive temperature coefficient (PTC) element installed inside the cell, whose resistance increases several fold in response to surge current during cell abuse, followed by this the cell temperature rises due to I_2R loss which causes sudden fall of current flow consequently preventing the cell failure. Contrary to (PTC) element, negative temperature coefficient (NTC) element decreases its resistance with temperature. This characteristic is used to monitor inside cell temperature and hence helps to understand any unwanted reactions inside the cell. Various companies incorporating protection circuit module (PCM/PCB) to keep safe Li-Ion/Polymer battery from overcharge, overdischarge, and accidental battery explosion due to its extra high energy density are available in the market(BATECH Korea INC. & Co., Ltd in Tokyo, Japan). During their discussion on safety mechanism in (Balakrishnan et al., 2006) the authors have described various devices including the use of thermostat or temperature cut-off (TCO) element, which serves to terminate current flow when the temperature reaches a preset value.

5. Experimental

5.1 Pouch cell construction

The cell used for safety tests is a commercial, rectangular, pouch cell (1000mAh) of dimensions 60mm x 33mm x 4mm. The data provided by the manufacturer reveals that the cathode constituents are $LiCoO_2$, super p black (SPB) and polyvinylidene difluoride (PVDF)

coated over aluminum current collector in the wt ratio 94, 3, and 3 % respectively. The particle size of Li_xCoO_2 is 20μm. The anode material constituents are coated over a copper current-collector and comprised a blend made up of mesocarbon microbeads and PVDF in a wt ratio 92 and 8%. The electrolyte (Techno Semichem.) is 1.12 M $LiPF_6$ with 2wt% vinylene carbonate (VC) dissolved in ethylene carbonate (EC) and ethyl methyl carbonate (EMC) mixed in 1: 1(V/V)) ratio. The separator is a non-woven poly propylene separator. Electrodes and electrode materials removed from the cell were used for the obtaining thermal and structural data.

5.2 Instrumental procedures

The pouch cells were charged and/or overcharged to a set voltage using the current source from Digatron (Germany) either for heat-treatment experiments or for abuse tests. For measuring the temperature variation with time during abuse tests experiments an electronic digital recorder with a thermocouple probe was fixed tightly over the surface of the test cells. Designed and locally fabricated equipments (Fig. 1 & Fig. 2)) were employed for carrying out the nail penetration test and impact tests. To acquire data for 1C rate (Fig. 3) or 3C rate (Fig. 4) the batteries were overcharged by using current source from Digatron.

Fig. 1. Nail penetration Test equipment.

The nail penetration test (Fig.5) was performed on the cell noted as Cell-3 using a nail (50mm long, 5mm diameter) at a penetration rate of 5mm/s at the centre of the cell. The impact test (Fig. 6) was carried out by placing a rod (15.8mm diameter and 50mm. length) on the cell which was kept on a flat iron plate and over that an iron cylinder (~ 15 cm x 10 cm) weighing 9.1kg was allowed to fall from a height of ~ 610mm onto the cell named as Cell-4. The nail penetration and overcharge test chambers were provided with glass door to view the experiments. In order to have an insight into the materials formed during abuse tests, a pouch cell was charged to a cut-off voltage of 4.5V and then heated to 400°C in a furnace under argon atmosphere at a rate of 5°C/min. The heating was then switched off to cool the cell down spontaneously to room temperature. The heating temperature 400°C was chosen as this temperature is close to the cell temperature of pouch cell during/near explosion. Also, the observation (Cho et al., 2003) that the internal cell temperature of abused cell is always higher by 80°C over surface of the cell has also been taken into consideration.

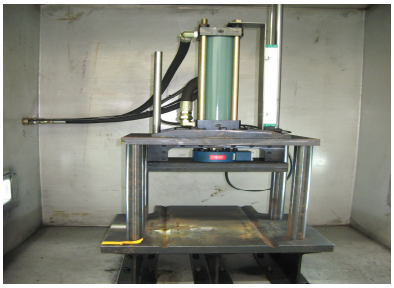

Fig. 2. Impact test equipment

A Philips 1830 X-ray diffractometer with nickel filtered Cu Kα radiation at a scan rate of 0.04°/s over 2 theta range 10°— 80° was used to analyze the cathode material heated to 400°C.

Differential scanning calorimetry (DSC-Q1000) and thermo-gravimetry (TGA-Q600) from TA Instrument USA which use data processing program universal analysis 2000 were used to carry out thermal behavior of the samples. The sample holders are made of alumina and aluminum for DGA and DSC, respectively. Electrode material weighing ~8 to 10mg was kept in open alumina holder and ~7 to 9mg was crimp sealed in aluminum holder; both experiments were carried out at a scan rate of 5°C/min in a nitrogen atmosphere. The cell opening and extraction of the cathode material for these experiments were carried out in a dry-room maintained at ~21°C with dew point temperature ~ 65°C.

A portion of the electrode cut in size 20mm x10mm washed first with dimethyl carbonate and then with acetone to remove any electrolyte in the electrode. It was then kept immersed in 50 ml of distilled water for 1h and the solution was subjected to identify presence of any carbonate ions in the cathode using Ion chromatography (IC). Ion chromatography was also carried out for a solution prepared by adding 1ml of the battery electrolyte (1.12 M $LiPF_6$ in VC/EC/EMC) in 9 ml of water giving a rest time of 30 minute in order to find out the presence of other ions in the electrolyte.

6. Results and discussion

6.1 Over charge behavior

6.1.1 Overcharge at 1C rate

The overcharge behaviors of a pouch cell designated as Cell-1 at 1C rate for 2.5h is presented in Fig. 3 along with photograph of the abused cell. During the first hour, the cell voltage shifts from 4.2 to 4.5V. Consequently, the electrode gets polarized giving rise to the following processes. As the potential of Li_xCoO_2 electrode shifts to more positive value, the deintercalation of lithium ions proceeds along with the oxidation of Co^{3+} into unstable Co^{4+}, which dissolves in the electrolyte. The dissolution of Co^{4+} accelerates with time as the potential shifts to a more positive value and results in damage to Li_xCoO_2 crystal, a process which is related to fading of cell capacity (Oh et al., 2004). This polarization process is followed by a thermal process. As the x in Li_xCoO_2 shifts from 0.45 to 0.3, a large anisotropic volume change of 3% occurs due to the phase transition between hexagonal and monoclinic

H1-3 phases (Jang et al., 2002 & Amatucci et al., 1996). Such crystal-phase change is also presumed to induce thermal stability of the positive electrode (Saito et al., 1997).

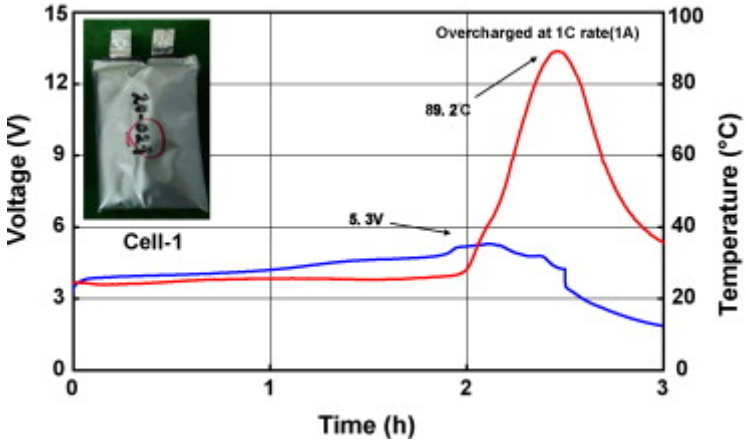

Fig. 3. Voltage and thermal behaviour of Cell-1 on overcharge at 1 C rate, (Doh et al, 2008)

As the cathode is completely de-lithiated, the cell voltage moves above 4.5V, the ionic conduction completely ceases, and the passage of current through the cell becomes purely ohmic resulting in heat generation due to I^2R loss. The poor heat dissipation of the cell components causes an exponential increase in cell temperature (Saito et al., 1997)), which induces decomposition of Li_xCoO_2 according to equation. (1). As discussed in section 6.15 the overcharged cathode Li_xCoO_2 ,as $x \rightarrow 0$,decomposes into Co_3O_4 and oxygen, (Dahn et al., 1994). At higher temperatures, the liberated oxygen and Co_3O_4 promotes combustion of carbonaceous materials. Since the electrolyte contains organic solvent, Co_3O_4 will be reduced to CoO (Mac Neil, 2001). The extent of conversion depends on the probability of contact between Co_3O_4 and the reductive organic species available during the combustion process. The Fig. 3 also shows an abrupt triggering of heat after 2h of charging is possibly be due to meltdown of the separator (~125°C for polyethylene and ~155°C for polypropylene) (Tobishima et al., 1999)leading to a cell short-circuit. As the passage of overcharge current ends at 2.5h, the joule heating also ceases. Finally both cell voltage and temperature start decline from the peak values 5.3V and 89°C, respectively. As reported in (Cho., 2003) the inner cell temperature will be 169°C. The disconnected battery from the abuse tests was subjected to charge but found the cell could not be recharged and has undergone thermal runaway.

6.1.2 Overcharge at 3C rate

The overcharge behaviors of the pouch cell designated as Cell-2 recorded at 3C rate (current-3A) and a photograph of cell used for the tests are presented in Fig. 4. After 0.7h, there appears to be a change in voltage and temperature behavior of the cell. At the ~ 0.8h, the cell temperature and voltage move above 300°C and 12V respectively. The sudden drop of cell voltage after reaching 12V implies perfect short circuiting of the electrodes, possibly due to melt down of the separator. The temperature and the cell voltage are so high to cause

all the erroneous process (described for the Cell-1) for the cell destruction. Meltdown of the separator and combustion of the organic electrolyte with the released oxygen would have been instantaneous to cause volume expansion and violent explosion. The maximum dc power attained is ~39W and the cell surface temperature reaches 300°C.

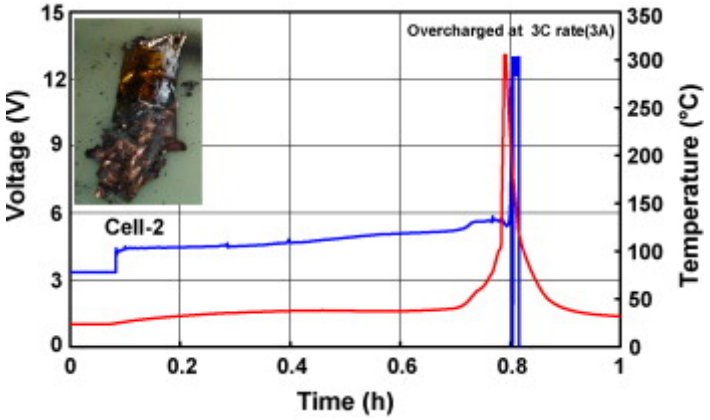

Fig. 4 Voltage and thermal behavior of cell Cell-2 on overcharge at 3C rate, (Doh et al, 2008).

6.1.3 Nail penetration test

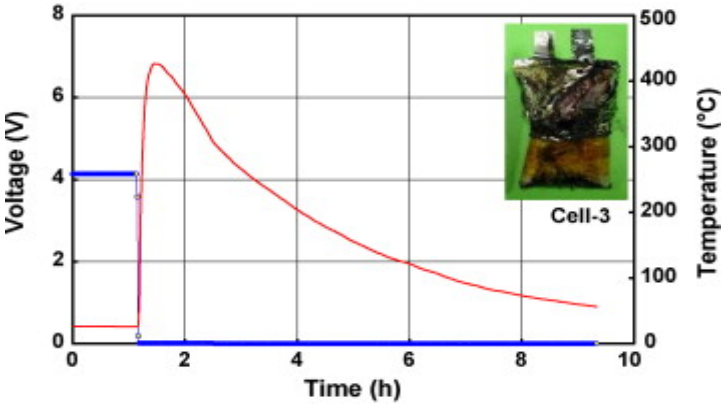

Fig. 5. Voltage and thermal behaviour of Cell-3 on nail penetration test, (Doh et al, 2008).

The cell designated as Cell-3 was subjected to nail penetration and a photograph of the cell taken after the test is presented in Fig.5. The Figure shows a constant voltage and temperature before the test is conducted. At the instant the experiment is started, the voltage falls to zero and the surface temperature of the cell shoots up to 420°C which could only be attributed to a high surge of discharge current resulting in a high joule heat followed by separator meltdown and contact of the anode and cathode. In the case of overcharge tests, the electrodes are charged at a known current, whereas, in nail penetration tests the quantity of the discharge current flowing through the nail is not known. The temperature of the cell

reaching 420°C shows the intensity of the discharge current in the nail penetration test which could have been much higher than that in overcharge test. The current flowing through nail can be compared with well-known dendrite shorting. The usual discharge product $LiCoO_2$ along with Co_3O_4 and O_2 from the decomposition of de-lithiated cathode Li_xCoO_2 could be expected, after combustion process. In addition, a trace quantity of CoO could be expected (section 6.15). The cell does not explode violently as the nail has made a partial way for the release of gaseous materials and the cell appears to have expanded as evident from the figure (Fig.5).

6.1.4 Impact tests

In nail penetration tests, the nail makes a direct contact between the anode and cathode. But in the impact tests the cylindrical rod is kept horizontally over the cell which crushes the cell at the centre. Since the action is expected to expand and tear the separator that makes contact between positive and negative electrodes. A high discharge current will flow between the anode and cathode of the cell. The highest surface temperature noted is 161°C (the internal temperature will be around 241°C). As the internal portion of the cell is opened the gaseous products formed will be easily released from the cell and there will be less severe effect on the environment. The thermal behavior along with a photograph of the impact tested cell designated as Cell-4 is presented in Fig. 6.

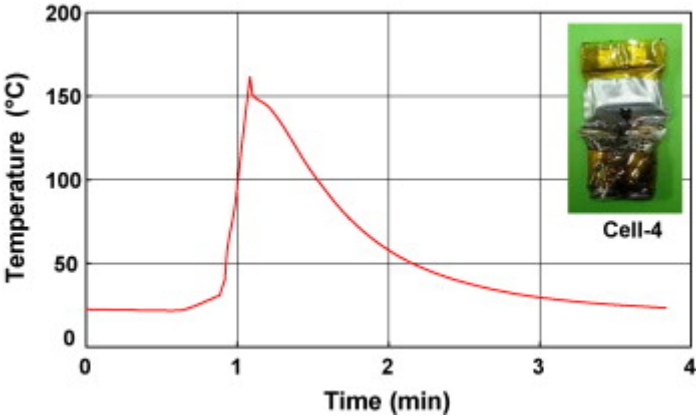

Fig. 6. Thermal behavior of Cell-4 on impact test; (Doh et al, 2008).

6.1.5 XRD analysis of the cathode material exposed to high temperature.

The general equation that govern the decomposition of Li_xCoO_2 may be represented by the equation

$$Li_xCoO_2 \rightarrow xLiCoO_2 + \left(\frac{1-x}{3}\right)Co_3O_4 + \left(\frac{1-x}{3}\right)O_2 \quad (1)$$

This shows that during overcharging, highly de-lithiated cathode material Li_xCoO_2, as $x \rightarrow 0$, decomposes into Co_3O_4 and O_2 gas. In a partially delithiated cathode, of $Li_{0.5}CoO_2$ (4.2V cells), the possible products are $LiCoO_2$, Co_3O_4 and O_2 gas. The XRD patterns of cathode

material Li_xCoO_2, unheated (4.5V cell), heated (4.5V cell) and $LiCoO_2$(3V cell for comparison) are presented in Fig. 7. The Bragg peaks appearing for the unheated cathode of 4.5V cell show a change in the crystal parameters for $LiCoO_2$, which can possibly be attributed to a de-lithiated state. After heat treatment, the XRD pattern shows disappearance of many peaks corresponding to the parent sample. The resultant material after heat treatment has lost its crystallinity, as evident from the XRD pattern. The Bragg peaks of $LiCoO_2$, Co_3O_4 overlap in many cases, except in the region of Co_3O_4(220) peak near 31.1°. The appearance of this peak in the heat treated sample confirms the formation of Co_3O_4 upon decomposition of Li_xCoO_2 (MacNeil., 2001). The effective conversion of Co_3O_4

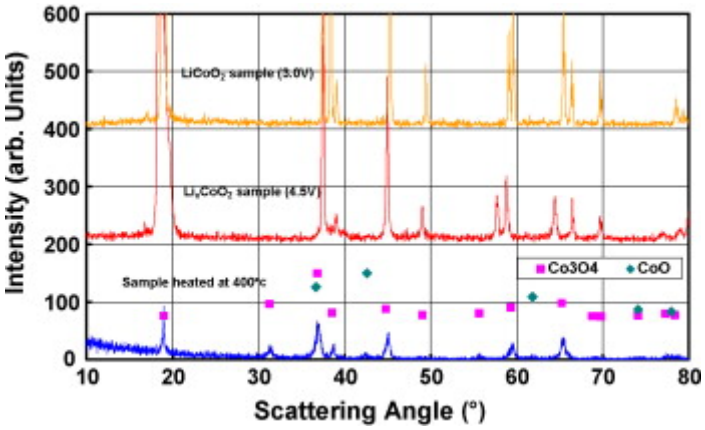

Fig. 7. XRD patterns of cathodes $LiCoO_2$ (3V cell), Li_xCoO_2 (4.5V cell) and heat-treated cathode (4.5V cell) at 400°C, (Doh et al, 2008).

into CoO by the reductive action of organic solvent becomes likely. On the other hand, the probability of the formation of a trace quantity of CoO from the reduction of Co_3O_4 by the carbonaceous residues present in the cathode material may be attributed to the weak peak appearing in the XRD pattern. The formation of $LiCoO_2$, Co_3O_4 and CoO has been reported in (MacNeil & Dahn, 2001, 2002) from a thermal study of $Li_{0.5}CoO_2$ with electrolyte. Since all the abuse tested cells contains electrolyte, the formation of a small quantity of CoO from the reduction of Co_3O_4 is expected by virtue of reducing power of solvent. In (Dahn et al., 1994) reported the thermal behavior of Li_xCoO_2, Li_xNiO_2, and $Li_xMn_2O_4$ materials and found that the amount of oxygen released into the electrolyte increases with decrease of x value. Hence a highly oxidized cathode could explode violently as the amount of oxygen released from the combustion reaction is enormous.

6.1.6 Thermogravimetric analysis

The TGA curves obtained for electrodes charged to different temperature are presented as Fig. 8. The figure shows the extent of weight loss at three different regions. In the region around 100°C where the weight loss may either be due to evaporation of the electrolyte solvent or combination of evaporation of the solvent and weight loss due to oxidation reaction. If there is exothermic energy release in any region that will be understood from the DSC data. In the region between 200 and 400°C the weight loss is attributed to

decomposition of Li_xCoO_2 into $LiCoO_2$, Co_3O_4 and oxygen. The reduction of Co_3O_4 into lower cobalt oxide or to cobalt depends on the extent of electrolyte solvent present in the sample. The liberated oxygen oxidizes the carbonaceous materials releasing carbon dioxide and energy. In (MacNeil & Dahn, 2001) the authors analyzed the XRD pattern of $Li_{0.5}CoO_2$ sample heated with and without organic solvent using ARC and demonstrated that the former one even at lower temperature (275°C), not only produces $LiCoO_2$ and Co_3O_4 but also shows the presence of $Li_xCo_{(1-x)}O$. Since the amount of lithium (Li) is very small, the authors refer $Li_xCo_{(1-x)}O$ as CoO. Fig. 8 shows that the highly charged electrode materials of 4.20 and 4.35V cells to undergo pronounced weight loss compared to electrode materials of cells charged to lower voltage cells (3.85 and 3.95V). The highly charged material with low value of lithium could behave well like an oxidizing agent towards the electrolyte which may lead to the formation of less quantity of $LiCoO_2$ and Co_3O_4, but with larger proportion of CoO.

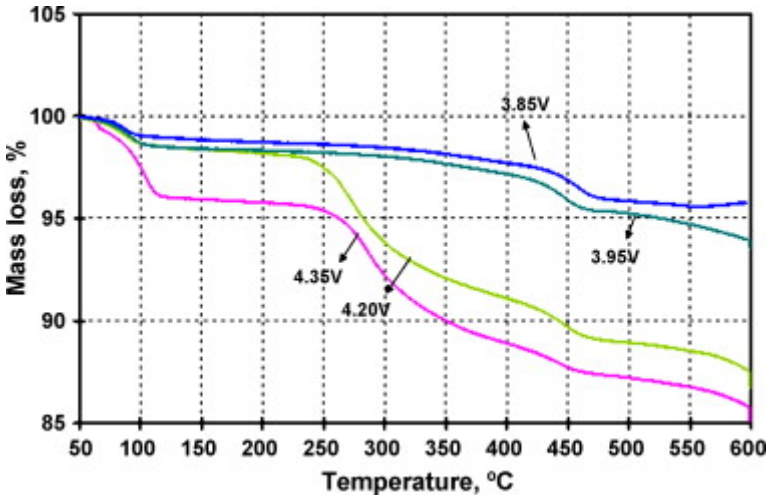

Fig. 8. TGA curves for the different cathode materials; (veluchamy et al., 2008).

6.1.7 Differential Scanning calorimetry

The DSC spectrums representing the heat flow with temperature for the charged cathode are presented as Fig.9. The figure shows that the cathodes of cells charged to 3.85 and 3.95V have no thermal peaks in the low temperature region whereas the cells charged to 4.20 and 4.35V have well defined exothermic peaks of the order of 4.9 and 7.0 J/g respectively below 100°C. Even though the intensity of these peaks is low, they arouse more curiosity as no such peaks in this temperature region have so far been reported. In (MacNeil and Dahn, 2001) the authors made in-depth thermal study of the cathode materials with calculated quantity of organic solvents. In this present study the cathode material containing electrolyte was used as such for obtaining thermal data. The exothermic energy released is assumed to be due to the reaction between the oxide cathode material and the organic electrolyte present in it. The heat energy calculated from DSC spectrum for the two cathodes materials are 83 and 80 J/g between 125 and 250°C and above 250°C the values are 81 and 17 J/g for the respective cathode materials of 4.20 and 4.35V cells. The lower exothermic energy

release of cathode material of 4.35V cells at higher temperature region may be associated with early history of the sample such as decomposition of the cathode material/electrolyte during overcharging and decomposition at low temperature region in DSC itself.

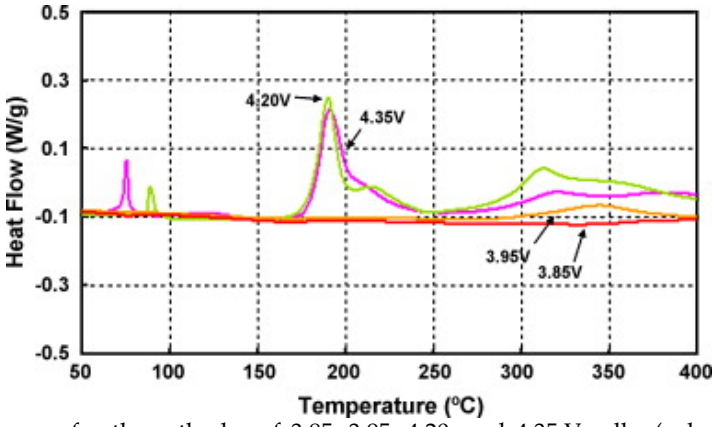

Fig. 9. DSC scans for the cathodes of 3.85, 3.95, 4.20, and 4.35 V cells, (veluchamy et al., 2008).

6.1.8. Ion Chromatography

Through XPS spectra the authors in (Dedryvère et al, 2007) identified a passivation film of LiF on the surface of positive electrode material Li_xCoO_2 of the cell $LiCoO_2/C$ charged to different cell voltages, which increased progressively from ~10% at 3V up to 18% at 4.2V. In our experiment the electrode is washed first with organic solvent to remove the organic electrolyte along with dissolved inorganic salt present in the electrolyte.

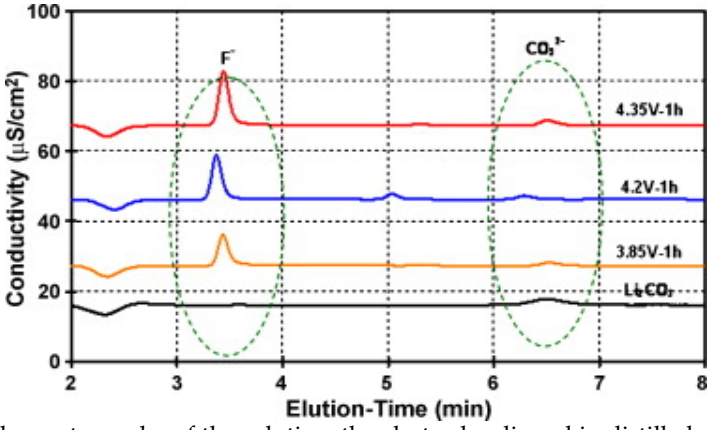

Fig. 10. Ion chromatography of the solution: the electrodes dipped in distilled water; Li_2CO_3 dissolved in distilled water. (veluchamy et al., 2008).

Then the electrode is immersed in distilled water for 1 hour so that the ionic materials present in SEI film could be dissolved in water and identified using Ion

Chromatography(IC) technique (Fig. 10).The curves show the presence of ionic carbonates and ionic fluoride. Again 1ml of fresh battery electrolyte (1.12 M $LiPF_6$ in VC/EC/EMC) added to 9 ml of distilled water with a 30 minute rest time was analyzed and presented in Fig.11.The figure shows the probable ionic species which may get incorporated in the electrode materials. Comparison of Fig.10 and Fig 11 shows the peak at 5 minute elution time in the IC of 4.2V, electrode immersed in distilled water for 1 h is due to the presence of chloride impurities present in the electrolyte. Hence it may be concluded that the possible materials present over the surface of the electrode material are LiF, Li_2CO_3 and trace quantity of LiCl. Even though LiCl could have same role as LiF, only LiF is considered for discussion as the contribution of LiF will be greater compared to LiCl.

6.1.9 Mechanism of SEI film break-down

During overcharge process the x value of the cathode steadily changes from 0.45 to 0.3. The electrode faces an instability and passes through a phase change from hexagonal structure to monoclinic H1-3 accompanying a large anisotropic volume change (~3%) (Jang et al., 2002 & Amatucci and Tarascon, 1996). Over the highly positive unstable electrode during the phase change process protons are generated due to oxidation of the solvent by the cathode. This proton interacts with LiF deposit present in the SEI film and forms H_2F_2. The acidic species HF_2^- formed from H_2F_2 then reacts with Li_2CO_3 present in SEI film making it more fragile (Lorey et al, Doh et al., 2008 & Saito et al., 1997). The reactions are presented as equation (2) and (3).

$$LF + \text{-H-} \rightarrow Li^+ + HF \quad (2)$$

$$Li_2CO_3 + 2HF \rightarrow 2LiF + CO_2 + H_2O \quad (3)$$

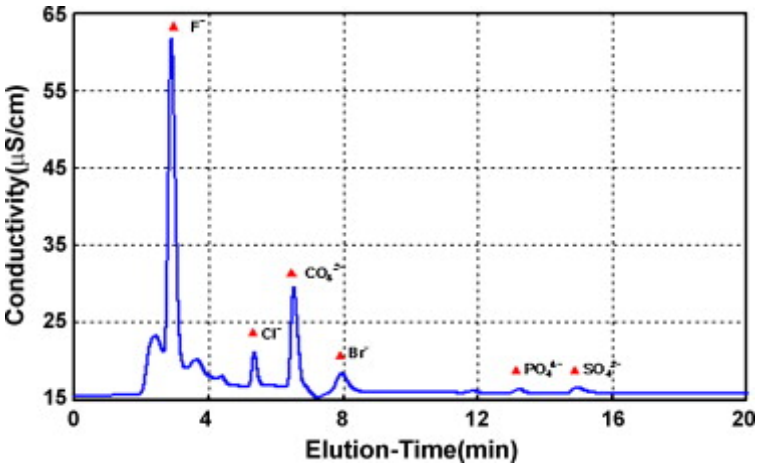

Fig. 11. Ion chromatography of the electrolyte added to distilled water, (Veluchamy et al., 2008).

These reactions will convert the rigid SEI layer into fragile one especially as liquid phase which could allow easy diffusion of the available organic solvent from the bulk into the surface of the oxide cathode. Now the oxidative reaction between the reactive cathode and

the solvent causes release of exothermic heat flow of low magnitude even at low temperature region near 100°C. This low heat pulse acts as a prelude for the large scale release of oxygen from the cathode to an eventual catastrophic exothermic reaction which accentuates damage to the cell, even causes explosion. This explanation may be compared with the experimental findings reported earlier that only highly charged batteries are prone to explosion during battery abuses (Doh et al 2008).

7. Conclusion

A. Results from abuse analysis

I) The extent of cell deterioration or the resultant explosion depends on the quantity of charge/discharge current passing through the charged cell.

II) At the instant the battery is abused the processes such as rise of joule heat, break down of SEI film, release of oxygen from cathode, oxidation of plated lithium over graphite anode takes place consecutively leading to combustion of organic molecule resulting in cell failure or explosion.

III) The internal shorts such as nail penetration, impact and dendrite short could cause catastrophic damage to the cell compared to external short.

IV) The extent of exothermic reaction is greater for (a) when $x \rightarrow 0$, in Li_xCoO_2, (b) amount lithium plated over the graphite anode and (c) the quantity of organic electrolyte present in the cell.

V) At higher cycles the lithium plated over graphite anode is higher than the intercalated lithium which causes the cell to experience greater heat energy released during battery abuse.

VI) Even though binders are in close contact with lithium metal, lithium prefers to react with solvent rather than with binder.

B. State of the art

I) The search for electrolyte additives to arrive non-degradable electrode-electrolyte interface film with cycling is to serve as an alternative one to SEI film for providing stability to the electrode materials.

II) Additives to the electrolytes such as low resistant flame retardants, current interrupter materials and redox shuttles are expected to further reinforce safety of lithium ion batteries.

III) Dopants to cathode materials and coatings to electrodes and electrode materials of cathodes and anodes are a noteworthy development and are expected to contribute further for the stability of electrodes.

IV) Physical devices such as Positive temperature coefficient(PTC) and Negative temperature coefficient (NTC), developed may further has scope for improvement to check/monitor battery condition.

V) Present activity on the development of non flammable electrolyte is expected to reach a mile-stone which will be a final solution for making electric vehicle a more safe.

C. Need of the Future

Heat dissipating pouch/metal container, state of charge monitor, thermally more stable cathodes, anode without dendrite or plating with cycles, non flammable electrolytes are some of the areas wherein the researchers will continue, to arrive a safe and ultimate lithium ion battery for use in electric vehicles, domestic utilities and also in emerging non-conventional energy sectors.

8. References

Abe, K.; Ushigoe, Y.; Yoshitake, H & Yoshio, M. (2006). Functional Electrolytes: Novel type additives for cathode materials, providing high cycleability, *Journal of Power Sources*. Vol. 153, (July 2006) 328-335.

Abraham, K. M.; Pasquariello, D. M. & Willstaedt, E. B. (1990). N-butylferrocene for overcharge protection of secondary lithium batteries, *Journal of The Electrochemical Society, Vol.* 137, No. 6, (June 1990) 1856-1857.

Amatucci, G. G.; Tarascon, J. M. & Klein, L. C. (1996). Cobalt dissolution in $LiCoO_2$-based non-aqueous rechargeable batteries, *Solid State Ionics*, *Vol. 83, No.1-2*, (*January 1996) 167-173*.

ANSI News and publications. New York, November 20, 2006.

Aurbach, D.; Levi, M. D.; Levi, E.; Markovsky, B.; Salitra, G. & Teller. H. (1997). Batteries for Portable Applications and Electric vehicles, in: Holms, C. F.; Landgrebe, A. R.(Eds.),*The Electrochemical Society Proceedings Series*, PV 97-18, Pennington, NJ, 1997, P.941.

Balakrishnan, P. G.; Ramesh, R. & Prem Kumar, T. (2006), Safety mechanisms in lithium ion battery, 15) *Journal of Power Sources,* 155 (February, 2006) 401- 414.

Biensan, P.; Simson, B.; Peres, J. P.; Guibert, A. D.; Broussely, M.; Bodet, J. M.& Perton, F.(1999). On safety of lithium-ion cells, *Journal of Power Sources*, Vol. 81-82, (September 1999) 906-912.

Blomgren, G. E.(2003). Liquid electrolytes for lithium and lithium-ion batteries. *Journal of Power Sources*, Vol. 119-121, (June 2003) 326-329.

Cho, J. (2003). Improved thermal stability of $LiCoO_2$ by nanoparticle $AlPO_4$ coating with respect to spinel $Li_{1.05}Mn_{1.95}O_4$, *Electrochemistry Communications*, Vol. 5, No. 2, (February 2003) 146-148.

Cho, J. (2004). Dependence of $AlPO_4$ coating thickness on overcharge behavior of $LiCoO_2$ cathode material at 1 and 2 C rates, *Journal of Power source,* Vol. 126, Issues 1-2, 16 (February 2004) 186-189.

Chen, J.; Buhrmester, C. & Dahn. J. R (2005). Chemical Overcharge and Overdischarge Protection for Lithium ion Batteries, *Electrochem. Solid state letters*, Vol. 8, issue 1 (2005)A 59-A 62.

Dahn, J. R. (2001) Lithium ion battery Tutorial and update: *Power* 2001, Anaheim, CA, September 30, 2001

Dahn, J.R.; Fuller, E.W.; Obrovac, M. & Sacken, U. V. (1994). Thermal stability of Li_xCoO_2, Li_xNiO_2 and λ-MnO_2 and consequences for the safety of Li-ion cells, *Solid State Ionics*, Vol. 69, No. 3-4, (August, 1994) 265-270.

Dedryvère, R.; Martinez, H.; Leroy, S.; Lemordant, D.; Bonhomme, F.; Biensan, P. & Gonbeau, D.(2007). Surface film formation on electrodes in a $LiCoO_2$/graphite cell, A step by step XPS study, *Journal of Power Sources*, Vol. 174, Issue 2, 6 (December 2007) 462-468.

Doh, C. H.; Kim, D. H.; Kim, H. S.; Shin, H. M.; Jeong, Y.D.; Moon, S. I.; Jin, B. S.; Eom S. W.; Kim, H.S.; Kim, K.W.; Oh, D. H. & Veluchamy, A.(2008). Thermal and electrochemical behaviour of C/Li_xCoO_2 cell during safety test. *Journal of Power Sources*, Vol. 175, Issue 2, 10 (January 2008) 881-885

Fouchard, D.; Xie,L.; Ebner,W.& Megahed,S. A.(1994). Rechargeable lithium and lithium ion (RCT) batteries in: Megahed, S. A. (Ed), *Electrochemical Society*. PV 94-28 Miami Beach, Florida, October 1994.

Jang, Y-I.; Dudney, N.J.; Blom, D.A. & Allard, L. F. (2002). High-Voltage Cycling Behavior of Thin-Film $LiCoO_2$ Cathodes. *Journal of The Electrochemical Society,* 149 (2002) A1442-1447.

Kim, J.; Kim, B.; Lee, J-G; Cho, J. & Park. B. (2005). Direct carbon-black coating on $LiCoO_2$ cathode using surfactant for high-density Li-ion cell, *Journal of Power Sources*, Vol. 139, No. 1-2, 4 (January 2005) 289-294

Kim, J.; Noh, M.; Cho, J.; Kim, H. & Kim, K.B. (2005). Controlled Nanoparticle Metal Phosphate (Metal = Al, Fe, Ce, and Sr) coating on $LiCoO_2$ cathode materials. *Journal of The electrochemical society*, Vol. 152, No 6(2005) A1142- A1148.

Kitoh, K. & Nemoto,H. (1999). 100 Wh Large size Li-ion batteries and safety tests, *Journal of Power Sources*. Vol. 81-82, (September 1999) 887-890.

Lee, H.; Kim, M. G & Cho. J.(2007). Olivine $LiCoPO_4$ phase grown $LiCoO_4$ cathode material for high density Li batteries. *Electrochemistry communications,* Vol. 9, Issue 1, (January 2007), 149-154

Leising, R. A.; Palazzo, M. J.; Takeuchi, E. S. & Takeuchi, K.J. (2001). Abuse testing of lithium-ion batteries characterization of the overcharge reaction of LiCoO2/graphite cells, *Journal of The Electrochemical Society* (2001), 148(8), A838-A844.

Leroy, S.; Martinez, H.; Dedryvère, R.; Lemordant, D.& Gonbeau, D. (2007). Influence of the lithium salt nature over the surface film formation on a graphite electrode in Li-ion batteries: An XPS study, *Applied surface science*, 253(2007) 4895-4905.

Lin, H.-P.; Chua, D.; Salomon, M.; Shiao, H. C.; Hendrickson, M.; Plichta, E.& Slane, S. (2001), Low-Temperature Behavior of Li-Ion Cells, *Electrochemical and solid state letters*, Vol. 4, Issue 6, (April, 2001) A71-A73.

Liu, X.; Kusawake, H. & Kuwajima, S. (2001). Preparation of a PVdF-HFP/polyethylene composite gel electrolyte with shutdown function for lithium-ion secondary battery, *Journal of Power Sources*, Vol. 97-98, (July 2001), 661-663.

MacNeil, D. D. & Dahn, J. R. (2002). The reactions of $Li_{0.5}$ CoO_2 with non aqueous Solvents at elevated temperature, *Journal of The electrochemical society,* Vol. 149, No. 7 (2002) A912-A919.

MacNeil, D. D. & Dahn J.R. (2001). The Reaction of Charged Cathodes with Nonaqueous Solvents and Electrolytes, *Journal of The Electrochemical Society* 148 (11) A1205-A1210 (2001).

Maleki, H.; Deng, G.; Anani, A. & Howard. (1999). Thermal stability studies of Li-ion cells and components. *Journal of The electrochemical society*, Vol. 146, Issue 9, (September, 1999) 3224-3229.

Needham, S.A.; Wang, G.X.; Liu, H.K.; Drozd, V.A. & Liu, R.S, (2007). Synthesis and electrochemical performance of doped $LiCoO_2$ materials, *Journal of Power Sources*, Vol. 174, No. 2, 6 (December 2007) 828-831.

Nozaki, H.; Nagaoka,K.; Hoshi,K.; Ohta, N.& Inagaki, M. (2009). Carbon-coated graphite for anode of lithium ion rechargeable batteries: Carbon coating conditions and precursors, *Journal of Power Sources*, Vol. 194, No. 1, (October 2009) 486-493.

Oh, S.; Lee, J. K.;Byun, D;Cho,W. & Cho.B. W. (2004). Effect of Al_2O_3 coating on electrochemical performance of $LiCoO_2$ as cathode materials for secondary lithium batteries. *Journal of Power Sources*, Vol. 132, No 1-2, 20 (May 2004) 249-255.

Okutoh and Tadashi (2001). Battery protector having a positive temperature coefficient element, American patent No: 6177209. Publication on 01/23/2001.

Ota, H.; Kominato, A.; Chun, W.; Yasukawa, E. & Kasuya, S. (2002) Extended abstract no. 201, in: Proceedings of the *11th International Meeting on Lithium batteries*, Monterey, CA, 2002.

Ota, H.; Akai, T.; Namita, H.; Yamaguchi, S.& Nomura, M. (2003). XAFS and TOF–SIMS analysis of SEI layers on electrodes, *Journal of Power Sources*, Vol. 119-121, 1 (June 2003) 567-571.

Ota, H.; Kominato, A.; Chun, W.J.; Yasukawa, E.; Kasuya, S.(2003) Effect of cyclic phosphate additive in non-flammable electrolyte, *Journal of Power Sources*, Vol. 119-121, 1 (June 2003) 393-398.

Oyama, N.; Fujimoto,Y; Hatozaki, O.; Nakano,K.;Maruyama, K.;Yamaguchi,S.; Nishijima, K.;Iwase,Y.;Yoshikazu Kutsuwa (2009). New gel-type polyolefin electrolyte film for rechargeable lithium batteries, *Journal of Power Sources*, Volume 189, Issue 1, 1 (April 2009) 315-32.

Plichta, E.; Salomon, M.; Slane, S.; Uchiyama, M.; Chua, D.; Ebner, W.B. & Lin, H.W. (1987). A rechargeable Li/Li_xCoO_2 Cell, *Journal of Power Sources*, Vol. 21, No. 1, (August 1987) 25-31.

Richard, M. N. & Dahn, J.R.(1999). Accelerating rate Calorimetry Study on the Thermal Stability of Lithium Intercalated Graphite in Electrolyte, I Experimental, J. *Electrochemical Society, Vol.* 146, No. 6. (January, 1999) 2068- 2077.

Reimers, J. N& Dahn. J. R. (1992) Electrochemical and *in situ* R-ray Diffraction Studies of Lithium intercalation in Li_x CoO_2, *Journal of The Electrochemical Society* Vol. 139, No. 8 (August 1992) 2091-2097.

Saito,Y.; Kanari,K & takano,. K. (2001). Thermal studies of a lithium-ion battery, *Journal of Power Sources*, Vol. 68, No. 2, (October 1997), 451-454.

Saito,Y.; Takano, K.& Negishi, A. (2001). Thermal behaviors of lithium-ion cells during overcharge, *Journal of Power Sources*, Vol. 97-98, (July 2001) 693-696.

Spotnitz, R. & Franklin. (2003). Abuse behavior of high-power, lithium-ion cells, *Journal of Power Sources,* Vol. 113, No. 1, 1 (January 2003) 81-100.

Tobishima, S.; Takei, K.; Sakurai,Y. & Yamaki, J. (2000). Lithium ion cell safety, *Journal of Power Sources*, Vol. 90, No. 2, 1 (October 2000) 188-195.

Tobishima, S.; Yamaki, J. (1999). A consideration of lithium cell safety, *Journal of Power Sources*, Vol. 81-82, (September 1999) 882-886.

Under writers laboratories, Inc., standard for Safety 1642- Lithium batteries (April 1995).

Veluchamy, A.; Ikuta, H& Wakihara, M. (2001). Boron-substituted manganese spinel oxide cathode for lithium ion battery, *Solid State Ionics*, Vol. 143, No. 2, 2(June 2001)161-171.

Veluchamy, A.; Doh, C. H.; Kim, D. H.; Lee, J. H.; Shin, H. M.; Jin, B. S.; Kim, H. S.; Moon, S. I.(2009), Thermal analysis of Li_xCoO_2 cathode material of lithium ion battery, *Journal of Power Sources*, Vol. 189, No.1, 1(April 2009) 855-858.

Venugopal, G. (2001) .Characterization of thermal cut-off mechanisms in prismatic lithium-ion batteries, *Journal of Power Sources*, Vol. 101, No 2, 15 (October 2001) 231-237.

Venugopal, G; Moore, J.; Howard, J. & Pendalwar, S.(1999) Characterization of microporous separators for lithium-ion batteries, *Journal of Power Sources*, Vol. 77, No. 1, 1 (January 1999), 34-41.

Wainwright, D. (1995) Method of evaluating relative safety of porous electrode/electrolyte combinations to spot heating, *Journal of Power Sources*, Vol. 54, Issue 2, (April 1995) 192-197

Wang,Y.; Guo, X.; Greenbaum,S.; Liu, J.; & Amine, K.(2001). Solid Electrolyte Interphase Formation on Lithium-Ion Electrodes: A ^{7}Li Nuclear Magnetic Resonance Study. *Electrochem. Solid-State Lett.*, Vol. 4, No. 6, (April, 2001) A68-A70..

Wang, X.; Yasukuwa, E & Kasuya, S. (2001). Nonflammable Trimethyl Phosphate Solvent-Containing Electrolyts for lithium ion batteries-I. Fundamental Properties. *Journal of The Electrochemical Society*, Vol. 148. No. 10, (October 2001), A1058-41065.

Wu, M. S.; Chiang, P.J.; Lin, J. C. & Jan. Y. S. (2004), Correlation between electrochemical characteristics and thermal stability of advanced lithium-ion batteries in abuse tests—short-circuit tests, *Electrochimica Acta*, Vol 49, No. 11, 30 (April 2004), 1803-1812

Xiang, H.F.; Jin, Q.Y.; Chen, C.H.; Ge, X.W.; Guo, S. & Sun, J. H. (2007). Dimethyl methylphosphonate-based nonflammable electrolyte and high safety lithium-ion batteries, *Journal Power Sources*, 174(1) (2007)335-341.

Xiang, H.F.; Xu, H.Y.; Wang, Z.Z. & Chen C.H. (2007). Dimethyl methyl phosphonate (DMMP) as an efficient flame retardant additive for the lithium-ion battery electrolytes, *Journal of Power Sources*, 173(1) (2007)562-564.

Yamaki, J.; Baba, Y.; Katayama, N.; Takatsuji, H.; Egashira, M & Okada, S.(2003). Thermal stability of electrolytes with Li_xCoO_2 cathode or lithiated carbon anode. *Journal of Power Sources, Vol. 119-121, 1 (June 2003), 789-793.*

Yoshino, A.(2001), in*: Proceedings of the 3th Hawai battery conference*, ARAD Enterprises, Hilo, HI, 3 January 2001, p. 449.

Yoshino, A.(2002) in: *Proceedings of the 4th Hawai battery conference*, ARAD Enterprises, Hilo, HI 8 January 2002, p. 102.

Zhang, Z.; Fouchard, D & Rea, J.R. (1998), Differential scanning calorimetry material studies: Implications for the safety of lithium-ion cells. *Journal of Power Sources, Vol. 70, No. 1, 30* (January 1998), 16-20

Zheng, T.; Gozdz, A.S.& Amatucci, G.G.(1999) Reactivity of the solid electrolyte interface on carbon electrodes at elevated temperatures, *Journal of The Electrochemical Society*, 146(11) (1999) 4014-4018.

3

Plasma-Modified Polyethylene Separator Membrane for Lithium-ion Polymer Battery

Jun Young Kim[1,2] and Dae Young Lim[3]
[1]*Material Laboratory, Corporate R&D Center, Samsung SDI Co., Ltd. South Korea*
[2]*Dept. of Materials Science & Engineering, Massachusetts Institute of Technology, USA*
[3]*Fusion Textile Technology Team, Korea Institute of Industrial Technology, South Korea*
**E-mail addresses: junykim74@hanmail.net (J.Y. Kim); zoro1967@kitech.re.kr (D.Y. Lim)*

Abstract
This chapter describes the fabrication of a novel modified polyethylene (PE) membrane using plasma technology to create high-performance separator membrane for practical applications in rechargeable lithium-ion polymer battery. The surface of PE membrane as a separator for lithium-ion polymer battery was modified with acrylonitrile via plasma-induced coating technique. The plasma-induced acrylonitrile coated PE (PiAN-PE) membrane was characterized by X-ray photoelectron spectroscopy (XPS), scanning electron microscopy (SEM), and contact angle measurements. The electrochemical performance of lithium-ion polymer cell assembly fabricated with PiAN-PE membranes was also analyzed. The surface characterization demonstrates that the enhanced adhesion of PiAN-PE membrane resulted from the increased polar component of surface energy. The presence of PiAN induced onto the surface of PE membrane via plasma modification process plays a critical role in improving the wettability and electrolyte retention, the interfacial adhesion between the electrodes and the separator, and the cycle performance of the resulting lithium-ion polymer cell assembly. This plasma-modified PE membrane holds a great potential to be a promising polymer membrane as a high-performance and cost-effective separator for lithium-ion polymer battery. This chapter also suggests that the performance of lithium-ion polymer battery can be greatly enhanced by the plasma modification of commercial separators with proper functional materials for targeted application.

1. Introduction

As there is a growing demand for high-performance rechargeable batteries used in portable electronic equipments, mobile products, and communication devices, lithium-based batteries as a power source are of great scientific interests. Among many types of rechargeable batteries, lithium-ion polymer batteries hold potential to be used in industries, because they can be produced in a variety of forms and thus make it possible to fabricate readily portable batteries in required shapes for various electronic applications (Scrosati, 1993).

A separator placed between a cathode and an anode is one of critical components in the rechargeable lithium batteries. Its primary function is to effectively transport ionic charge carriers between the two electrodes as an efficient ionic conductor as well as to prevent the electric contact between them as a good electric insulator (Linden & Reddy, 2002; Besenhard, 1999). A separator should be chemically or electrochemically stable and have mechanical strength sufficiently enough to sustain battery-assembly processes (Besenhard, 1999; Zhang, 2007; Arora & Zhang, 2004). In addition, a separator has a significant effect on the manufacturing process and the performance of rechargeable lithium batteries. Commercially available porous polyolefin separators have good mechanical and thermal properties and effectively prevent thermal runaway caused by electrical short-circuits or rapid overcharging. However, they do not readily absorb the electrolyte solvents with high dielectric constants such as ethylene carbonate, propylene carbonate, and γ-butyrolactone due to their hydrophobic surface with low surface energy, and have poor ability in retaining the electrolyte solutions (Wang et al., 2000; Lee et al., 2005). In addition, the solvent leakage from the interfaces between electrodes or the opposite side of current collectors often causes the deterioration of life cycle of the rechargeable lithium batteries (Croce et al., 1998). To overcome these drawbacks of conventional polyolefin separators, much research has been undertaken to develop alternative separators that are compatible with polar liquid electrolytes and stable with the electrode materials (Michot et al., 2000; Huang & Wunder, 2001; Song et al., 2002; Saito et al., 2003).

A number of efforts have been made to achieve high-performance polyolefin separators by coating them with gel polymer electrolytes to improve the compatibility with various electrolyte solutions as well as the electrochemical properties of the lithium-ion polymer batteries (Abraham et al., 1995; Kim et al., 2001; Wang et al., 2002). Although these surface-modified polyolefin separators exhibit good mechanical and thermal properties as well as the degree of compatibility with the electrolyte solutions, they still have several disadvantages such as complex multi-step processes and relatively expensive modification of the surface of hydrophobic polyolefin separator with adequate hydrophilic monomers to increase the surface energy enough to absorb the electrolyte solutions. Among the numerous methods of the surface modification of polyolefin separators, the radiation process is one of the most promising methods due to the rapid formation of active sites for initiating the reaction through the polymer matrix and the uniformity of polymers over the entire specimens (Tsuneda et al., 1993). In addition, plasma process is a preferred and convenient technique when considering a large scale production or commercialization of the membrane. However, studies on the surface modification of polyolefin separators using the plasma technology have rarely been investigated to date.

In this chapter, we describe the fabrication of a novel modified polyethylene (PE) membrane by coating the plasma-induced acrylonitrile (PiAN) onto the surface of PE membrane using plasma technology in order to create high-performance separator membranes for practical applications in rechargeable lithium-ion polymer batteries. An acrylonitrile was chosen as a polymeric coating material for the surface of PE membranes because of its chemical stability and ability to be easily wetted by the electrolyte solution for use in the lithium-ion polymer batteries (Choe et al., 1997; Akashi et al., 1998). Attempts to coat the PiAN on the surface of a porous PE membrane and to fabricate the plasma-induced AN coated membrane (PiAN-PE) have not been previously investigated, and the study on the characterization of PiAN-PE membranes have not yet been reported in the literature. This is the first study of possible

realization of PiAN-PE membrane as a separator, and will help in preliminary evaluation and understanding of PiAN-PE membrane as a separator for the lithium-ion polymer battery. This study also suggests that PiAN-PE membrane via plasma treatment holds a great potential to be used as a high-performance cost-effective separator for lithium-ion polymer batteries.

2. Fabrication of separators for lithium-ion polymer battery

2.1 General features

The separator is a critical component in the lithium-ion polymer battery, and its primary function is to facilitate ionic transport between the electrodes as well as to prevent the electric contact of the electrodes. However, the presence of the separator in lithium-ion polymer battery induces electrical resistance and limited space inside the battery to satisfy the need for slimming and safety, which significantly influences the battery performance. Thus, the fabrication of high-performance separators plays an important role in controlling the overall performance of lithium-ion polymer battery, including high power or energy density, long cycle life, and excellent safety.

For many design options, the separator design requirements have been proposed by many researchers, and a number of factors influencing the battery performance must be considered in achieving high-performance separators for the battery applications. Among a wide variety of properties for the separators used in the lithium-ion battery, the following criteria should be qualified to fabricate the separators for lithium-based battery (Arora & Zhang, 2004): (a) electronic insulator, (b) minimal electric resistance, (c) dimensional stability, (d) mechanical strength enough to allow the assembly process, (e) chemical stability against degradation by electrolyte or electrode reactants, (f) effective prevention of the migration of particles or soluble species between the electrodes, (g) good wettability on electrolyte solution, and (h) uniform thickness and pore distribution. General requirements of the separators for lithium-ion batteries are summarized in Table 1.

Separator parameters	Parameter values	Standard
Thickness	< 25 μm	ASTM D5947-96
Electrical resistance	< 2 Ωcm^2	US 4,464,238
Pore size	< 1 μm	ASTM E128-99
Porosity	~ 40%	ASTM E128-99
Wettability	Completely wet in liquid electrolytes	
Chemical stability	Stable in the battery for long cycle life	
Tensile strength	> 1500 kg/cm^2	ASTM D882
Puncture strength	> 300 g/mil	ASTM D3763
Shrinkage	< 5%	ASTM D1204
Shutdown temperature	~130°C	

Table 1. Separator requirements for lithium-ion battery

Most of microporous polymer membranes currently used in the lithium-ion polymer battery is based on polyolefin resins, including polyethylene (PE), polypropylene (PP) and their blends or multilayer forms such as PE–PP and PP-PE-PP (Higuchi et al., 1995; Sogo, 1997; Hashimoto et al., 2000; Fisher & Wensley, 2002; Lee et al., 2004). Usually, the microporous polymer membrane as a separator for lithium-ion polymer battery can be fabricated by dry

and wet processes, including the extrusion step to make thin films and the orientation steps to impart porosity and increase mechanical strength (Bierenbaum et al., 1974; Kim & Lloyd, 1991). The separators made by dry process show a distinct slit-pore and straight microstructure, while those made by wet process exhibit interconnected spherical or elliptical pores (Zhang, 2007). The dry process for polymers with high crystallinity consists of the following steps (Yu & Dwiggins, 1997; Yu, 2000; Chandavasu et al., 2004; Yu, 2005): (a) extruding step (polyolefin resins are melt-extruded into a uniaxially oriented film), (b) annealing step (to improve the size and lamellar crystallites), and (c) stretching step (i.e., annealed films are deformed along the machine direction by three sequential processes of cold stretching to create the pore structure, hot stretching to increase the size of pores, and relaxation to reduce internal stresses within the films). Consequently, the porosity of microporous membranes depends on the morphology of films, annealing conditions and stretching ratios (Arora & Zhang, 2004; Zhang, 2007). The wet process for both crystalline and amorphous polymers is performed as follows (Kesting, 1985; Weighall, 1991; Yen et al., 1991; Chung et al., 1993; Kim et al., 1993): (a) mixing of hydrocarbon liquid and other additives with polyolefin resins and heating, (b) extrusion of the heated solution into a sheet, orientating the sheet uniaxially or biaxially, and (c) extraction of the liquid with a volatile solvent to form the microporous structure (Bierenbaum et al., 1974; Takita et al., 1991). For semi-crystalline polymers, a stretching step can be performed before/after the extraction step to achieve high porosity and a large pore size (Ihm et al., 2002).

However, commercially available polyolefin separators cannot satisfy the enhanced battery characteristics and stability accompanied by the need for sliming various devices required in the actual industrial field. Accordingly, the physical properties of polyolefin separator must be improved in order to be applied as a separator for high-performance and high-safety lithium-ion polymer battery. In addition, commercial polyolefin separators cannot be wet easily organic electrolyte solutions with high dielectric constant usually used in lithium battery, and have poor ability in conserving the electrolytes during the repeated cycling process. Further, they have a shortcoming since it causes a phenomenon of leaking organic electrolyte solutions between electrodes or separators, thereby lowering the cycle life performance of lithium-ion polymer battery. Future development of polymer membranes as separators for lithium-ion polymer batteries will be performed by balancing high performance of separators against their safety and manufacturing cost.

2.2 Plasma treatment techniques

Plasma treatment methods have been developed to modify polymer surfaces for enhanced adhesion, wettability, printability, dye-uptake, etc., and usually performed by modifying the surfaces on only several molecular levels, thus allowing the surface functionalization of polymers without sacrificing their appearance and bulk properties (Liston et al., 1994). Plasma is a chemical process and its chemistry determines on polymers. Among several plasma processes, cold gas plasma treatments are used in processing of them. Cold gas plasma generally has very low temperature (300~600 K) and particle density of 10^{10}~10^{12} no./cm^3, suitable for modifying polymer materials (Kapla & Rose, 2006). Exposing gases to sufficient electromagnetic power dissociate them, and create chemically reactive gases that modify the exposed surfaces. At the atomic level, plasma consists of ions, electrons, and various neutral species at different energy levels. One of the excited species is free radicals, which can directly react with the surface of polymers, leading to remarkable modifications

to their chemical structures and properties. The generated ions and electrons collide with the atoms of surfaces, and transfer energy to form more radicals, ions, and atoms. The general reactions induced by means of cold gas plasma, depending on the substrate, gas chemistry, reactor design, and operating parameter, are as follows (Liston et al., 1994; Shishoo, 2007): (a) cleaning to remove organic contamination from the surfaces, (b) ablation or etching of materials form the surface of polymer to remove a weak boundary layer and increase the surface roughness and area, (c) crosslinking of near-surface molecules, to cohesively strengthen the surface layers, (d) activation by creating reactive sites, grafting of chemical moieties and functional groups to modify the chemical structures of polymer surfaces, and (e) polymerized deposition of thin polymeric films on the surface. Various gases used for plasma reactions are presented in Table 2. As oxygen gas plasma breaks the C-C bonds of polymers, volatile monomers or oligomers ablate at shorter molecules, and they are cleaned with the exhaust. After cleaning, the plasma begins ablating the top layer of polymers. Amorphous and crystalline regions will be removed at different rates, producing the surface topology with a view to increasing the mechanical adhesion. On the contrary, noble gases such as argon and helium generate free radicals on the surface and they react with adjoining radicals of molecules to form crosslinks. This process increases the strength, temperature resistance, and solvent resistance of the surface of polymers. Unlike ablation and crosslinking, certain gas or mixture of gas generate free radicals on the surface and then react with radicals of functional molecules in the plasma by covalent bonding. In particular, oxygen and tetrafluoromethane gas plasma do oxidative reaction and form polar groups such as carboxyl, hydroxyl, and hydroperoxyl on the molecules. This oxidation increases the surface energy, and enhances the hydrophilicity and wettability of polymers. If use with substances such as fluoro-monomers and acrylic-monomers, the polymerization will take place. This process provides permanent coating of thin films on the surface of polymers. In general, fluoro-monomer gas plasma provides a low surface energy and hydrophobic surfaces, while acrylic-monomer gas plasma induces permanent hydrophilicity and wettability without mixing of other gases.

Plasma reactions	Gas
Cleaning	Oxygen
Ablation/Etching	Argon, Helium, Oxygen
Crosslinking	Oxygen-free noble gases such as argon and helium
Activation	Ammonia, Argon, Helium, Methane, Nitrogen, Tetrafluoromethane
Polymerization	Fluoro-monomers (Hexafluoroethylene, Perfluoroallylbenzene, Pentafluorostyrene, etc.) Acrylic-monomers (Acrylic acid, Acrylonitrile, Alkyl acrylates, etc.)

Table 2. Various gases used for plasma reactions

Recently, a number of efforts have been made up to develop the performance of separators by means of plasma treatment technology, because it is very efficient techniques to modify the surface properties of polymer membranes without producing impurities or sacrificing their properties. Kubota treated PP separator film with nitrogen gas plasma to create polymeric radicals for utilizing the graft polymerization-initiating sites, followed by immersion with acrylic monomer solution and polymerization at 65^{o}C, and the resultant separators showed the increased ionic conductivity (Kubota, 1993). For nikel-metal secondary battery, Tsukiashi et al. modified PP non-woven fabric separators by means of

the technique of gas plasma treatment using several gases such as oxygen, nitrogen, and argon to increase their surface hydrophilicity and they reported that the modified PP non-woven fabric separators with the contact angle below 100° showed the increased capacity retention (Tsukiashi et al., 2003). Ciszewski et al. reported the results of the plasma-induced graft polymerization of acrylic acid under UV irradiation using microporous PP membranes for nickel–cadmium (Ni-Cd) battery. (Ciszewski et al., 2006; Ciszewski et al., 2007). They modified PP membranes by argon plasma treatment to create grafting sites, followed UV irradiation to covalently-bond acrylic acid to the surface of PP, and suggested that hydrophobic surface of PP membrane changed into hydrophilic via this technique and the resulting PP membrane as a separator for Ni–Cd cells showed good mechanical properties and very low electrolytic area resistance. Choi et al., reported that the electrospun poly(vinylidene fluoride) nanofiber web treated with ethylene plasma could provide the web surface with low melting PE layer, in which polymerized-PE layer could act as a shutter by melting at elevated temperature, thus contributing to the safety of battery (Choi et al., 2004). More recently, we reported the fabrication of plasma-modified PE membrane as a separator for lithium-ion polymer battery, in which the surface of microporous PE membranes was modified with acrylonitrile using the plasma-induced coating process and the lithium-ion polymer battery cells fabricated with the modified PE separator showed the enhanced cycling life and rate performance (Kim et al., 2009).

3. Plasma-modified polyethylene separator membrane

Urethane acrylate (UA) and hexyl acrylate (HA) were supplied by Samsung Cheil Industry, Korea, and were used without further purification. A 2,2-azobis(2,4-dimethylvaleonitrile) (V-65®, Wako Pure Chem., Japan) was used as an initiator. The electrolyte solution of 1.3 M lithium hexafluorophosphate ($LiPF_6$) dissolved in the mixture of ethylene carbonate (EC), ethyl methyl carbonate (EMC), and dimethyl carbonate (DEC) (EC:EMC:DEC=3:2:5, by volume, battery grade) was supplied by Samsung Cheil Industry, Korea. An acrylonitrile (AN, degree of purity >98%, Aldrich) was used as received without further purification. The gel polymer electrolyte was prepared as follows: UA/HA (3:1, by weight) in the presence of an initiator were dissolved in the above electrolyte solution by stirring at room temperature to achieve better homogenization, and they were polymerized at 75°C for 4 h to produce the cross-linked gel polymer electrolytes by thermal curing. All procedures were performed in a glove box filled with argon gas.

The system consists of the reactor equipped with the inner electrodes to which an alternating voltage was applied at a frequency of 13.56 MHz, an RF power supply with an impedance matching network, and a vacuum pump. Commercial porous PE membranes (Asahi Chem., Japan) were dipped in AN solution for 5 min, and they were moved into the reactor. Subsequently, the dipped PE membranes were placed between the electrodes in the reactor where the plasma-induced coating was initiated by the plasma generation. Prior to starting up the plasma treatment, plasma reactor was evacuated, and argon gas was introduced into the reactor at a flow rate of 400 sccm using unit mass flow controller. Then, the vacuum pressure of the plasma reactor was maintained at a constant value of 10^{-3} Torr. The electrical power of the plasma was supplied by an RF power operating at 300W and the treatment time was 10 min.

The cathode was prepared by coating the slurry consisting of 96% lithium cobalt oxide ($LiCoO_2$) with 2% poly(vinylidene fluoride) (PVDF) as a binder and 2% acetylene black as a conducting agent in a *N*-methyl pyrrolidone (NMP) solvent onto aluminum foils. The graphite anode was prepared by coating the slurry of 94% graphite with 6% PVDF onto copper foils. The lithium-ion polymer cells were assembled in the form of the aluminum pouch by sandwiching PE or PiAN-PE membrane between $LiCoO_2$ cathode and graphite anode. After assembling the cell, polymer precursor solution was injected into the aluminum pouch, which then was vacuum-sealed. Polymer precursor in the cell was thermally cured in the heating oven at 75°C for 4 h to form cross-linked gel polymer electrolytes. The prepared cells were cycled once at 0.2 C rate to improve the wetting of gel polymer electrolytes and to form stable solid electrolyte interphase (SEI) layers on the electrode surface.

XPS spectra were obtained on a VG ESCALAB 220-I system using Mg Kα X-radiation as the excitation source with a pass energy of 1253.6 eV. XPS analysis was performed under high vacuum conditions (10^{-9} Torr). All binding energies were referenced to the C_{1s} neutral carbon peak at 284.6 eV. The membrane surfaces were characterized by contact angle measurements. Water contact angle was determined by means of the sessile drop method, and the water droplet was limited to about 0.5 μl to prevent gravitational distortion of its spherical profile. The surface energies of PE and PiAN-PE membranes were calculated by measuring the contact angle of two testing liquids: water and diiodomethane on the surface of the membranes at room temperature using a contact anglemeter G-1 model (ERMA Inc.). The morphology of PE and PiAN-PE membranes were observed using a JEOL JSM-6340F SEM. The peel strength was measured at room temperature by a T-peel test using an Instron 4465 testing machine employing the crosshead speed of 10 mm/min, according to the procedures in the ASTM D1876 standard. The membranes, immersed in the electrolyte solutions consisting of 1.3 M $LiPF_6$ and EC:EMC:DEC (3:2:5) mixture, were sandwiched between two stainless-steel electrodes. The ionic conductivity of the membranes was obtained from the bulk resistance, which measured by AC complex impedance analysis using a Solartron 1255 frequency response analyzer over the frequency range of 100 Hz to 1 MHz. The charge and discharge cycling tests of the lithium-ion polymer cell were conducted in the voltage range of 3.0~4.2 V at a constant current density at room temperature using a TOSCAT-300U instrument (Toyo System Co.)

4. Effect of plasma modification on polyethylene membrane

4.1 Surface properties

XPS spectra of PE and PiAN-PE membranes are shown in Figure 1. XPS analysis was performed to clarify the surface elemental composition for the membranes. XPS spectrum of PE membrane exhibited the presence of only carbon as observed at 284.6 eV, corresponding to C_{1s} core level. However, PiAN-PE membrane exhibited intense and narrow peak at 532.5 eV and very weak intensity peak centered at 400.5 eV, corresponding to O_{1s} and N_{1s} core levels, respectively, as well as C_{1s} core level for PE membrane, as shown in Figure 1(b). As shown in Figure 1(c), XPS spectra of C_{1s} core level for PiAN-PE membrane can be decomposed into five contributions appearing at 284.6, 285.5, 286.2, 287.6, and 289.1 eV. These observed peaks were assigned to C–C/C–H, C–O, C–N, C=O, and –COO groups formed on the surface of PiAN-PE membrane originating from PE membrane and AN. The –

CH and $-CH_2$ (of pristine PE), oxidized (–C=O, –COO, –COC–), and –C=C– groups were reported to present in Ar plasma treated high density polyethylene (Svorcik et al., 2006). The percentage contributions of the C_{1s} components of PiAN-PE membrane are shown in Table 3. After the plasma-induced coating process, the contribution of the C–N groups in the XPS spectra of C_{1s} core level for PiAN-PE membrane was 7.55%, which was attributed to the presence of PiAN in the membrane. This result demonstrates that PiAN was effectively induced onto the surface of PE membrane via plasma treatment.

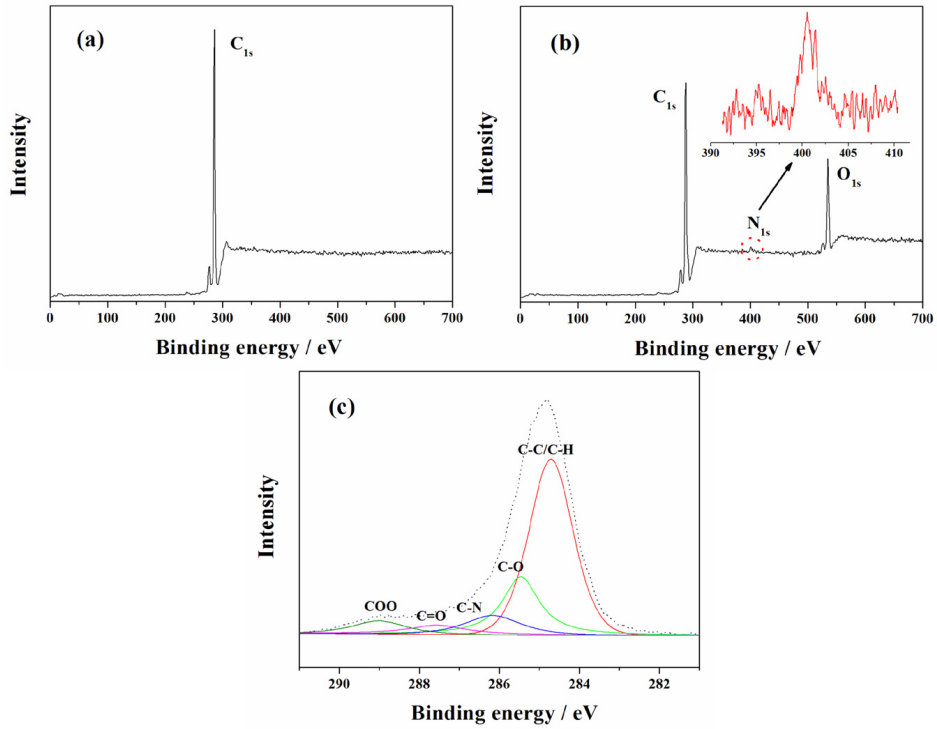

Fig. 1. XPS spectra of (a) PE and (b) PiAN-PE membranes and high resolution spectra of C_{1S} core level for PiAN-PE membranes. The inset of Fig. 1(b) shows N_{1S} core level spectra of PiAN-PE membranes

Materials	Functional group (%)				
	C-C/C-H	C-O	C-N	C=O	C-O-O
PE membrane	98.37	1.16	-	0.26	0.21
PiAN-PE membrane	63.77	17.54	7.55	5.00	6.14

Table 3. XPS analysis of PE and PiAN-PE membranes

The contact angle measurements of PE and PiAN-PE membranes were conducted to clarify the effect of PiAN on the surface property of the membrane. For the lithium-ion polymer cell

assembly, the wettability of the separator used in the non-aqueous electrolytes plays a critical role in the cell performance because the separator with good wettability can effectively retain the electrolyte solutions and facilitates the electrolytes to diffuse well into the cell assembly (Arora & Zhang, 2004; Zhang, 2007). As shown in Figure 2, the contact angle of PiAN-PE membranes significantly decreased, indicating significant change of the surface property of PE membranes. The contact angle of PiAN-PE membrane was much smaller than that of PE membrane, implying that PiAN-PE membrane has better wettability as compared to PE membrane. This result demonstrates that the surface energy of PiAN-PE membrane increased by the presence of PiAN on the surface of the membrane effectively induced via plasma treatment. Therefore, it is expected that the presence of PiAN on the surface of the membranes makes it possible for them to have high surface energy to be wetted more sufficiently in the electrolyte solution as compared to PE membrane.

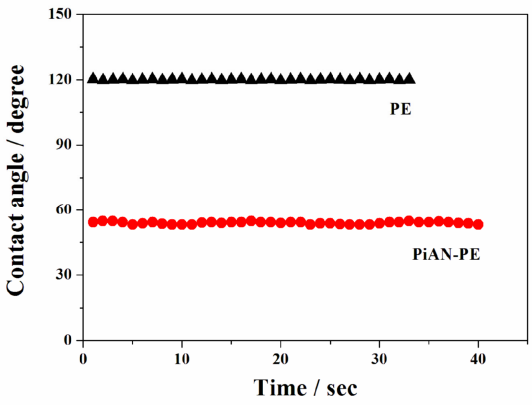

Fig. 2. Contact angles of PE and PiAN-PE membranes

The surface energy and its polar component of the PE and the PiAN-PE membranes can be estimated from the Qwens–Wendt equation modified by Fowkes and Kinloch (Owens & Wendt, 1969; Konloch, 1987; Novak & Chodak, 2006; Novak et al., 2008):

$$(1+\cos\theta)\gamma_{LV} = 2\sqrt{\left(\gamma_{LV}^{d}\cdot\gamma_{S}^{d}\right)} + 2\sqrt{\left(\gamma_{LV}^{p}\cdot\gamma_{S}^{p}\right)} \quad (1)$$

$$\gamma_S = \gamma_S^d + \gamma_S^p \quad (2)$$

where θ is the observed contact angle; γ_{LV} and γ_S are the surface free energy of testing liquid and a polymer, respectively, and the superscript d and p refer to the dispersive and polar components of surface energy, respectively. The preferred values of the surface energy and its components for two testing liquids used are as follows: γ_L = 72.8, $\gamma_L{}^d$ = 21.8, and $\gamma_L{}^p$ = 51.0 mJ/m² for water and γ_L = 50.8, $\gamma_L{}^d$ = 50.4, and $\gamma_L{}^p$ = 0.4 mJ/m² for diiodomethane (Wu, 1982). The results for the surface energy of PE and PiAN-PE membranes are presented in Table 4. The PiAN-PE membrane exhibited higher values of γ_S, $\gamma_S{}^p$, and X_p than those of PE membrane. This result indicated that the presence of the PiAN in the membrane effectively

induced via plasma-induced coating process increased the fraction of polar component in the surface energy of PiAN-PE membrane, resulting in the enhanced polarity and higher surface energy of PiAN-PE membrane. It should be noted that the increased polar component in the surface energy of PiAN-PE membrane can favor the enhancement of the interfacial adhesion between the membrane and the electrodes, thus contributing to the improvement in the cycle performance of the lithium-ion polymer cell assembly.

Materials	γ_s	γ_s^d	γ_s^p	X_p [a]
PE membrane	30.3	28.9	1.4	0.05
PiAN-PE membrane	56.6	40.8	15.8	0.28

Table 4. The surface energy and polarity of PE and PiAN-PE membranes [[a] The polarity, $X_p = \gamma_p/\gamma$]

4.2 Morphology

SEM images of the surfaces for PE and PiAN-PE membranes are shown in Figure 3. The PE membranes had highly porous structures with uniform pore sizes of approximately 200 nm. According to the supplier's specification, PE membranes exhibit a pore structure with the thickness of 23 μm and the porosity of ~40%. After the plasma-induced coating process, PiAN-PE membranes exhibited rough surfaces and expanded pore structure relative to the PE membranes. The surfaces of PiAN-PE membrane appeared to be porous structures with some dense or coated layers. This result suggests that some pores or surfaces for PiAN-PE membranes may be partially covered by the PiAN. In addition, the PiAN covered in both top and bottom sides of the surface of PiAN-PE membrane can be also observed, implying that the PiAN were introduced simultaneously into both sides of the surface of PiAN-PE membrane via this plasma-induced coating process. In general, the presence of the pores on the membrane can lead to the efficient uptake of the electrolyte solution. Although both membranes were easily wetted in a few seconds in contact with the electrolyte solution, PiAN-PE membranes exhibited better wettability than PE membrane. This result was in good agreement with much lower contact angle and higher surface energy of PiAN-PE membranes as compared to the PE membranes.

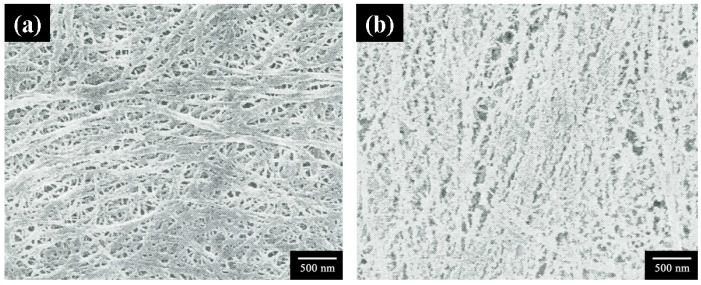

Fig. 3. SEM micrographs of the surfaces for (a) PE and (b) PiAN-PE membranes.

5. Plasma-modified polyethylene separator for lithium-ion polymer battery

5.1 Ionic conductivity and adhesion

For the liquid electrolyte-based system, the ionic conduction may be mainly provided by the electrolyte solution, and the variation of the ionic conductivity is related to the polymer morphology and microstructure of the membrane for the retention of the electrolyte solution (Linden & Reddy, 2002). The ionic conductivities of PE and PiAN-PE membrane at room temperature were estimated to be 0.8×10^{-3} and 1.4×10^{-3} S/cm, respectively. In general, non-polar polyethylene separators exhibited poor wettability and electrolyte retention with the electrolyte solutions containing polar solvents, due to their inherent hydrophobic properties. For PE membrane, it was difficult to be completely wetted by organic solvents with high dielectric constant because of its hydrophobic surface with low surface energy, leading to lower ionic conductivity. However, PiAN-PE membrane exhibited better electrolyte retention as compared to PE membrane due to its good compatibility between the PiAN and the carbonate-based electrolyte solution, resulting from the fact that the electrolyte solution was well retained in the porous membrane by polymer–solvent interactions (Kim, et al., 2002) with the presence of the PiAN induced onto the surface of PiAN-PE membrane. Therefore, PiAN-PE membrane exhibited high ionic conductivity due to the improved wettability and electrolyte retention, resulting from the presence of the PiAN induced onto the surface of PiAN-PE membrane by the plasma treatment.

The peel testing of PE and PiAN-PE membranes was performed to clarify the effect of the PiAN induced onto the surface of PE membrane via plasma-induced coating process on the interfacial adhesion between the electrodes and the membrane. As shown in Table 5, the average peel strength of the test cell based on PiAN-PE membrane was increased to 22.6 N/m by up to 18% compared to the reference cell with PE membrane. This result suggested that the adhesion between the separator and the electrodes was improved by the PiAN effectively induced onto the surface of the membrane via plasma-induced coating process

Materials	Average load (N)	Peel strength (N/m)
PE membrane	0.44	19.1
PiAN-PE membrane	0.52	22.6

Table 5. The peel testing of PE and PiAN-PE membranes

5.2 Cycle performance of lithium-ion polymer battery

The lithium-ion polymer cells fabricated with PE or PiAN-PE membranes were subjected to charge–discharge tests after preconditioning with cut-off voltages of 4.2 V for the upper limit and 3.0 V for the lower limit at 1 C rate. The charge–discharge profiles of the fabricated lithium-ion polymer cells with cycle number are shown in Figure 4. It can be seen that the voltage drop in passing from charge to discharge was small, indicating the lower resistance of the lithium-ion polymer cell. As cycle number increased, the voltage and capacity decreased, which was attributed to the high polarization resulting from the increased internal resistance of the cell and the decrease in the diffusivity of the lithium ion in the electrode (Avora & Zhang, 2004; Zhang, 2007). As shown in Figure 4, the discharge capacity of the lithium-ion polymer cell fabricated with PiAN-PE membrane was higher than that of the cell with PE membrane. The plasma-induced PiAN coating process can enhance the interfacial adhesion between the electrodes and the separator, which were interfacial

resistance of the cell, resulting in higher cycle performance of the lithium-ion polymer cell fabricated with PiAN-PE membrane.

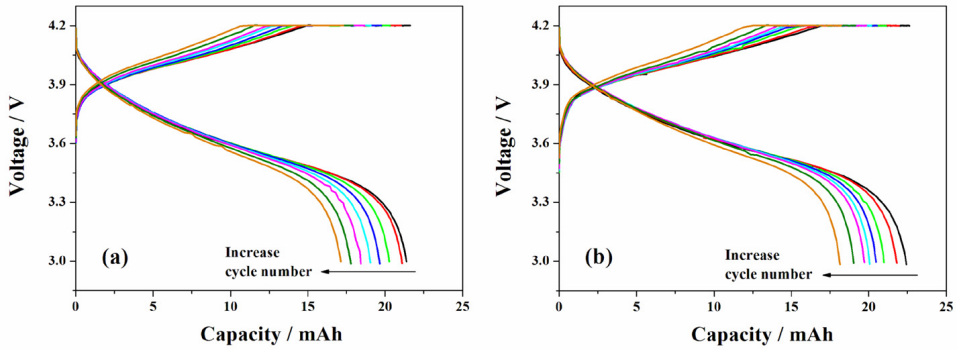

Fig. 4. Charge-discharge profiles for the lithium-ion polymer cells fabricated with (a) PE and (b) PiAN-PE membranes with increasing cycle number.

The variations of the coulombic efficiency of the lithium-ion polymer cell with cycle number are shown in Figure 5(a). In general, the coulombic efficiency can be defined as the ratio of the discharge capacity to charge capacity. The relatively low coulombic efficiency of both membranes during the initial cycling was attributed to the formation of SEI layers on the surface of the graphite electrode (Morzilli et al., 1987; Aurbach et al., 1994; Zhang et al., 2001), providing the good stability to the graphite anode toward the electrolyte reduction during lithium intercalation–deintercalation. The coulombic efficiency of the cell tended to increase with increasing cycle number, and gradually approached to unit value (>99.5%). The discharge capacities of the lithium-ion polymer cells fabricated with PE or PiAN-PE membranes with cycle number are shown in Figure 5(b). The discharge capacity of the cell was slowly decreased with increasing cycle number. The decrease in the discharge capacity may be attributed to the deterioration of the interfacial contact of the electrodes and the physical changes in the active materials for the electrodes (Avora & Zhang, 2004; Zhang, 2007), leading to the gradual increase in the internal resistance of the cell during the repeated charge–discharge cycling. After 96th cycles, the lithium-ion polymer cell fabricated with PiAN-PE membrane retained 80.3% of the initial discharge capacity, while the cell with PE membrane showed 76.4% of that. Higher discharge capacity of the lithium-ion polymer cell fabricated with PiAN-PE membrane may be attributed to the enhanced wettability and the reduced interfacial resistance (Kim et al., 2004). This result suggests that the PiAN effectively induced on the surface of the membranes play a critical role in determining the cycle performance of the lithium-ion polymer cell and that stable cycle performance can be obtained by modifying the surface of PE membrane with the plasma-induced coating process.

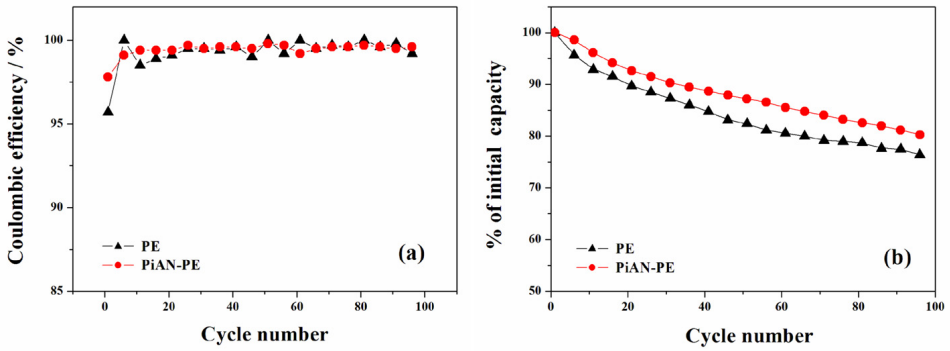

Fig. 5. (a) Coulombic efficiency and (b) discharge capacity of the lithium-ion polymer cells fabricated with PE or PiAN-PE membrane as a function of cycle number

The rate capabilities of the lithium-ion polymer cells fabricated with PE or PiAN-PE membranes with cycle number are shown in Figure 6. The lithium-ion polymer cells fabricated with PE or PiAN-PE membranes exhibited the capacity retentions of 90.3 and 93.1%, respectively, at 0.5 C rate, and then decreased clearly with increasing the current rate. The lithium-ion polymer cells fabricated with PiAN-PE membranes exhibited higher capacity retention than in the case of PE membrane. As compared to PE membrane, better rate capability of the cell fabricated with PiAN-PE membrane may be attributed to the enhanced interfacial adhesion between the electrodes and the separator as well as better wettability and the electrolyte retention. This result demonstrates that good cycle performance of the lithium-ion polymer cells can be obtained by using a novel modified PiAN-PE membrane with simple plasma treatment, suggesting that PiAN-PE membrane is expected to be a promising polymer membrane as a high-performance and cost-effective separator for rechargeable lithium-ion polymer batteries.

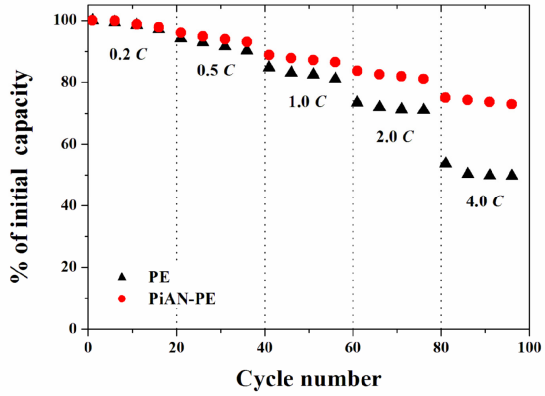

Fig. 6. Rate capability of the lithium-ion polymer cells fabricated with PE or PiAN-PE membrane as a function of cycle number

6. Summary

The separator is a critical component in the lithium-ion polymer batteries, and its primary function is to facilitate ionic transport between the electrodes as well as to prevent the electric contact of the electrodes. This chapter describes the fabrication of a novel modified polyethylene membrane via plasma-induced coating process to create high performance and cost-effective separator membranes for practical applications in rechargeable lithium-ion polymer battery. The enhanced interfacial adhesion and cycle performance of the lithium-ion polymer cell fabricated with modified polyethylene membrane by plasma-induced coating process were observed. The surface modification of polyethylene membrane by the plasma-induced coating process played a critical role in determining the performance of the resultant lithium-ion polymer cell assembly. The plasma-modified polyethylene membrane exhibited the increased ionic conductivity, the good wettability, and the enhanced interfacial adhesion between the electrodes and the separators. Consequently, the lithium-ion polymer cell fabricated with the plasma-modified polyethylene membrane exhibited better cycle performance as compared to the unmodified polyethylene membrane. This chapter suggests that the performance of the lithium-ion polymer battery can be greatly enhanced by the plasma modification of the commercial separator with proper materials for targeted application. Future development of microporous polymer membranes as separators for lithium-ion polymer batteries will be performed by balancing high performance of separators against their safety and manufacturing cost.

7. References

Abraham, K. M.; Alamgir, M. & Hoffman, D. K. (1995). Polymer Electrolytes Reinforced by Celgard® Membranes. *J. Electrochem. Soc.*, 142, 683-687.

Akashi, H.; Tanaka, K. & Sekai, K. (1998). An Ionic Conductivity and Spectroscopic Study of Ionic Transport Mechanism in Fire-Retardant Polyacrylonitrile-Based Gel Electrolytes for Li Polymer Batteries. *J. Electrochem. Soc.*, 145, 881-887.

Arora, P. & Zhang, Z. (2004). Battery Separators. *Chem. Rev.*, 104, 4419-4462.

Aurbach, D.; Weissman, I.; Zaban, A. & Chusid, O. (1994). Correlation Between Surface Chemistry, Morphology, Cycling Efficiency and Interfacial Properties of Li Electrodes in Solutions Containing Different Li Salts. *Electrochim. Acta*, 39, 51-71.

Besenhard, J. O. (1999). *Handbook of Battery Materials*, Wiley–VCH, Weinheim

Bierenbaum, H. S.; Isaacson, R. B.; Druin, M. L. & Plovan, S. G. (1974). Microporous Polymeric Films. *Ind. Eng. Chem. Prod. Res. Dev.*, 13, 2-9.

Chandavasu, C.; Xanthos, M.; Sirkar, K. K. & Gogos, C. (2004). Preparation of Microporous Films from, Immiscible Blends via Melt Processing and Stretching. US Patent 6,824,680.

Choi, S. S.; Lee, Y. S.; Joo, C. W.; Lee, S. G.; Park, J. K. & Han, K. S. (2004). Electrospun PVDF Nanofiber Web As Polymer Electrolyte or Separator. *Electrochim. Acta*, 50, 339-343.

Choe, H. S.; Carroll, B. G.; Pasquariello, D. M. & Abraham, K. M. (1997). Characterization of Some Polyacrylonitrile-Based Electrolytes. *Chem. Mater.*, 9, 369-379.

Chung, T. S.; Foley, P.; Kafchinski, E. R. (1993). Development of Poly(ethylene tetrafluoroethylene) Microporous Film for Advanced Batteries. *J. Mater. Sci.-Mater. Electron.*, 4, 259-266.

Ciszewski, A.; Gancarz, I.; Kunicki, J. & Marek, B. (2006). Plasma-modified Polypropylene Membranes As Separators in High Power Alkaline Batteries. *Surf. Coat. Technol.*, 201, 3676-3684.

Ciszewski, A.; Kunicki, J. & Gancarz, I. (2007). Usefulness of Microporous Hydrophobic Polypropylene Membranes After plasma-induced Graft Polymerization of Acrylic Acid for High Power Nickel-Cadmium Batteries. *Electrochim. Acta*, 52, 5207-5212.

Croce, F.; Appetecchi, G. B.; L. Persi, L. & Scrosati, B. (1998). Nanocomposite Polymer Electrolytes for Lithium Batteries. *Nature*, 394, 456-458.

Fisher, H. M. & Wensley, C. G. (2002). Polypropylene Microporous Membrane for Battery Separator. US Patent 6,368,742.

Hashimoto, A.; Yagi, K. & Mantoku, H. (2000). Porous Film of High Molecular Weight Polyolefin and Process for Producing Same. US Patent 6,048,607.

Higuchi, H.; Matsushita, K.; Ezoe, M. & Shinomura, T. (1995). Porous Film, Process for Producing the Same and Use of the Same. US Patent 5,385,777.

Huang, H. & Wunder, S. L. (2001). Ionic Conductivity of Microporous PDVF-HFP/PS Polymer Blends. *J. Electrochem. Soc.*, 148, A279-A283.

Ihm, D. W.; Noh, J. G. & Kim, J. Y. (2002). Effect of Polymer Blending and Drawing Conditions on Properties of Polyethylene Separator Prepared for Li-ion Secondary Battery. *J. Power Sources*, 109, 388-393.

Kaplan, S. L. & Rose, P. W. (2006). Plasma Surface Treatment, In: *Coatings Technology Handbook*, Tracton, A. A., (Ed.), CRC Press.

Kesting, R. E. (1985). *Synthetic Polymeric Membranes*, John Wiley & Sons Inc., New York.

Kim, D. W.; Ko, J. M.; Chun, J. H.; Kim, S. H. & Park, J. K. (2001). Electrochemical Performances of Lithium-Ion Cells Prepared with Polyethylene oxide-Coated Separators. *Electrochem. Commun.*, 3, 535-538.

Kim, D. W.; Noh, K. A.; Min, H. S.; Kang, D. W. & Sun, Y. K. (2002). Porous Polyacrylonitrile Membrane for Lithium-Ion Cells. *Electrochem. Solid-State Lett.*, 5, A63-A66.

Kim, J. J.; Kim, S. S.; Hwang, J. R. & Suh, S. B. (1993). Process for the Preparation of Porous Polyolefin Separation Membranes via Thermally-Induced Phase Separation. US Patent 5,250,240.

Kim, J. Y.; Kim, S. K.; Lee, S. J.; Lee, S. Y.; Lee, H. M. & Ahn, S. (2004). Preparation of Microporous Gel Polymer for Lithium Ion Polymer Battery. *Electrochim. Acta*, 50, 363-366.

Kim, J. Y.; Lee, Y. & Lim, D. Y. (2009). Plasma-modified Polyethylene Membrane As a Separator For Lithium-Ion Polymer Battery. *Electrochim. Acta*, 54, 3714-3719.

Kim, S. S. & Lloyd, D. R. (1991). Microporous Membrane Formation via Thermally-Induced Phase Separation. III. Effect of Thermodynamic Interactions on the Structure of Isotactic Polypropylene Membranes. *J. Membr. Sci.*, 64, 13-29.

Konloch, A. J. (1987). *Adhesion and Adhesives: Science and Technology*, Springer

Kubota, T. (1993). Secondary Battery with Graft-polymerized Separator. US Patent 5,270,137.

Lee, Y. M.; Kim, J. W.; Choi, N. S.; Lee, J. A.; Seol, W. H. & Park, J. K. (2005). Novel Separator Based on PVdF and PE Non-woven Matrix for Rechargeable Lithium Batteries. *J. Power Sources*, 139, 235-241.

Lee, S. Y.; Ahn, B. I.; Im, S. G.; Park, S. Y.; Song, H. S. & Kyung, Y. J. (2004). High Crystalline Polypropylene Microporous Membrane, Multi-Component Microporous Membrane and Methods for Preparing the Same. US Patent 6,830,849.

Linden, D. & Reddy, T. B. (2002). *Handbook of Batteries*, McGraw-Hill, New York

Liston, E. M.; Martinu, L. & Werheimer, M. R. (1994). Plasma Surface Modification of Polymers for Improved Adhesion: A Critical Review, In: *Plasma Surface Modification of Polymers: Relevance to Adhesion*, Strobel, M.; Lyons, C. S. & Mittal, K. L., (Eds.), VSP, Netherlands.

Michot, T.; Nishimoto, A. & Watanabe, M. (2000). Electrochemical Properties of Polymer Gel Electrolytes Based on Poly(vinylidene fluoride) Copolymer and Homopolymer. *Electrochim. Acta*, 45, 1347-1360.

Morzilli, S.; Bonini, F. & Scrosati, B. (1987). Characteristics of the Lithium Electrode in Organic and Polymeric Electrolytes. *Electrochim. Acta*, 32, 961-964

Novak, I.; Pollak, V. & Chodak, I. (2006). Study of Surface Properties of Polyolefins Modified by Corona Discharge Plasma. *Plasma Process. Polym.*, 3, 355-364.

Novak, I.; Elyashevich, G. K.; Chodak, I.; Olifirenko, A. S.; Steviar, M.; Spirkova, M.; Saprykina, N.; Vlasova, E. & Kleinova, A. (2008). Polymer Matrix of Polyethylene Porous Films Functionalized by Electrical Discharge Plasma. *Eur. Polym. J.*, 44, 2702-2707.

Owens, D. K. & Wendt, R. C. (1969). Estimation of the Surface Free Energy of Polymers. *J. Appl. Polym. Sci.*, 13, 1741-1747.

Saito, Y.; Stephan, A. M. & Kataoka, H. (2003). Ion Conduction Mechanisms of Lithium Gel Polymer Electrolytes Investigated by the Conductivity and Diffusion Coefficient. *Solid State Ionics*, 160, 149-153.

Scrosati, B. (1993). *Applications of Electroactive Polymer*, Chapman & Hall, London

Shishoo, R. (2007). *Plasma Technologies for Textiles*, Woodhead Publishing Limited, England.

Sogo, H. (1997). Separator for a Battery Using an Organic Electrolytic Solution and Method for Preparing the Same. US Patent 5,641,565.

Song, J. Y.; Cheng, C. L.; Wang, Y. Y. & Wan, C. C. (2002). Microstructure of Poly(vinylidene fluoride)-Based Polymer Electrolyte and Its Effect on Transport Properties. *J. Electrochem. Soc.*, 149, A1230-A1236.

Svorcik, V.; Kolarova, K.; Slepicka, P.; Mackova, A.; Novotna, M. & Hnatowicz, V. (2006). Modification of Surface Properties of High and Low Density Polyethylene by Ar Plasma Discharge. *Polym. Degrad. Stab.*, 91, 1219-1225.

Takita, K.; Kono, K.; Takashima, T. & Okamoto, K. (1991). Microporous Polyolefine Membrane and Method of Producing Same. US Patent, 5,051,183.

Tsuneda, S.; Saito, K.; Furusaki, S.; Sugo, T. & Makuuchi, K. (1993). Simple Introduction of Sulfonic Acid Group onto Polyethylene by Radiation-Induced Cografting of Sodium Styrenesulfonate with Hydrophillic Monomers. *Ind. Eng. Chem. Res.*, 32, 1464-1470.

Tsukiashi, M.; Teraoka, H.; Hata, K. & Tajima, M. (2003). Battery Separator and Manufacturing Method Thereof, and Alkali Secondary Battery Having the Separator Incorporated Therein. US Patent 6,723,809.

Wang, H. P.; Huang, H. & Wunder, S. L. (2000). Novel Microporous Poly(vinylidene Fluoride) Blend Electrolytes for Lithium-Ion Batteries. *J. Electrochem. Soc.*, 147, 2853-2861.

Wang, Y.; Travas-Sejdic, J. & Steiner, R. (2002). Polymer Gel Electrolyte Supported with Microporous Polyolefin Membranes for Lithium Ion Polymer Battery. *Solid State Ionics*, 148, 443-449.

Weighall, M. J. (1991). Recent Advances in Polyethylene Separator Technology. *J. Power Sources*, 34, 257-268.

Wu, S. (1982). *Polymer Interface and Adhesion*, Marcel Dekker, New York

Yen, Y. L.; Lopatin, G.; Malarkey, H. & Soane, D. (1991). Process for Producing Fluorocarbon Membranes and Membrane Product. US Patent 5,032,274.

Yu, W. C. & Dwiggins, C. F. (1997). Methods of Making Cross-Ply Microporous Membrane Battery Separator, and the Battery Separators Made Thereby. US Patent 5,667,911.

Yu, W. C. (2005). Continuous Methods of Making Microporous Battery Separators. US Patent 6,878,226.

Yu, T. H. (2000). Trilayer Battery Separator. US Patent 6,080,507.

Zhang, S. S.; Ding, M. S.; Xu, K.; Allen, J. & Jow, T. R. (2001). Understanding of Solid Electrolyte Interface Film Formation on Graphite Electrodes. *Electrochem. Solid-State Lett.*, 4, A206-A208.

Zhang, S. S. (2007). A Review on the Separators of Liquid Electrolyte Li-Ion Batteries. *J. Power Sources*, 164, 351-364.

4

A novel all-solid-state thin-film-type lithium-ion battery with in-situ prepared electrode active materials

Yasutoshi Iriyama
Shizuoka University
Japan

1. Introduction

All-solid-state thin-film rechargeable lithium batteries have received much attention as a power source for micro devices. Especially, in recent years, thin-film batteries using lithium phosphorus oxynitride glass electrolyte (LiPON) discovered by Wang and co-workers (Wang et al., 1996) have been extensively investigated. In the fabrication process of these film batteries, thin films of electrodes, solid electrolyte, and current collectors are sequentially piled-up on a substrate using different kinds of vapor deposition techniques such as pulsed laser deposition, r.f. magnetron sputtering, and vacuum evaporation.

For the practical application of thin-film batteries, the fabrication process is desirable to be simplified as much as possible. One of the effective methods to overcome the above problem will be the use of ''*in-situ* formed'' material in the battery system. Using this in situ formed material, fabrication of at least one of the material in a battery will not be necessary, leading to both the simplification and cost reduction for its fabrication process. The use of ''in situ formed'' solid electrolyte have been already shown in a primary battery system of Li/poly-2-vinylpyridide (P2VP)•I_2 (Greatbatch et al., 1971), which was commercialized as power sources of cardiac pacemakers. In this battery system, solid electrolyte of LiI was prepared at the negative electrode/positive electrode interface through the reaction of these electrodes. Neudecker et al. have proposed ''Lithium-free'' thin-film rechargeable lithium battery using LiPON, where electrochemically plated Li was used as an in situ formed anode material (Neudecker et al., 2000). Because of high reactivity of Li, the battery system required an overlayer to prevent side reactions with the Li anode. Lee et al. proposed a reversed structural configuration of the lithium-free battery so that the overlayer was not required. Although the use of in situ formed Li anode is very attractive to simplify the fabrication process, this battery system relies on specific stability of LiPON against lithium metal.

Most of oxide-based solid electrolyte dose not obtain such stability against lithium metal and then this technique will not be used to these solid electrolytes. It is well known that there are so many oxide-based solid electrolytes containing transition metal ions. It should be noted that some of these solid electrolytes can act as an electrode material when the electrode potential exceed their voltage windows. For example, $Li_3xLa_{(2/3)-x}TiO_3$($0.04 < x < 0.16$) (LLT) with ABO_3-perovskite structure can be an insertion electrode material after

reductive decomposition (Birke et al., 1997). When such a decomposition reaction is partially conducted in the solid electrolyte, decomposition product can be in situ formed electrode material combined with the solid electrolyte, that can be an unit of all-solid-state battery system. Based on the above concept, this chapter will introduce a possibility to fabricate an all-solid-state thin-film-type lithium-ion battery with in situ formed electrode material. In the next section, inorganic solid electrolytes, especially, oxide-based solid electrolyte including transition metals will be briefly summarized, and two examples of reductive decomposition reaction of solid electrolytes will be picked-up. Finally, examples of all-solid-state thin-film-type batteries with in-situ formed electrode active materials will be introduced.

2. Solid Electrolytes and their decomposition reaction

2.1 Lithium-ion conducting solid electrolytes

Lithium-ion conducting solid electrolytes used for all-solid-state rechargeable lithium batteries should provide the following electrical and physical properties in general.

1. High lithium-ion conductivity with negligible electronic conductivity at operating temperature, preferably at room temperature.
2. Wide potential window at both positive and negative electrode sides: sufficient stability against chemical reaction with both electrodes.
3. Environmentally benign, nonhygroscopic, low cost, and ease of preparation.

	Lithium-ion conductors	σ_{ionic} / S cm^{-1} (at R.T.)	Researchers	Year
①	LiI	1×10^{-7}	Ginnings and Phipps	1930
②	Li-βAl_2O_3	3×10^{-3}	Yao and Kummer	1967
③	Li_3N	10^{-3}	Alpen and Muller	1977
④	$Li_{14}Zn(GeO_4)_4$ (LISICON)	2×10^{-6} (at 323 K)	Hong	1978
⑤	$4.9LiI\text{-}34.1Li_2O\text{-}61B_2O_3$	2×10^{-7}	Malgani and Robert	1979
⑥	$Li_{3.6}Ge_{0.6}V_{0.4}O_4$	4×10^{-5}	Kuwano and West	1980
⑦	$0.30Li_2S\text{-}0.26B_2S_3\text{-}0.44LiI$	1.7×10^{-3}	Wada *et al.*	1983
⑧	$LiTi_2(PO_4)_3$	2×10^{-6}	Subramanian *et al.*	1986
⑨	$60Li_2S\text{-}40SiS_2$	4×10^{-4}	Pradel and Ribes	1986
⑩	$Li_{1.3}Al_{0.3}Ti_{1.7}(PO_4)_3$	7×10^{-4}	Aono *et al.*	1989
⑪	$0.02Li_3PO_4\text{-}0.98(Li_2S\text{-}SiS_2)$	7.6×10^{-4}	Takada *et al.*	1993
⑫	$Li_{0.35}La_{0.55}TiO_3$ (LLT)	1×10^{-3}	Inaguma *et al.*	1993
⑬	$Li_{2.9}PO_{3.3}N_{0.46}$ (LiPON)	2×10^{-6}	Bates *et al.*	1993
⑭	$2[Li_{1.4}Ti_2Si_{0.4}P_{2.6}O_{12}]\text{-}AlPO_4$	1.5×10^{-3}	Fu	1997
⑮	$Li_{3.25}Ge_{0.25}P_{0.25}S_4$ (Thio-LISICON)	2.2×10^{-3}	Kanno and Maruyama	2001
⑯	$0.7Li_2S \cdot 0.3P_2S_5$ glass-ceramics	3.2×10^{-3}	Mizuno *et al.*	2005

Table 1. Ionic conductivities of typical inorganic lithium-ion conductors.

Assuming that "solid electrolytes" are defined as lithium-ion conductors that are present in solid state in the macroscopic view, polymer or gel electrolytes will be included in the category. These electrolytes are excellent in terms of flexibility and ease of preparation. However, this chapter focuses on inorganic solid electrolyte mainly including transition metal oxides in them. Table 1 summarizes such inorganic lithium-ion conductors reported to

date. Figure 1 shows the temperature dependence of ionic conductivities for these conductors. Several kinds of conductors, such as Li-βAl_2O_3 (Yao and Kummer, 1967) and Li_3N (Rabenau, A., 1982), show high ionic conductivities (larger than 10^{-3} S cm^{-1}) even at room temperature, comparable to that of the currently used liquid or gel electrolytes in lithium-ion batteries. However, they are not simply used as solid electrolytes for lithium batteries because of their chemical instability. For example, Li_3N has a low decomposition potential (0.445 V (vs Li/Li^+)) so that its application to all-solid-state batteries is limited.

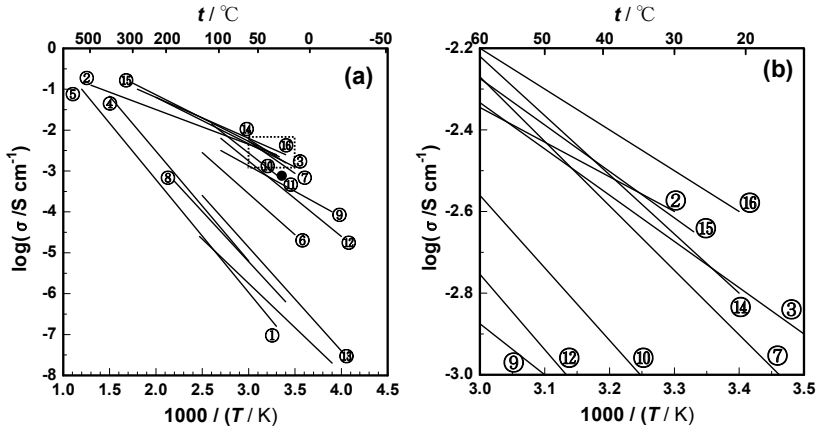

Fig. 1. (a)Temperature dependence of ionic conductivities for typical solid state lithium-ion conductors listed in Table 1. Dotted box in panel (a) is enlarged in panel (b).

Crystalline oxide-based inorganic solid electrolytes with higher chemical stability have been explored since the late 1970s. The material design of crystalline oxide-based ionic conductors is based on certain structural criteria: (i) mobile ions should have suitable sizes for conduction pathways in the lattice and (ii) there should be disorder in the mobile ion sublattice. Based on these considerations, solid solutions of Li_4GeO_4–Li_3VO_4, which is isostructural to $Li_{14}Zn(GeO_4)_4$ (lithium super ionic conductor; LISICON) (Hong 1978) related to the γ-Li_3PO_4 structure, were synthesized (Kuwano and West, 1980). Partial substitution of Li_4GeO_4 by Li_3VO_4 induced vacancies in the lithium sites, resulting in easier lithium-ion hopping in the structure. The substituted $Li_{3.6}Ge_{0.6}V_{0.4}O_4$ crystal attained ionic conductivity of 4×10^{-5} S cm^{-1} at room temperature, which were a few orders higher than those of the members. Another example is lithium lanthanum titanate, $Li_{3x}La_{(2/3)-x}TiO_3$ ($0.04 < x < 0.16$) (LLT) with ABO_3-perovskite structure (Inaguma et al., 1993). LLT showed high ionic conductivity, on the order of 10^{-3} S cm^{-1}, taking advantage of favorable lithium-ion hopping via *A*-sites in the perovskite structure.

Oxyacid-based solid electrolyte, typically $LiM_2(PO_4)_3$ (*M* = Ti (Subramanian et al., 1986), Fe (Sigaryov and Terziev, 1993), ...) compounds with NASICON (sodium (Na) super ionic conductor) structure, have been investigated progressively as solid electrolytes. Partial substitution of tetravalent M^{4+} ions in the $LiM_2(PO_4)_3$ by pentavalent A^{5+} ions or trivalent B^{3+} ions induced lithium-deficient $Li_{1-x}M_{2-x}A_x(PO_4)_3$ compounds or lithium-excess $Li_{1+x}M_{2-x}B_x(PO_4)_3$ compounds, respectively, which effectively enhance their ionic conductivities. Although the NASICON-based materials showed rather high ionic conductivities in the

bulk, they also exhibited large grain boundary resistances. To solve these problems, the M ions were partially substituted by Al or Sc, which enhanced the degree of sintering and increased the ionic conductivity at grain boundaries (Aono et al., 1989, 1990). The resultant $Li_{1.3}Ti_{1.7}Al_{0.3}(PO_4)_3$ showed the highest ionic conductivity among the NASICON-based materials, 7×10^{-4} S cm^{-1}. Taking advantage of the high ionically conductive $Li_{1.3}Ti_{1.7}Al_{0.3}(PO_4)_3$ phase mentioned above, Fu synthesized Li_2O–Al_2O_3–TiO_2–P_2O_5 glass ceramics showing ionic conductivity of 1.3×10^{-3} S cm^{-1} without grain boundary resistance (Fu, 1997). He subsequently optimized the elemental composition and reported in 1997 that $2[Li_{1.4}Ti_2Si_{0.4}P_{2.6}O_{12}]$-$AlPO_4$ glass-ceramics exhibited 1.5×10^{-3} S cm^{-1} at room temperature.

Oxide-based glassy materials have also been well studied as lithium-ion conducting solid electrolytes. They exhibit several advantages over crystalline electrolytes; in particular, they can provide isotropic ionic conduction without grain boundary resistance because of their random open framework. Development of oxide-based glassy electrolytes has been conducted based on the following two approaches. One is based on the Li*X*-Li_2O-M_xO_y (M_xO_y = B_2O_3, P_2O_5, GeO_2) glass system, which is an analog of lithium substitution of super silver-ion conducting glasses, Ag*X*-Ag_2O-M_xO_y, showing over 10^{-2} S cm^{-1} at room temperature. For example, LiI–Li_2O–B_2O_3 showed ionic conductivity of 10^{-7} S cm^{-1} (Malugani and Robert, 1979). Another approach stems from the discovery that rapid-quenched glasses of ferroelectric $LiNbO_3$ crystals showed high ionic conductivity of 10^{-5} S cm^{-1} (Glass et al., 1978). Based on this discovery, various kinds of oxyacid glasses have been synthesized. These include Li_4SiO_4–Li_3BO_3, Li_2O–SiO_2–$_2O_3$, and Li_2O–SiO_2–ZrO_2. Lithium phosphorus oxynitride (LiPON) glasses showed acceptable ionic conductivity (2×10^{-6} S cm^{-1}) when used for thin-film batteries (Bates et al., 1993). The LiPON glasses showed chemical stability against lithium metal because of their structural stability, originating from the introduction of nitrogen ions into the structure. The outstanding features of LiPON glass electrolytes have encouraged many researchers to study all-solid-state thin-film rechargeable lithium batteries using this solid electrolyte.

2.2 Decomposition of solid electrolyte and their lithium insertion/extraction reaction

As mentioned above, there have been many studies on the development of solid electrolytes, and various kinds of solid electrolyte have been discovered. It should be noted that there are many solid electrolytes containing 3*d*-transition metal ions: *e.g.*, V^{5+} in $Li_{3.6}Ge_{0.6}V_{0.4}O_4$ (Kuwano and West, 1980), Ti^{4+} in $Li_{1.3}Ti_{1.7}Al_{0.3}(PO_4)_3$ (Aono et al., 1989), $Li_{3x}La_{2/3-x}TiO_3$ (LLT) (Inaguma et al., 1993) and $2[Li_{1.4}Ti_2Si_{0.4}P_{2.6}O_{12}]$-$AlPO_4$ (Fu, 1997). These solid electrolytes are intrinsically susceptible to reductive decomposition accompanied by redox reactions of the transition metal ions through Li^+ insertion into them. It should be noted that transition metal oxides, such as CoO, FeO, NiO, etc, can work as high voltage negative electrode materials through conversion reaction (Poizot et al., 2000). Also, TiO_2 is well-known lithium insertion electrode material. In other words, when these transition metal oxides are prepared electrochemically in solid electrolyte vir the reductive decomposition reaction of solid electrolytes, the resultant material will work as electrode active materials. Moreover, because the decomposed material is grown from solid electrolytes, electrode/solid electrolyte interface with good adhesion can be simply prepared in principle. It is expected that success of such novel interface design become a breakthrough to develop advanced all-solid state battery system with low-cost and much smaller internal resistance. In this section, two examples of reductive decomposition of solid electrolytes will be introduced.

2.2.1 Li-V-Si-P-O system

An amorphous Li_2O–V_2O_5–SiO_2 system in which Li_2O and SiO_2 are expected to have a function as network modifier and network former, respectively, to stabilize the amorphous material. This system has been initially noted as a solid electrolyte in an analog of Li_3VO_4–Li_4SiO_4 solid solution. Bulk crystals of $Li_{3.4}V_{0.6}Si_{0.4}O_4$ with a γ-Li_3PO_4 structure, which is isostructural to the so-called lithium superionic conductor "LISICON" showed high ionic conductivity of 1 x 10^{-5} S cm^{-1} with negligible electronic conductivity at room temperature, which has encouraged several researchers to study all-solid-state batteries using this solid electrolyte. Thin solid electrolyte films of the Li–V–Si–O system have been reported to show acceptable ionic conductivity as an application for all-solid-state thin-film batteries. Partially crystallized Li–V–Si–O thin films have been prepared by r.f. magnetron sputtering (Ohtsuka and Yamaki, 1989) and amorphous one have been by pulsed laser deposition (PLD) (Kawamura et al., 2004). These film electrolytes have been successfully used in all-solid-state thin-film batteries. Here we report "charge/discharge" properties of the Li–V–Si–O thin film, aiming at utilizing redox reactions of multivalent vanadium ions. Following the results, the feasibility of applying the Li–V–Si–O films as high-voltage negative electrode materials is discussed (Yada et al., 2006).

Characterization of a pristine Li–V–Si–O thin solid electrolyte film.

An XRD pattern of the pristine Li–V–Si–O thin film showed no characteristic peaks other than those originating from the substrate, indicating that no crystalline phase was confirmed in the film. Figure 2 shows a Cole-Cole plot of an ionically blocking cell, Pt/Li–V–Si–O/Pt, measured at 298 K. The spectrum consisted of one semicircle in the higher frequency region followed by a nearly vertical tail, suggesting that the electrical conductivity of the film is fairly dominated by ionic conduction. The semicircle can be assigned to the ionic conduction in the Li–V–Si–O thin solid electrolyte film, whose characteristic frequency was ca. 10 kHz.

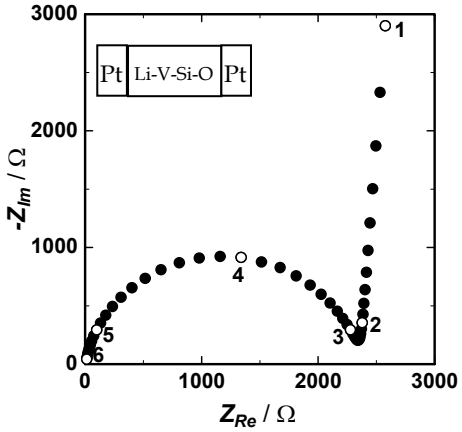

Fig. 2. Cole-Cole plot of Pt/Li-V-Si-O/Pt (750 nm in thickness, 0.25 cm^2 in electrode area) measured at 298 K. Open circles are data points obtained at 10^n Hz, where n is denoted near the open circles.

The ionic conductivity of the film at 298 K was 1.3×10^{-7} S cm^{-1}. The electronic contribution to the total electric conductivity was evaluated by two-electrode dc polarization technique, indicating that the transference number of lithium ions in the film was almost unity. The activation energy for ionic conduction in the film was 56.5 kJ mol^{-1}. These results are in good agreement with the previous reports.

Charge/discharge properties of a Li–V–Si–O thin solid electrolyte film.

Although the prepared thin films can work well as solid electrolytes in appropriate potential region, once the potential exceeds over the limitation of potential windows, they are irreversible decomposed. Here, electrochemical properties of the reductively decomposed material as an anode material and its decomposition process will be discussed below.

Figure 3(a) and (b) shows typical charge/discharge profiles of the Li–V–Si–O thin solid electrolyte film obtained at 12.8 μA cm^{-2} in the 1st and 47th cycles and at 2.55 μA cm^{-2} in the 48th and 90th cycles, respectively. The OCV of the film electrolyte before the charge/discharge reaction was 2.8 V. In the first discharge, the electrode potential dropped steeply from the OCV to ca. 1.7 V, followed by an asymptotic potential decrease to 1.0 V with a capacity of 3.8 μAh cm^{-2}. In the first charge, however, the potential rapidly increased and immediately reached 4.0 V, whose capacity was only 0.8 μAh cm^{-2}. The difference between the discharge and charge capacities observed at the first cycle, 3.0 μAh cm^{-2}, would be consumed to decompose the Li–V–Si–O thin solid electrolyte film. In the subsequent charge/discharge cycles, the difference in the discharge and charge capacities, irreversible capacity, gradually decreased with the repetition of the charge/discharge reaction. At the 47th cycle, the irreversible capacity became very small and the reversible charge/discharge capacity increased to 2.6 μAh cm^{-2}. When the current density was decreased to 2.55 μA cm^{-2}, Figure 3(b), the discharge and charge capacities increased to 20 and 13 μAh cm^{-2}, respectively, and the irreversible capacity was observed again. This would be attributed to much more decomposition of the film electrolyte due to the smaller overpotential resulting from the smaller current density. In the prolonged cycles, both the discharge and charge capacities constantly increased and achieved 58 and 52 μAh cm^{-2}, respectively, at the 90th cycle. The increase in the capacities was brought by microstructural reformation of the film, as is discussed later. Figure 4 summarizes the variation in the charge/discharge capacities of the film as a function of the cycle number. Obvious increases in the charge/discharge capacities were observed during the 48th–90th cycles. When the current density was increased to 12.8 μA cm^{-2} again (91st–108th cycles), the charge/discharge capacities maintained almost the same value, 38 μAh cm^{-2}, which was ca. 10 times larger than that obtained at the 1st–47th cycles. When the current density was decreased to 2.6 μA cm^{-2} (109th–119^{th} cycles) again, the charge/discharge capacities did not increase further and showed almost the same value of 60 μAh cm^{-2}.

SEM images revealed that the Li–V–Si–O thin film became rough after the charge/discharge measurement. This micro structural reformation would be due to stress relaxation of the film by the repetition of lithium insertion/extraction reaction. Also, XPS analysis revealed that mean valence of vanadium decrease, indicating that the valence change of vanadium concerns with the redox reaction. In the pristine film, asymmetric peaks of V 2p1/2 at around 523 eV and V 2p3/2 at around 516 eV, which can be deconvoluted to peaks originating from V5+ and V4+ was observed. On the other hand, the film retained at 1.0 V

gave lower binding energies, meaning the presence of lower oxidation number (+2.5) than the pristine film.

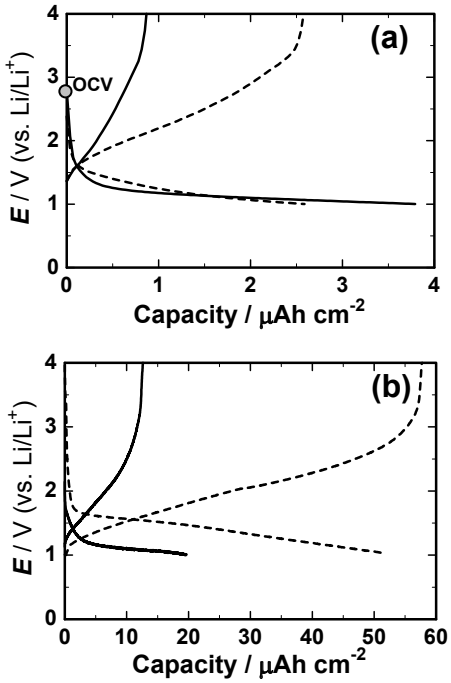

Fig. 3. (a) Charge/discharge profiles of Li-V-Si-O thin film obtained at a current rate of 12.8 μA cm^{-2} in (-)1st cycle and (---)47th cycle. (b) Charge/discharge profiles of Li-V-Si-O thin film obtained at a current rate of 2.55 μA cm^{-2} in (-)48th cycle and (---)90th cycle.

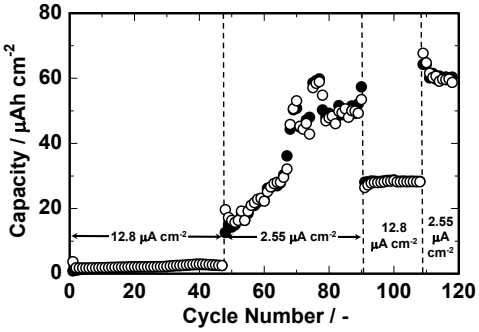

Fig. 4. (●)Charge and (○)discharge capacities as a function of cycle number for Li-V-Si-O thin film obtained at current rates of 12.8 μA cm^{-2} and 2.55 μA cm^{-2}. Cutoff voltages are 1.0 and 4.0 V (vs. Li/Li+).

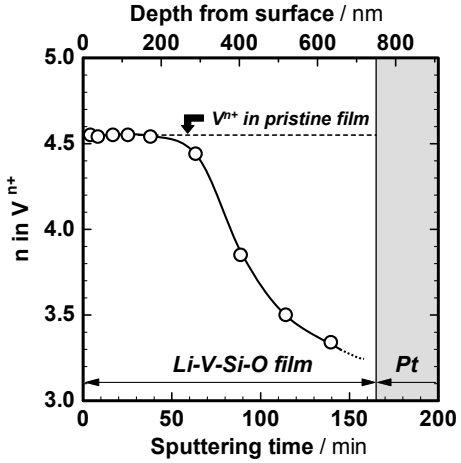

Fig. 5. Depth profile of average oxidation state of vanadium-ions in partially decomposed Li-V-Si-O thin film.

In order to investigate this decomposition process of the Li–V–Si–O thin solid electrolyte film, XPS analysis was conducted to a partially decomposed Li–V–Si–O thin film, which was prepared by applying current of 2.55 μA cm^{-2} reductively until the electrode potential reached 1.0 V. The depth profile of average oxidation numbers of vanadium ions is summarized in Figure 5. The V 2p binding energies maintained their initial state until the middle of the thin film; the average oxidation number of vanadium ions kept the initial state. However, they gradually shifted to the lower energy levels as ion milling time increased, indicating that the average oxidation number of vanadium ions gradually decreased toward the depth direction. These results indicate that the decomposition of the Li–V–Si–O thin solid electrolyte film started from the current collector side. Because charge/discharge reaction was available for the partially decomposed film as well, the part in the vicinity of the current collector performed as an electrode material. This result indicates that both an electrode material and a solid electrolyte coexisted in the partially decomposed Li–V–Si–O thin film.

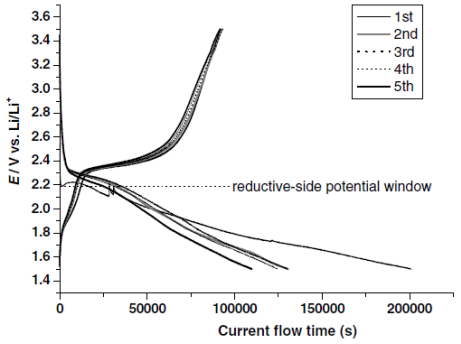

Fig. 6. Charge–discharge curves of Cu/OHARA sheet in 1 mol dm^{-3} $LiClO_4$ dissolved in propylene carbonate between 3.5 and 1.5 V. I = 1.0 μA.

2.2.2 Li-Al-Si-Ti-O system

As with the case of Li-V-Si-O system, crystalline-glass electrolyte (Li-Al-Si-Ti-O system) also shows interesting reductive decomposition reaction. The glass electrolyte sheet with 150 μm in thickness obtains $1x10^{-4}$ S cm^{-1} in its Li^+ conductivity at room temperature, and its activation energy for the Li^+ conduction in the bulk is 30 kJ mol^{-1}, which was manufactured by Ohara Inc. Electrochemical lithium insertion/extraction reaction of the OHARA sheet was investigated using a three-electrode cell. Working electrode was the Cu film deposited on one side of the OHARA sheet. Opposite side of the OHARA sheet was bare. The counter and reference electrodes were lithium metal. The liquid electrolyte, propylene carbonate (PC) containing 1 mol dm^{-3} $LiClO_4$, was filled only into bare side of the OHARA sheet. Electrochemical lithium insertion/extraction reaction of the OHARA sheet was carried out at a constant current of 2.5 μA cm^{-2} in an argon-filled glove box.

Figure 6 shows charge–discharge curve of the "OHARA sheet". The charging process (lithium insertion reaction) at first cycle starts at 2.2 V (vs. Li/Li^+). This potential generally considers as reductive-side potential window of the OHARA sheet. After that, the potential gradually decreased with increasing current flow time from 2.2 to 1.6 V. In the discharge process (lithium extraction reaction) at first cycle, potential plateau was clearly observed at 2.3 V. This discharge capacity was smaller than that of the charging capacity, indicating that the charge–discharge reaction at first cycle is not reversible reaction but includes some irreversible reactions. This irreversible reaction will be responsible for decomposition reaction of the OHARA sheet, and the resultant decomposition material becomes an insertion electrode material operating at 2.3 V vs. Li/Li^+. The charge–discharge capacities were preserved after the second cycles.

The pristine OHARA sheet is white color. The OHARA sheet after the charge–discharge reaction maintained its initial color at the organic electrolyte side while the current collector (Cu) side became dark blue. This dark blue region never returned to its pristine white color even after maintaining its open circuit voltage. This indicates that the dark blue region was irreversibly formed in the OHARA sheet only around Cu current collector. It will be reasonable to expect that this dark blue region is the decomposition material formed at the first charging process and that this region can act as the electrode material. XPS analysis showed that reduced Ti peak was observed at the blue colored region, and this Ti will work as the redox species in the in-situ formed electrode material.

Both Li-V-Si-P-O glass electrolyte and Li-Al-Si-Ti-O crystalline glass sheet start gradual reductive decomposition reaction from current collector side. This decomposition process is not universal phenomena in solid electrolytes and seems to strongly depend on the species of solid electrolytes.

3. Thin-film type batteries with *in-situ* formed materials

As mentioned above, reductively decomposed material of solid electrolyte works as lithium insertion material. Here, manufacturing examples using in-situ formed material in all-solid-state battery system on one side (Iriyama et al., 2006) or both sides (Yada et al., 2009) will be shown below, where OHARA sheet was mainly used as a model solid electrolyte.

3.1 Battery with in-situ formed electrode material on one side

Amorphous lithium manganese oxide thin film was deposited to one side of the sheet by pulsed laser deposition at room temperature. After that, metal film of Pt was deposited on it as a current collector by r.f. magnetron sputtering. Subsequently, metal film of Cu was deposited on the opposite side as a current collector by the sputtering, and a layer of Cu/OHARA sheet/amorphous Li–Mn–O/Pt was fabricated. Voltage of the resultant layer was 0 V. A D.C. 400 V was applied to the resultant layer for a few seconds at room temperature, where Cu side was connected to cathode and Pt side to anode. After the high voltage application, voltage of the layer gradually decreased with time and, finally, it stabilized at 1.7 V. Charge–discharge reaction of the resultant ''all-solid-state thin-film-type lithium-ion battery'' was conducted by 1 μA cm^{-2} between 2.2 and 1.0 V at room temperature. Figure 7(a) shows a plausible fabrication scheme of this battery.

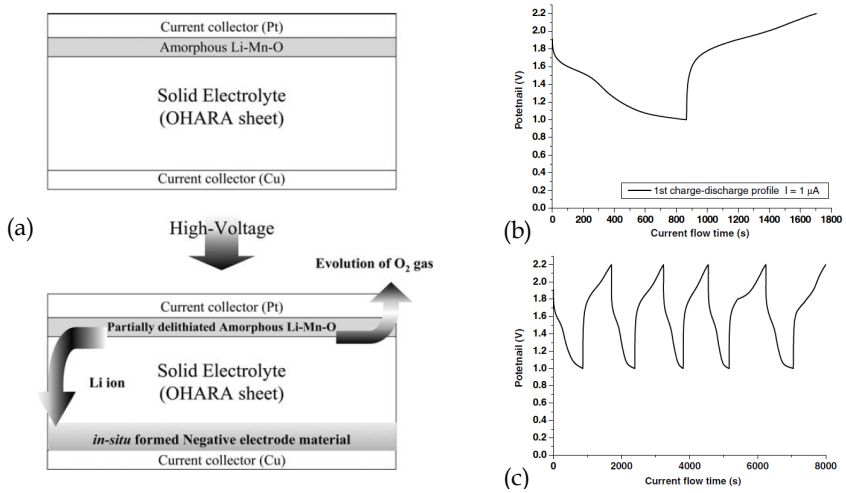

Fig. 7. (a)A plausible fabrication scheme for all-solid-state rechargeable lithium-ion battery (Cu/OHARA sheet/amorphous Li–Mn–O/Pt) developed by applying D.C. high voltage. Charge–discharge curves of the above battery developed by applying D.C. high voltage: (b) charge–discharge curve at first cycle and (b) sequential charge–discharge curves. I = 1.0 μA.

Figures 7(b) and 7(c) show charge–discharge cycles of the resultant all-solid-state thin-film-type lithium-ion battery between 1.0 and 2.2 V. As shown in Fig. 7(b), this battery obtained charge–discharge reaction at around 1.4 V. The irreversible capacity at first cycle was small, and the battery could repeat stable charge–discharge reaction as shown in Fig. 7(c). The charge–discharge reaction of OHARA sheet proceeds at 2.3 V vs. Li/Li^+ as shown in Fig. 6. On the other hand, electrochemical lithium insertion/extraction reaction of amorphous Li–Mn–O occurs at around 3.7 V (Yokoyama et al., 2003). Hence, operating voltage of the resultant battery will be due to the difference of redox potential of these two electrodes.

Cross-sectional SEM image revealed interesting structural change. Figures 8(a) and 8(b) illustrate the cross-sectional SEM images at the amorphous Li–Mn–O/OHARA sheet interface before and after applying the high voltage, respectively. As shown in Fig. 8(a), the as-deposited amorphous Li–Mn–O film electrode was composed of fine particles and these

particles mounted densely on the OHARA sheet. Once the high voltage was applied on the layer, some of cavities were clearly formed at around the amorphous Li–Mn–O/OHARA sheet interface as shown in Fig. 8(b). The cavities seemed to be formed mainly in the amorphous Li–Mn–O film electrode. In addition, the amorphous Li–Mn–O thin film became smooth after applying the high voltage, which may be due to resistive heat generated by applying the high voltage. Figs. 8(c) and 8(d) show the cross-sectional SEM images at the Cu/OHARA sheet interface, respectively. In comparison with the OHARA sheet/amorphous Li–Mn–O interface, the Cu/OHARA sheet interface did not show clear differences before and after applying the high voltage.

As mentioned above, all-solid-state thin-film-type lithiumion battery with in situ formed negative electrode material can be prepared by applying a D.C. high voltage to a Cu/OHARA sheet/amorphous Li–Mn–O/Pt layer. The OHARA sheet around the Cu current collector decomposed irreversibly by application of the high voltage, resulting in negative electrode material in situ formed at Cu/OHARA sheet interface. This negative electrode material obtained reversible charge–discharge capacity in the potential window of the original OHARA sheet. Also, at positive electrode side, oxidation reaction of oxygen ions will occur around the electrode/solid electrolyte interface in addition to the lithium extraction from amorphous Li–Mn–O. It is suggested that oxidation current due to the oxidation reaction of oxygen ions compensated reduction current required to form the negative electrode material. The resultant all-solid state thin-film-type lithium-ion battery operated at 1.4 V, repeated stable charge–discharge reaction, and obtained reversible charge–discharge capacity from the initial charge–discharge cycle.

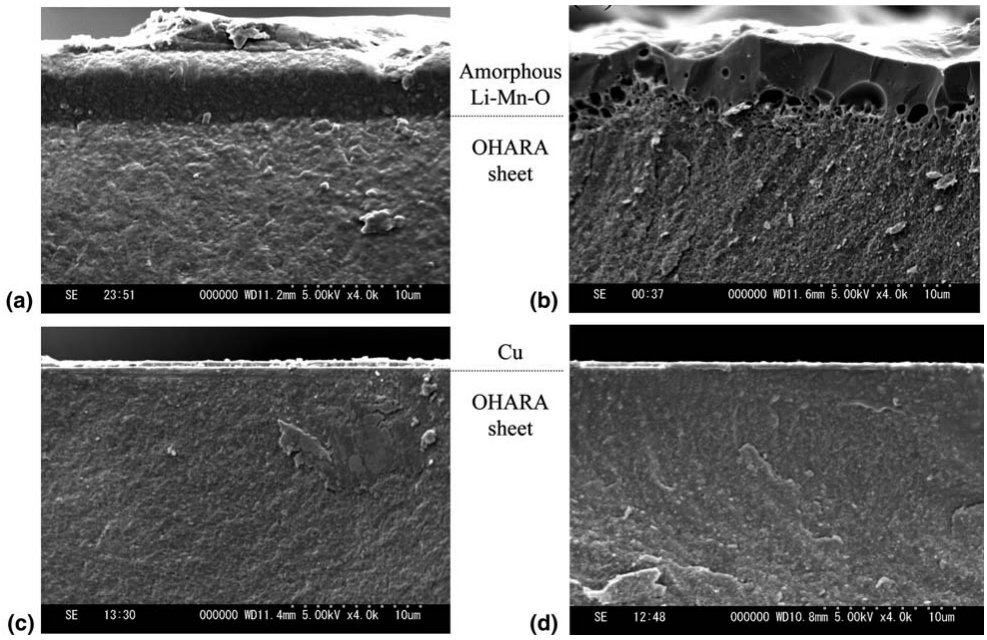

Fig. 8. Cross-sectional SEM images of amorphous Li–Mn–O/OHARA sheet interface: (a) before and (b) after applying D.C. high voltage. Cross-sectional SEM images of OHARA sheet/Cu interface: (c) before and (d) after applying D.C. high voltage.

In-situ preparation of positive electrode material has been investigated using LiPON films (Iriyama et al, 2008). In this case, electrochemical oxidation of iron and the iron ions diffusion into LiPON film was used to fabricate *in-situ* formed iron phosphate amorphous electrode. Although the interfacial resistance at the resultant *in-situ* formed electrode/LiPON interface became smaller than that at the amorphous lithium iron-phosphate/LiPON interface where the film electrode was deposited on LiPON film by PLD, the resultant batter obtained quite small capacity. This is probably because of the difficulty of iron ions diffusion into internal region of LiPON film.

3.2 Battery with *in-situ* formed electrode materials on both sides

In the previous system, electrode material on one side was prepared by in-situ process. In case of negative electrode side, the electrode active material was reductively decomposed material from the solid electrolyte (OHARA sheet) and formed only around the Cu current collector. However, only one electrode active material was prepared. Preparation of both electrodes by in-situ process would simplify the fabrication process markedly. In this paper, a novel all-solid-state battery with in-situ formed electrodes on both sides.

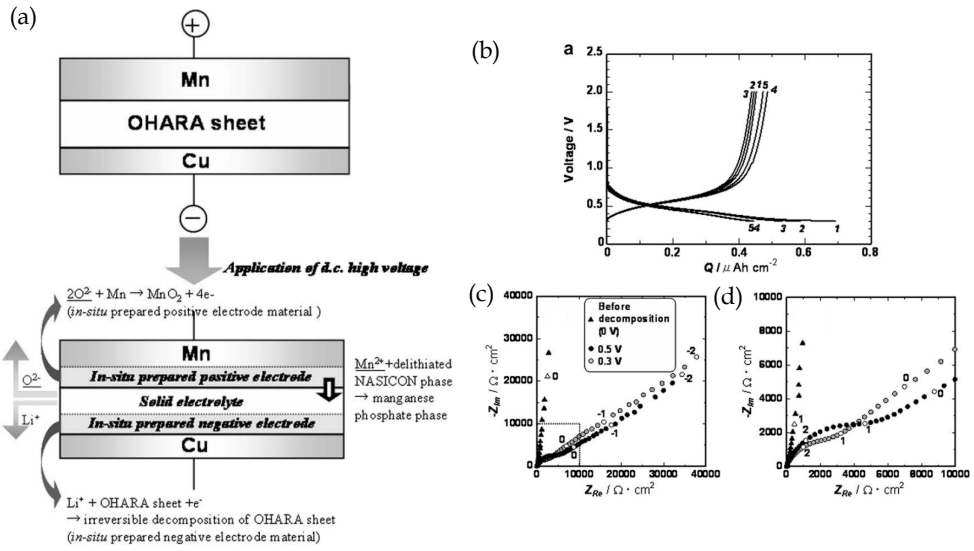

Fig. 9. (a) Charge–discharge profiles of an all-solid-state Cu/OHARA sheet/Mn battery (electrode area: 0.15 cm^2, thickness: 0.03 cm). I = 0.33 μA cm^{-2}. Cycle numbers are denoted at the end of the charge–discharge curves. (b) Cole-Cole plots of the Cu/OHARA sheet/Mn battery. Magnified image of high frequency region in (b) (surrounded by dotted square) is shown in (c). Open symbols are data points obtained at 10^n Hz, where n is denoted near the open symbols.

A layer of Cu metal film/OHARA sheet/Mn metal film shown in Fig. 9 was fabricated in the following manner. Thin-film of Cu (thickness: 0.5 μm, area: 0.15 cm^2) was deposited on one side of the OHARA sheet by r.f. magnetron sputtering method with r.f. power of 40W

under argon atmosphere (1.5 Pa). After that, Mn thin-film (thickness: 1.5 μm, area: 0.15 cm^2) was deposited on the other side of the OHARA sheet by vacuum evaporation. D.c. 16 V was applied to the resultant Cu/OHARA sheet/Mn layer for 10 h at 353 K in air, where the Cu side was connected to cathode and the Mn side to anode. This high voltage application made the layer to a Cu/OHARA sheet/Mn battery. A plausible battery preparation scheme is shown in Fig. 9(a). Hereafter, as-prepared Cu/OHARA sheet/Mn layer and the resultant Cu/OHARA sheet/Mn battery are referred to as COM layer and COM battery, respectively. Figure 9(b) shows the charge–discharge profiles of the COM battery between 0.3 V and 2.0 V. A clear charge–discharge capacity was observed at 0.3–0.8 V, while the COM layer did not have any capacity in this voltage range. The irreversible capacity was ca. 0.25 μAh cm^{-2} at the initial cycle and decreased with repetition of the charge–discharge reactions. A stable, reversible capacity of 0.45 μAh cm^{-2} was observed at the fifth cycles. Figs. 9(c) and 9(d) show Cole-Cole plots of the COM battery measured at 0.3 and 0.5 V. Cole-Cole plot of the COM layer is also displayed in these figures for comparison. The Cole-Cole plot of the COM layer consisted of a nearly vertical line to the real axis with a resistive component (20 Ω cm^2) in the high frequency region. The resistive component was assigned to the resistance of the OHARA sheet. This result indicates that both the Cu and Mn metal films performed as ionically blocking electrodes. On the other hand, Cole-Cole plots of the COM battery showed a depressed semicircular arc in the middle frequency region (10 Hz < f < 100 kHz) together with a slope of nearly 45° to the real axis in the low frequency region (f < 10 Hz).
The diameter of this semicircular arc depended on the cell voltage, suggesting that this semicircular arc contains charge transfer resistances at the in situ prepared electrodes/solid electrolyte interface. The slope of nearly 45° observed at lower frequency region would correspond to Warburg impedance in the in situ prepared electrode materials. This result supports that the electrode active materials are prepared at both sides just by applying d.c. high voltage to COM layer. As shown in Fig. 9(a), the in-situ prepared negative electrode material will be a partially decomposed OHARA sheet around the Cu current corrector as discussed in previous section. In this preparation process, excess Li^+ is required to decompose the OHARA sheet irreversibly for the fabrication of the negative electrode material. The Li^+ source for the reductive decomposition is restricted to the OHARA sheet itself. Therefore, to promote Li^+ migration in the OHARA sheet to the Cu side so that Li^+ is consumed in the irreversible preparation of the negative electrode material, charge compensation is necessary at the positive electrode side in the OHARA sheet. One of the most significant reactions would be the release of oxygen ions from the OHARA sheet at the positive electrode side. If the released oxygen ions react with the Mn film at the OHARA sheet/Mn interface, formation of a manganese oxide will be expected. Once the dense MnO_2 phase is formed at the interface, it is speculated that counter diffusion of both manganese ions and oxide ions in the MnO_2 will grow the phase. Such diffusion will not proceed so fast, which will be one of the reasons for the small quantity of the resultant MnO_2 phase. The lithium insertion/extraction reaction to the MnO_2 occurs at ca. 3 V (Thackeray, 1997) and the half cell test also revealed that lithium insertion/extraction reaction at OHARA sheet/Mn film of the COM battery operated at ca. 3.0 V. On the other hand, lithium insertion/extraction reaction to the decomposed OHARA sheet occurs at ca. 2.3 V. Difference of this lithium insertion/extraction potential in these two electrodes will be reasonably agreement with the cell voltage shown in Fig. 9(b). Although oxygen ions in the OHARA sheet will interact strongly with phosphorus to form PO_4, free energy change for

the oxidation reaction of Mn has a relatively large negative value (Kubaschewski, 1978), which can promote the release of oxygen ions. XRD showed that Mn layer in the COM battery was mainly Mn metal and could not detect such manganese oxide phase, but this will be probably because of its small quantity. Another possibility that should be considered will be an oxidation of Mn and formation of a manganese phosphate phase due to the migration of Mn^{2+} into the OHARA sheet. The crystalline part of the OHARA sheet is mainly the composition of $LiTi_2(PO_4)_3$, where lithium locate at M1 site in the structure. Aatiq et al. have pointed out that Mn^{2+} can occupy the M1 site, resulting in the formation of $(Mn_{0.5})M_1Ti_2(PO_4)_3$ phase (Artiq et al., 2001, 2002). They have reported that lithium insertion into the M1 site of $Li_xMn_{0.5}Ti_2(PO_4)_3$ phase leads to a potential plateau in the vicinity of 2.9 V (Li/Li+) at $0 < x < 0.5$, following to the insertion into the M2 site around 2.2–2.5 V (Li/Li+). When the lithium content of M1 sites around Mn film decrease due to the migration of Li+ into Cu film side, a part of Mn^{2+} migration into the M1 sites for the charge compensation may be considerable. However, the lithium insertion process at 2.9 V region was not observed in half cell test. Hence, we consider that this charge–discharge capacity will not contribute so much to the capacity observed in Fig. 9(b).

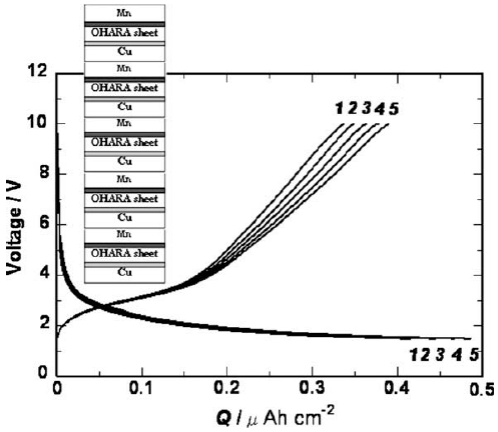

Fig. 10. Charge–discharge profiles of a five-series of all-solid-state Cu/OHARA sheet/Mn battery (electrode area: 0.15 cm², thickness: 0.15 cm) measured at 353 K. I = 0.33 μA cm-2. Cycle numbers are denoted at the end of the charge–discharge curves.

One of the problems of the proposed COM battery is its low usable voltage (0.3–0.8 V), which is too small for practical applications. To overcome this problem, a d.c. 16 V was applied to a series of five COM layers. Charge–discharge profiles of the resultant fiveseries COM batteries are shown in Fig. 10. The battery had charge–discharge reactions of 1.5–4.0 V, which was five times larger voltage than that of the single battery. This result indicate that COM batteries with high voltages can be easily fabricated by stacking many layers serially and applying appropriate d.c. high voltage to promote the in situ fabrication of electrode active materials at the positive and negative sides. The energy density per unit cell can be simply increased by reducing the thickness of solid electrolyte. Our calculation indicates that a cell made with an OHARA sheet (5.0 μm in thickness) has an energy density of ca. 0.1 Wh kg-1, which is nearly equivalent to that of the popular electrolytic capacitor. It is true that

the capacity of the COM battery is also small, but this will be improved by increasing the interface region, for example using three-dimensional porous solid electrolyte with high surface area (Kanamura et al., 2005).

4. Conclusion

In this chapter, new kinds of all-solid-state Li-ion battery with in-situ formed electrode material were introduced. Generally, decomposition reaction of solid electrolytes has considered as a limitation of voltage, the resultant decomposed material sometimes work as in-situ formed electrode materials. In addition, when the decomposed materials grow uniformly from the current collector, solid electrolyte/electrode interface can be formed by in-situ process that can be used in all-solid-state batteries. Because the large resistance at the electrode/solid electrolyte interface is a crucial problem to develop high power all-solid-state lithium-ion batteries, this novel fabrication process may become an effective method to reduce the interfacial resistance. However, in the current stage, this proposed battery does not obtain sufficient electrochemical properties, typically, on capacity, reaction rate, and voltage. To overcome these problems, mechanism of decomposition reaction of solid electrolytes and their characterization should be fundamentally clarified, which are currently investigated.

5. References

Aatiq, A.; Delmas, C.; El Jazouli, A. (2001). Structural and electrochemical study of $Li_{0.5}Mn_{0.5}Ti_{1.5}Cr_{0.5}(PO_4)_3$. *Journal of Solid State Chemistry*, Vol. 158, No. 2, p169-174, 0022-4596.

Aatiq, A.; Menetrier, M.; El Jazouli, A. & Delmas, C. (2002). Structural and lithium intercalation studies of $Mn_{(0.5-x)}Ca_xTi_2(PO_4)_3$ phases ($0<x<0.50$). *Solid State Ionics, Diffusion & Reactions*, Vol. 150, No. 3-4, p. 391-405, 0167-2738.

Aono, H.; Sugimoto, E.; Sadaoka, Y.; Imanaka, N. & Adachi, G. (1989). Ionic conductivity of the lithium titanium phosphate ($Li_{1+x}MxTi_{2-x}(PO_4)_3$, M=Al, Sc, Y, and La) systems. *Journal of the Electrochemical Society*, Vol. 136, No. 2, p590-591, 0013-4651.

Aono, H.; Sugimoto, E.; Sadaoka, Y.; Imanaka, N. & Adachi, G. (1990). Ionic conductivity of solid electrolytes based on lithium titanium phosphate. *Journal of the Electrochemical Society*, Vol. 137, No. 4, p1023-1027, 0013-4651.

Bates, J. B.; Dudney, N. J.; Gruzalski, G. R.; Zuhr, R. A.; Choudhury, A.; Luck, C. F. & Robertson, J. D. (1993). FABRICATION AND CHARACTERIZATION OF AMORPHOUS LITHIUM ELECTROLYTE THIN-FILMS AND RECHARGEABLE THIN-FILM BATTERIES. *Journal of Power Sources*, Vol. 43, No.1-3, p. 103-110, 0378-7753.

Birke, P.; Scharner, S.; Huggins, R. A. & Weppner, W. (1997), Electrolytic stability limit and rapid lithium insertion in the fast-ion-conducting $Li_{0.29}La_{0.57}TiO_3$ perovskite-type compound, *Journal of the Electrochemical Society*, Vol. 144, No. 6, pL167-L169, 0013-4651.

Fu, J. (1997). Fast Li^+ ion conduction in Li_2O-Al_2O_3-TiO_2-SiO_2-P_2O_5 glass-ceramics. *Journal of the American Ceramic Society*, Vol. 80, No. 7, p1901-1903, 0002-7820.

Glass, A.M.; Nassau, K. & Negran, T. J. (1978). Ionic conductivity of quenched alkali niobate and tantalate glasses. *Journal of Applied Physics*, Vol. 49, No. 9, p4808-4811, 0021-8979.

Greatbatch, W.; Lee, J. H.; Mathias, W.; Eldridge, M.; Moser, J. R. & Schneider, A. A.(1971) *IEEE Transactions on Biomedical Engineering*, Vol. BME-18, No. 5, p317-324, 0018-9294.

Hong, H. Y. P. (1978). Crystal structure and ionic conductivity of $Li_{14}Zn(GeO_4)_4$ and other new Li^+ superionic conductors. *Materials Research Bulletin,* Vol. 13, No. 2, p117-124, 0025-5408.

Inaguma, Y.; Liquan, C.; Itoh, M.; Nakamura, T.; Uchida, T.; Ikuta, H. & Wakihara, M. (1993). High ionic conductivity in lithium lanthanum titanate. *Solid State Communications*, Vol. 86, No. 10, p689-693, 0038-1098.

Iriyama, Y.; Yada, C.; Abe, T.; Ogumi, Z. & Kikuchi, K. (2006). A new kind of all-solid-state thin-film-type lithium-ion battery developed by applying a DC high voltage. *Electrochemistry Communications*, Vol. 8, No. 8, p1287-1291, 1388-2481.

Iriyama, Y.; Shimidu, D.; Abe, T.; Sudoh, M.; & Ogumi, Z. (2008). Fast and Stable Charge Transfer Reaction at the $Li_{4/3}Ti_{5/3}O_4$/Lithium Phosphorus Oxynitride (LIPON) Interface and its Application to All-Solid-State Thin Film Batteries, ECS Transactions of 214th ECS Joint Meeting "PRiME 2008", p45-52, Vol. 16, No. 26, Honolulu, Oct. 12-17, 2008, ECS.

Kanamura, K.; Akutagawa, N. & Dokko, K. (2005). Three dimensionally ordered composite solid materials for all solid-state rechargeable lithium batteries. *Journal of Power Sources*, Vol. 146, No. 1-2, p86-89, 0378-7753.

Kawamura, J.; Kuwata, N.; Toribami, K.; Sata, N.; Kamishima, O. & Hattori, T. (2004). Preparation of amorphous lithium ion conductor thin films by pulsed laser deposition. *Solid State Ionics, Diffusion & Reactions*, Vol. 175, No. 1-4, p273-276, 0167-2738.

Kubaschewski, O. & Alcock C. B. (1979). *Metallurgical Thermochemistry, fifth ed.,* Pergamon Press, 0080208975, New York.

Kuwano, J. & West, A.R. (1980). New Li^+ ion conductors in the system, Li_4GeO_4-Li_3VO_4. *Materials Research Bulletin*, Vol. 15, No. 11, p1661-1667, 0025-5408.

Malugani, J.P. & Robert, G. (1979). Ionic conductivity of the glasses $LiPO_3$-LiX(X=I, Br, Cl). *Materials Research Bulletin*, Vol. 14, No. 8, p.1075-1081, 0025-5408 .

Neudecker, B. J.; Dudney, N. J. & Bates, J. B. (2000). "Lithium-free" thin-film battery with in situ plated Li anode. *Journal of the Electrochemical Society*, Vol. 147, No. 2, p517-523, 0013-4651.

Ohtsuka, H. & Yamaki, J. (1989). Electrical characteristics of Li_2O-V_2O_5-SiO_2 thin films. *Solid State Ionics, Diffusion & Reactions*, Vol. 35, No. 3-4, p201-206, 0167-2738.

Rabenau, A. (1982). Lithium nitride and related materials case study of the use of modern solid state research techniques. *Solid State Ionics*, Vol. 6, No. 4, p277-293, 0167-2738.

Radzilowski, R. H.; Yao, Y. F. & Kummer, J. T. (1969). Dielectric loss of beta alumina and of ion-exchanged beta alumina. *Journal of Applied Physics,* Vol. 40, No. 12, p4716-4725, 0021-8979.

Sigaryov, S.E. & V.G. Terziev. (1993). Thermally induced lithium disorder in $Li_3Fe_2(PO_4)_3$. *Physical Review B (Condensed Matter)*, Vol. 48, No. 22, p16252-16255, 0163-1829.

Subramanian, M.A.; Subramanian, R. & Clearfield, A. (1986). Lithium ion conductors in the system AB(IV) $_2(PO_4)_3$ (B=Ti, Zr and Hf). *Solid State Ionics, Diffusion & Reactions,* Vol. 18-19, p562-569, 0167-2738 .

Thackeray, M.M. (1997). Manganese oxides for lithium batteries. *Progress in Solid State Chemistry*, Vol. 25, No. 1-2, p1-71, 0079-6786.

Wang, B.; Bates, J. B.; Hart, F. X.; Sales, B. C.; Zuhr, R. A. & Robertson, J. D. (1996) Characterization of thin-film rechargeable lithium batteries with lithium cobalt oxide cathodes, *Journal of the Electrochemical Society*, Vol. 143, No.10, p3203-3213, 0013-4651.

Yada, C.; Iriyama, Y.; Abe, T.; Kikuchi, K. & Ogumi, Z. (2006). Amorphous Li-V-Si-O thin films as high-voltage negative electrode materials for thin-film rechargeable lithium-ion batteries. *Journal of the Electrochemical Society*, Vol. 153, No. 6, pA1148-A1153, 0013-4651.

Yada, C.; Iriyama, Y.; Abe, T.; Kikuchi, K. & Ogumi, Z. (2009). A novel all-solid-state thin-film-type lithium-ion battery with in situ prepared positive and negative electrode materials. *Electrochemistry Communications*, Vol. 11, No. 2, p413-416, 1388-2481.

Yokoyama, M.; Iriyama, Y.; Abe, T. & Ogumi, Z. (2003). Dependency on the electrode species of Li ion transfer at the electrode/glass electrolyte (LiPON) interface, *Proceedings of the 44th Battery Symposium*, p290-291, Osaka, November, Seiei, Ohsaka.

5

NASICON Open Framework Structured Transition Metal Oxides for Lithium Batteries

[1]K.M. Begam, [2]M.S. Michael and [3]S.R.S. Prabaharan
Department of Electrical Engineering, Universiti Teknologi PETRONAS
Malaysia
Department of Chemistry, S.S.N. Engineering College, Chennai
India
Faculty of Engineering, The University of Nottingham
Malaysia

1. Introduction

Since the dawn of civilization, world has become increasingly addicted to electricity due to its utmost necessity for human life. The demand for electrically operated devices led to a variety of different energy storage systems which are chosen depending on the field of application. Among the available stationary power sources, rechargeable lithium-ion batteries substantially impact the areas of energy storage, energy efficiency and advanced vehicles. These batteries are the most advanced and true portable power sources combined with advantages of small size, reduced weight, longer operating time and easy operation. Such batteries can be recharged anytime (no memory effect) regardless of the charge current/voltage and they are reliable and safe. These unique features render their application in a variety of consumer electronic gadgets such as mobile phones, digital cameras, personal digital assistants (PDAs), portable CD players and palmtop computers. The high-end applications of this smart power source are projected for Hybrid Electric Vehicles (HEVs) as potential source of propulsion.

The evolution of rechargeable lithium batteries since their inception by Sony Corporation (Reimers & Dahn, 1992) has led to the development of new electrode materials (Kobayashi et al., 2000; Gaubicher, et al., 2000; Zhang et al., 2009; Zhu et al., 2008) for their effective operation in the real ICT environment. Among the new materials search for Li-ion batteries, polyanion compounds are growing into incredible dimensions owing to their intriguing properties (Manthiram & Goodenough, 1989; Huang et al., 2001; Yang et al., 2002; Chung et al., 2002).

In this chapter, we present a systematic study of a group of new polyanion materials, namely, lithium-rich $[Li_2M_2(MoO_4)_3]$ and lithium-free $[Li_xM_2(MoO_4)_3]$ (M= Ni, Co) phases of transition metal oxides having NASICON open framework structure. A simple and efficient approach to prepare the materials and a combination of characterization techniques to reveal the physical and electrochemical properties of these materials are covered at length. A separate section is devoted to a nano-composite approach wherein conductivity enhancement of all the four materials is enlightened. We begin this chapter with a brief

description of polyanion materials in general in general and NASICON structure type materials in particular.

2. Background

2.1 Polyanions

Despite the long known history of polyanion compounds as fast ion conductors or solid electrolytes (Goodenough et al., 1976; Hong, 1976), they relatively comprise a new category of electrode materials in recent times. The remarkable properties of these materials in tailor made compositions may lead them for use as electrodes in next generation lithium-ion batteries.

2.2 Types of polyanion compounds

Polyanion compounds incorporate NASICON structure type $Li_xM'_2(XO_4)_3$ and olivine type $Li_xM''XO_4$ materials.

NASICON materials are a family of compounds with $M'_2(XO_4)_3$ [M′ = Ni, Co, Mn, Fe, Ti or V and X = S, P, As, Mo or W] networks in which $M'O_6$ octahedra share all their corners with XO_4 tetrahedra, and XO_4 tetrahedra, share all their corners with $M'O_6$ octahedra (Manthiram & Goodenough, 1987). The interstitials and conduction channels are generated along the c-axis direction, in which alkali metal ions occupy the interstitial sites. Consequently, the alkali metal ions can move easily along the conduction channels (Wang et al., 2003). The $M'_2(XO_4)_3$ host framework is chemically versatile and it could be stabilized with a variety of transition metal cations M′ having an accessible redox potential and XO_4 polyanions. Such framework oxides were known to undergo a topotactic insertion/ extraction of a mobile atom due to the availability of an open three-dimensional framework (Nadiri et al., 1984; Reiff et al., 1986; Torardi & Prince, 1986) and hence are considered as electrode materials for rechargeable lithium batteries (Padhi et al., 1997).

The $Li_xM''XO_4$ [M′ = Fe, Co, Mn or Ni and X = P, Mo, W or S] olivine structure has Li and M′′ atoms in octahedral sites and X atoms in tetrahedral sites of a hexagonal close-packed (hcp) oxygen array. With Li in continuous chain of edge-shared octahedra of alternate planes, a reversible extraction/insertion of lithium from/into these chains would appear to be analogous to the two-dimensional extraction or insertion of lithium in the $LiMO_2$ oxides (Padhi et al, 1997).

2.3 NASICON type materials for energy storage– A brief history

Over the past, a number of researchers widely investigated NASICON structure type materials to facilitate exploitation in Li-ion batteries.

As early in 1984, lithium insertion/extraction properties of NASICON type polyanion compound, $Fe_2(MoO_4)_3$ was first reported by Nadiri et al. (1984). The compound was found to crystallize in monoclinic structure and it contains iron ions exclusively in 3+ state. It was shown that lithium could be inserted either chemically or electrochemically into the framework $Fe_2(MoO_4)_3$ with the concurrent reduction of ferric to ferrous ions (Fe^{3+} to Fe^{2+}) to form $Li_xFe_2(MoO_4)_3$ (x=2). The latter compound was found to crystallize in an orthorhombic structure (Nadiri et al., 1984; Reiff et al., 1986).

Pure $Fe_2(WO_4)_3$, isostructural with room temperature $Fe_2(MoO_4)_3$ (Harrison et al., 1985) could also reversibly insert lithium either chemically or electrochemically to form $Li_2Fe_2(WO_4)_3$ similar to $Li_2Fe_2(MoO_4)_3$. It was demonstrated that the voltage versus lithium content x for a $Li/Li_xFe_2(MoO_4)_3$ cell gives rise to a plateau in the 3 V region for $0<x<1.7$ substantiating the two-phase character of this compositional range. There was a sharp drop in V_{oc} at x=2.0 due to lattice disproportionation leading to irreversibility (Manthiram & Goodenough, 1987). This finding during the initial stage of exploring polyanions, in fact, formed a footing to further investigating this kind of compounds as electrode materials for lithium battery application.

Iron sulphate based positive electrodes, $Fe_2(SO_4)_3$ were shown to exist in hexagonal NASICON structure (Goodenough et al., 1976) as well as in a related monoclinic form (Long et al., 1979). Electrochemical insertion of lithium into both structure types was demonstrated by a two phase process in the range $0<x<2$ of nominal $Li_xFe_2(SO_4)_3$ giving rise to a flat voltage profile at 3.6 V versus a lithium metal anode. The end phase $Li_2Fe_2(SO_4)_3$ was confirmed to be orthorhombic. A difference of 600 mV in OCV observed between the sulfate and corresponding molybdate or tungstate systems is due to the influence of the counter cation on the Fe^{3+}/Fe^{2+} redox couple (Manthiram & Goodenough, 1989; Nanjundasamy et al., 1996). For x>2, there is a drop in voltage from the open circuit voltage (OCV). The performance of the material vitally depended on the initial phase of $Fe_2(SO_4)_3$ framework. The rhombohedral starting material retained modest capacity at lower current densities even after 80 cycles whereas the monoclinic $Fe_2(SO_4)_3$ showed a faster capacity fade (Okada et al, unpublished results). The overall performance of the hexagonal phase was shown to be superior to the monoclinic phase (Bykov et al., 1990).

Nanjundasamy et al. (1996) investigated the use of titanium, vanadium in the cation site and $(PO_4)^{3-}$ in the anion site to buffer $Fe_2(SO_4)_3$ against too large a drop in voltage and found that changing the polyanion group from $(SO_4)^{2-}$ to $(PO_4)^{3-}$ shifts the position of the redox couple from 3.2 eV to 2.5 eV for Ti^{4+}/Ti^{3+}, 2.5 eV to 1.7 eV for V^{3+}/V^{2+} and 3.6 eV to 2.8 eV for Fe^{3+}/Fe^{2+} below the Fermi level of lithium due to the smaller polarization of O^{2-} toward P^{5+} than toward S^{6+}. Each of these materials delivered a specific capacity of about 100 mAh/g between 2.0 and 4.2 V for a reversible insertion of two Li^+ per formula unit.

Padhi et al., (1998) noticed that the lithium insertion is accomplished by means of a single-phase reaction by tuning the position of the redox couple in the NASICON framework structures by anionic substitution as well. Electrochemical insertion of additional lithium into rhombohedral $Li_{1+x}Fe_2(SO_4)_2(PO_4)$ with NASICON framework over the range $0 \leq x \leq 1.5$ was found to be a reversible solid solution reaction within the hexagonal structure. The position of the redox couple Fe^{3+}/Fe^{2+} is located at 3.3 – 3.4 eV below the Fermi energy of lithium and this material delivered a reversible capacity of 110 mAh/g relative to a Li-metal anode.

In an independent analysis, $Li_3Fe(MoO_4)_3$ was shown to reversibly insert lithium down to 2 V akin to $Fe_2(MoO_4)_3$ (Dompablo et al., 2006). They conducted a comprehensive phase diagram study for $Li_{3+x}Fe(MoO_4)_3$ which revealed preservation of the structural framework for low lithium contents ($0<x<1$) ensuring good cyclability of the material in lithium cells, however, with a slight change of the cell volume (0.85%) (Vega et al., 2005).

Most of the above mentioned framework materials tend to operate in the low voltage range, which is not impressive for high voltage (>4 V) positive electrode application.

In the field of high voltage (>4 V) positive electrode materials, phosphate structures operating on the V^{3+}/V^{4+} receive increasing interest in view of the fact that the redox

potential and energy densities of phosphate-based polyanion compounds are as good as the current technologies (Padhi et al., 1997; Nanjundasamy et al., 1996) with good cycling properties at high scan rates (Nazar et al., 2002). Barker et al. (2003) explored $LiVFPO_4$ and Davies et al. (1994) investigated vanadium phosphate glasses as cathodes for Li-ion cells. A number of phases of $Li_3V_2(PO_4)_3$ were also studied as novel cathodes for Li-ion batteries. The removal of lithium is facile in such materials as they are structurally alike the NASICON family of materials. Amongst is the thermodynamically stable monoclinic form of $Li_3V_2(PO_4)_3$ which is isostructural to several other $Li_3M_2(PO_4)_3$ (M = Sc, Fe or Cr) materials (Huang et al., 2002; Yin et al., 2003). All three Li-ions may be reversibly removed from $Li_3V_2(PO_4)_3$ over two-phase electrochemical plateaus yielding a theoretical capacity of 197 mAh/g which is the highest for all phosphates reported so far. Nevertheless, electrochemical measurements showed that the material sustains reversibility when extraction/insertion is confined to two Li-ions with a reversible capacity of 130 mAh/g and the extraction of the third lithium is kinetically hindered and involves a significant over voltage (Saidi et al., 2002; 2003). Rhombohedral form of $Li_3V_2(PO_4)_3$ exhibits similar electrochemical characteristics as for the charge extraction, but reinsertion is limited to 1.3 lithium corresponding to 90 mAh/g of capacity (Gaubicher et al., 2000; Morcrette et al., 2003). Later, it was found that Zr substitution in orthorhombic $Li_3V_2(PO_4)_3$ phase enhances the electrochemical performance in terms of the discharge capacity and disappearance of the two-plateau boundary in the charge-discharge curves (Sato et al., 2000).
In 4 V class NASICON structure type materials explored to date, $Li_3Fe_2(PO_4)_3$ exits in monoclinic and rhombohedral forms. The $Fe_2(PO_4)_3$ framework remains intact under lithium extraction/insertion (Masquelier et al., 1996) occurring in a single continuous step giving rise to an initial discharge capacity of 115 mAh/g (Masquelier et al., 1998). This behavior slightly differs from $Li_3V_2(PO_4)_3$ where partial dissolution of vanadium takes place in deep reduction and at deep oxidation (Patoux et al., 2003).

3. Experimental processes

A succinct description of various experimental methods followed in the present study is presented in this section. In addition, the experimental procedure employed is highlighted wherever required.

3.1 Synthesis of open framework structured materials-Soft combustion technique

The soft-combustion technique offers several advantages over conventional high temperature and other low temperature methods. Materials prepared via the solid-state route contain two-phase mixtures due to the inhomogeneity caused by physical mixing of the raw materials. The particle morphology is often irregular and particle size is very large. On the other hand, the soft-combustion method, which is a low temperature preparative process is not time consuming and obviously well suited for bulk synthesis. Moreover, materials can be prepared with a single-phase structure and there is no impurity as second phase. Uniform particle morphology is an added advantage of this technique.
To prepare the polyanion transition metal oxides in the present study, starting materials such as lithium nitrate and hexa-ammonium heptamolybdate along with nitrate of the transition metals, Ni and Co were dissolved in deionized water in the appropriate molar ratio. The mixed solution was then added to an aqueous solution of glycine that acted as a

soft-combustion fuel. The quantity of glycine was optimized as twice the molar fraction of the starting materials. The solution was heated to boiling at 100 ^{o}C. A paste like substance formed was further heated at 250 ^{o}C to decompose the dried substance namely, the precursor. During the process of decomposition, the reaction was ignited by the combustible nature of glycine and gases like N_2O, NH_3 etc. were liberated leading to dry powders namely, the as-prepared material.

3.2 Characterization techniques employed

a. Physical characterization

As for the new materials prepared via the soft-combustion method, we employed physical characterization techniques such as X-ray diffraction (XRD) and scanning electron microscopy (SEM) analysis so as to find the crystallographic properties of the annealed samples and to observe the particle size distribution, shape and morphology features of the synthesized powder samples.

JEOL (model JDX 8030) and Rigaku (RINT-2500 V, 50 kV/100 mA, Rigaku Co. Ltd) X-ray diffractometers were used to record the diffractograms of the polyanion materials using CuKα radiation (λ=1.5406 Å). Peak locations and intensities were determined by a least-squares method and a refinement analysis, FullProof Suite, WinPLOTR 2004 was used to calculate the unit cells. We used Cambridge Instruments (Stereo scan S200) to collect SEM data for the family of new polyanion compounds. JEOL (JSM 6301F) was employed to study the high resolution images.

b. Electrochemical characterization

In order to elucidate the mechanism of lithium extraction/insertion in the new materials, and to generate kinetic and interfacial information, electrochemical studies were made, the details of which are given below.

i. Cyclic voltammetry (CV) measurements - Constant voltage cycling:

Cyclic voltammetry is an important and most commonly used electrochemical technique to characterize any electrochemical system. We examined the new materials by means of cyclic voltammetry studies and obtained information regarding the reversible nature (redox properties) of the materials and structural integrity during prolonged cycling with a view to validate the suitability of the materials for Li-ion batteries. We performed the Slow Scan Cyclic Voltammetry (SSCV) tests using Basic electrochemical system (BAS, Perkin Elmer, PARC model, USA) equipped with PowerCV® software.

ii. Galvanostatic (constant current) charge/discharge test:

Although potentiostatic experiments are a key in the sense that they readily divulge the reversibility of an electrode material, there are some applications for which a galvanostat is advantageous. The number of Li-ions participating in the redox reaction and hence the discharge capacity of the electrode material expressed in mAh/g is made known through Galvanostatic cycling test. In the present study, Arbin battery tester (Arbin instruments BT2000, USA) (8-channel unit) equipped with MITSPRO software was used to conduct the galvanostatic charge/discharge cycle tests.

iii. Electrode preparation and cell fabrication:

Teflon made two-electrode cells with SS current collectors were used to perform the electrochemical tests. Composite cathodes (positive electrodes) were prepared by mixing the electrode-active material [powders of polyanion materials], acetylene black and PTFE binder in a weight ratio of 80:15:5. The mixture was kneaded in agate type mortar and

pestle, rolled into thin sheets of around 100 ③m thick, and cut into circular electrodes of 3.14 cm^2 area and pressed onto an aluminum expanded grid mesh current collector. Test cells were composed of cathode (working electrode), a thin lithium foil (FMC, USA) as both counter and reference electrode and a microporous (Celgard® 3501 polypropylene) membrane soaked in a standard non-aqueous Li^+ electrolyte mixture solution (1M $LiPF_6$ in EC+DMC) (Merck LP 30) as a separator. The test cells were fabricated inside a glove box filled with high purity (99.999%) argon.

4. Results and discussion

4.1 Structure of $Li_2M_2(MoO_4)_3$

The crystal structure of $Li_2M_2(MoO_4)_3$ was determined using the CrystalDesigner® software. Figure 1 shows the polyhedral crystal structure of $Li_2M_2(MoO_4)_3$. The determination of the crystal structure revealed a three-dimensional framework consisting of metal-oxygen octahedra and trigonal prisms (where Li and M reside) which are interconnected by MoO_4 tetrahedra. The hexagonal motif of Mo tetrahedra around M octahedra joined by their faces is clearly seen in Fig. 1. Lithium atoms may occupy sites between or within the layers. The open framework allowed Li^+ ions to easily move in and out of the structure. Similar structures were already reported for analogous polyanion materials such as orthorhombic $Li_2Fe_2(MO_4)_3$ [M = Mo or W] (Manthiram & Goodenough, 1987).

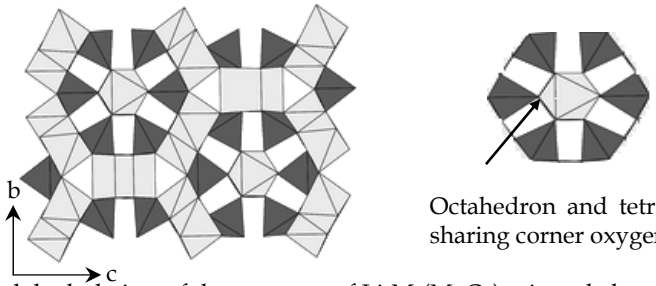

Fig. 1. Polyhedral view of the structure of $Li_2M_2(MoO_4)_3$ viewed along the (100) plane (Prabaharan et al., 2004).

4.2 Phase analysis

The phase purity of all the four materials was examined by means of XRD. In order to optimise the phase purity, we annealed the samples at different temperatures with a fixed soak time of 4h.

a. Lithium-rich phase of metal molybdates:

The XRD patterns of $Li_2Ni(MoO_4)_3$ recorded for the product annealed at 500°C exhibited some impurity peaks which were found to disappear upon annealing at 600°C and 700°C. In the case of the product annealed at 600°C, it was observed that the XRD peak positions are in good agreement with the preliminary crystallographic data previously reported (JCPDS #70-0452) indicating the formation of a well crystalline single-phase structure. So, the product annealed at 600°C was taken for further examination.

$Li_2Ni_2(MoO_4)_3$ was indexed in an orthorhombic structure with space group Pmcn. We used a refinement program (ICSD using POWD-12++) (Ozima et al., 1977) to calculate the cell

parameters of $Li_2Ni_2(MoO_4)_3$ and found the values as follows: a = 10.424(4) A°, b = 17.525(1) A° and c = 5.074(3) A°. It is to be mentioned here that no crystal structure information is available for $Li_2Ni_2(MoO_4)_3$ as for as we know except for the one available in JCPDS Ref. #70-0452. However, the latter pattern is non-indexed.

Although a single-phase structure with desired phase purity was formed at 600ºC/4 h/air, lithium could not be extracted from $Li_2Ni_2(MoO_4)_3$ during electrochemical charge owing to the difficulty in stabilizing nickel at a fixed valence state. It was suggested that a controlled oxygen atmosphere is essential during annealing of $LiNiO_2$ in order to stabilize nickel (Moshtev et al., 1995; Hirano et al., 1995). Accordingly, the as-prepared product of $Li_2Ni_2(MoO_4)_3$ was subjected to annealing at 600ºC/4h in the presence of oxygen atmosphere (90 ml/min). The XRD pattern of this product was recorded and compared with the one obtained under the same annealing conditions in ambient air.

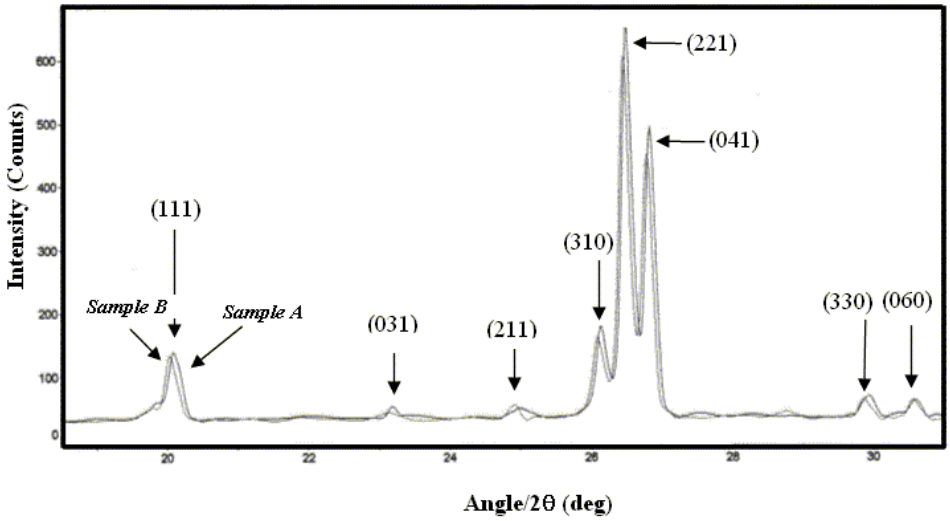

Fig. 2. Comparison of the peak positions of the diffractograms of as-prepared samples annealed in ambient air (sample A) and annealed in oxygen atmosphere (sample B) (Prabaharan et al., 2004).

Fig. 2 illustrates an expanded view of the differences in the peak positions of the chosen region with high intensity peaks (19°-31°/2θ angle) between the samples annealed in ambient air (sample A) and in oxygen atmosphere (sample B). A closer look at the diffractograms clearly reveals a slight but noticeable peak shift toward low 2θ regions for the sample B with respect to sample A, which is obviously a result of the heat treatment for the sample B in the presence of oxygen atmosphere. The peak shift is an indication of the volume change of the crystal lattice, which would probably facilitate the easy Li^+ extraction/insertion kinetics thereby improving the rate capability and discharge capacity compared to the one annealed in ambient air. The XRD pattern of $Li_2Co_2(MoO_4)_3$ is very much similar to that of $Li_2Ni_2(MoO_4)_3$. The disappearance of impurity peaks at a higher annealing temperature is well seen in figure 3. In addition, the peaks are refined and become sharper resulting in decreased crystallite size of the product. This is one of the favorable attributes for the effective utilization of $Li_2Co_2(MoO_4)_3$ positive-electrode active

powders. In the case of the product annealed at 600 ˚C, it was observed that the XRD peak positions are in good agreement with the crystallographic data previously reported (PDF # 31-0716), indicating the formation of a well crystalline single-phase structure.
$Li_2Co_2(MoO_4)_3$ was indexed in an orthorhombic structure with a space group Pnma. The refinement program used for $Li_2Ni_2(MoO_4)_3$ was used in this case as well and the lattice parameters were calculated to be a = 5.086(1) Å, b = 10.484(2) Å and c = 17.606(2) Å.

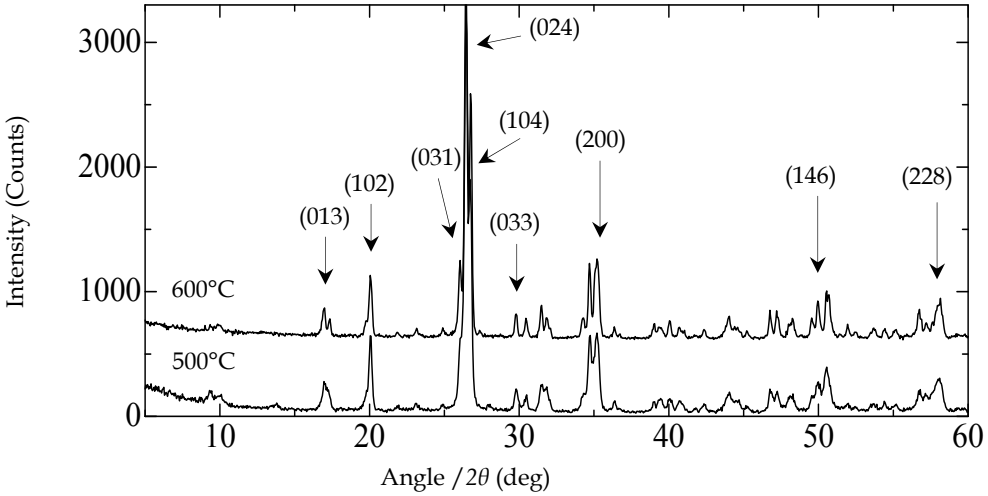

Fig. 3. XRD patterns of $Li_2Co_2(MoO_4)_3$ at (a) 500°C; (b) 600°C (Prabaharan et al., 2004).

b. Lithium-free phase of metal molybdates:
It is known from the XRD patterns of lithium-rich phases $Li_2M_2(MoO_4)_3$, that the appropriate annealing temperature to obtain single-phase polyanion materials is 600°C. Hence, the as-prepared product of $Ni_2(MoO_4)_3$ was annealed at 600 °C in the presence of oxygen atmosphere for two different annealing times, 4h and 7h to verify the effect of annealing time on the crystalline material.
Figure 4 presents the X-ray diffraction pattern of $Ni_2(MoO_4)_3$ annealed at 600°C for 4 h and 7 h in an oxygen atmosphere (90 ml/min). It is clear from the diffractograms that the peaks are alike in terms of peak position, sharpens of the peaks and intensity for the two samples indicating the formation of well crystalline structure. As the diffraction pattern is similar for both the samples, sample A was chosen for further investigation. The peaks were indexed using a least-squares refinement method.

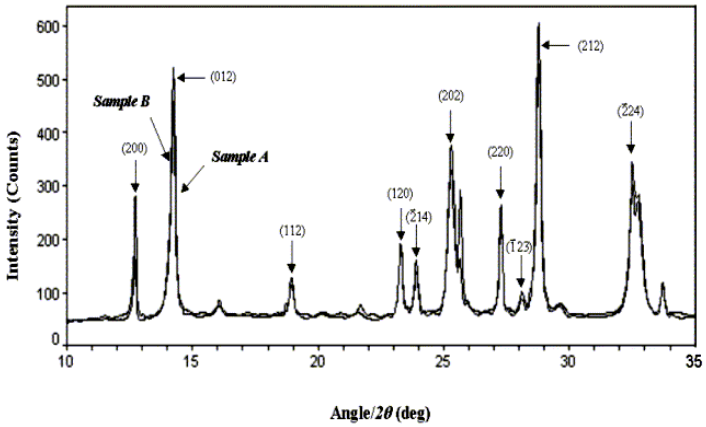

Fig. 4. X-ray diffractograms of $Ni_2(MoO_4)_3$ annealed at 600°C under O_2 purge (90 ml/min); Sample A - 600°C/4 h; sample B - 600°C/7h (Prabaharan et al., 2004).

The diffractograms of $Co_2(MoO_4)_3$ corresponding to 600°C and 700°C annealing temperature for 4 h signify the growth of peaks as shown in figure below (Fig. 5).
The peaks were indexed for the first time using a least-squares refinement method. $Co_2(MoO_4)_3$ was indexed in monoclinic structure with space group with P2/m. The lattice parameters were determined using a refinement program (FullProof Suite, WINPLOTR 2004) and calculated to be: a = 14.280(9) Å, b = 3.382(8) Å, c = 10.5571 Å and β = 117.9728˚.

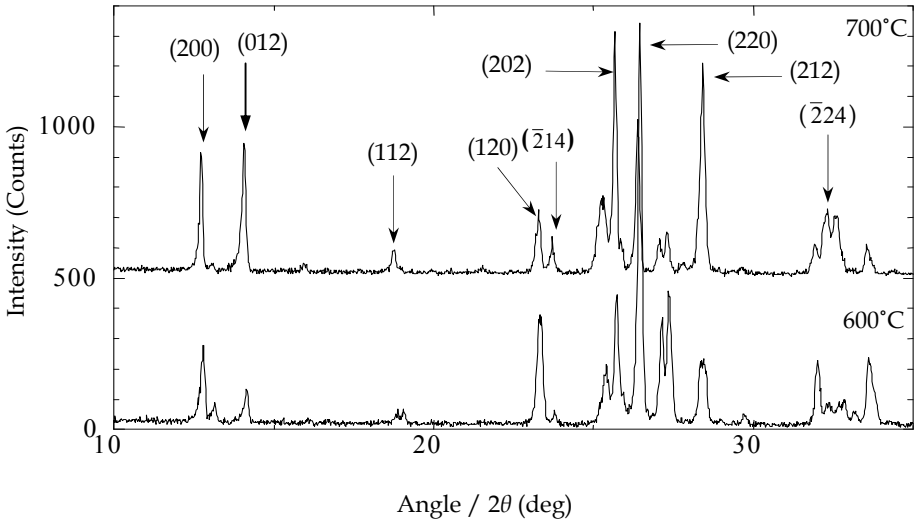

Fig. 5. X-ray diffraction patterns of $Co_2(MoO_4)_3$ annealed at 600 °C and 700 °C (Prabaharan et al., 2004).

4.3 SEM analysis

SEM images were recorded for the synthesized polycrystalline powders annealed at 600°C for 4h and are exhibited in Fig. 6. As for the lithium-rich phases ($Li_2Ni_2(MoO_4)_3$ & $Li_2Co_2(MoO_4)_3$, SEM reveals the formation fiber-like grains with controlled grain growth and morphology (Fig. 7a & b). In both cases the particles are loosely agglomerated with the average size within the submicrometre range.

As for as the morphology is concerned, $Ni_2(MoO_4)_3$ as well as $Co_2(MoO_4)_3$ powders exhibit uniform and ultrafine spherical grains (Fig. 7 c & d) with nearly uniform particle size. The inset in Fig. 7c shows the SEM picture recorded at high magnification to unveil the actual grain size distribution. Consequently, the micrograph (inset) demonstrates nanosized spherical grains with a single grain size of ~100nm. From the nanostructure morphology of $Co_2(MoO_4)_3$ as depicted in Fig. 7d, it is readily observed that $Co_2(MoO_4)_3$ powders contain uniform spherical grains of much reduced size (20 nm) when compared to $Ni_2(MoO_4)_3$.

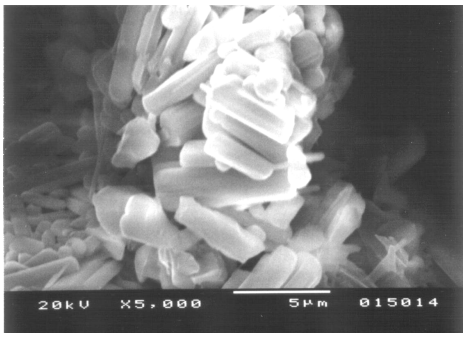

6a. $Li_2Ni_2(MoO_4)_3$

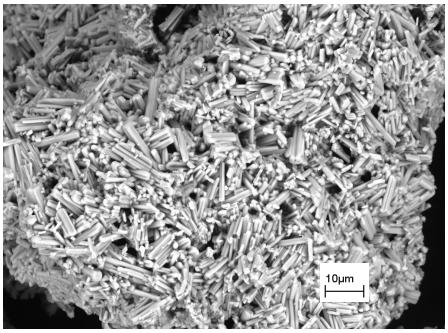

6b. $Li_2Co_2(MoO_4)_3$

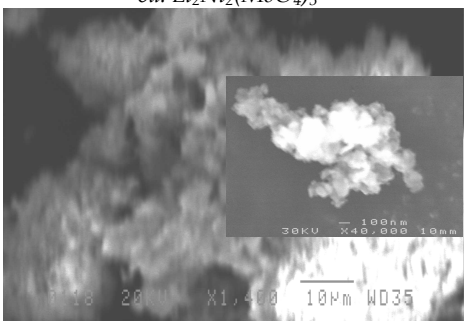

6c. $Ni_2(MoO_4)_3$

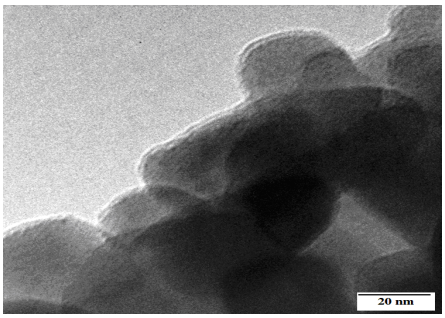

6d. $Co_2(MoO_4)_3$

Fig. 6 (a, b & c). SEM images; d. TEM image. (Prabaharan et al., 2004, 2006, 2008).

4.4 Electrochemical studies

a. Cyclic voltammetry (CV) measurements

In order to elucidate the electrochemical reversible nature of the materials taken for the present investigation, we carried out cyclic voltammetry tests on $Li/Li_2M_2(MoO_4)_3$ and $Li/Li_xM_2(MoO_4)_3$ half cells at a low scan rate (0.1 mV/s). The cells were first charged to extract lithium from the host materials and then discharged to insert lithium in the host structures. We discovered that all the four materials possess electrochemical reversibility

with regard to Li^+ extraction/insertion. Accordingly, Fig. 7 presents the slow scan cyclic voltammograms of $Li_2M_2(MoO_4)_3$ composite electrodes vs. Li/Li^+ cycled between 4.9 V and 1.5 V. It is clearly seen from the CV profiles that $Li_2M_2(MoO_4)_3$ polyanion materials reveal a systematic evidence for the electrochemical reversibility through the oxidation and reduction peaks corresponding to the two transition metal ions, M^{2+} [M = Ni, Co] and Mo^{6+}. As for the electrochemical reversibility of $Li_2M_2(MoO_4)_3$ vs. Li/Li^+, during charge (anodic scan), we observed the first oxidation of Ni^{2+}/Ni^{3+} at 4.4 V whilst the oxidation of Co^{2+}/Co^{3+} was found to occur at 4.3 V. Following the charging process, during discharge, (cathodic scan), we were able to notice a single peak at 3.2 V corresponding to Ni^{3+}/Ni^{2+} reduction, and its analogous counterpart, Co^{3+} was found to reduce to Co^{2+} at 3.1 V. The shift in the redox potential of M^{3+}/M^{2+} is correlated to the polyanion $(MoO_4)^{2-}$ in the host framework structure. In fact, we emphasized this point in some of our publication (Prabaharan et al., 2004) as reported by Nanjundaswamy et al. (1996), who studied the effect of NASICON-related framework compounds such as $M_2(SO_4)_3$ and $Li_xM_2(PO_4)_3$

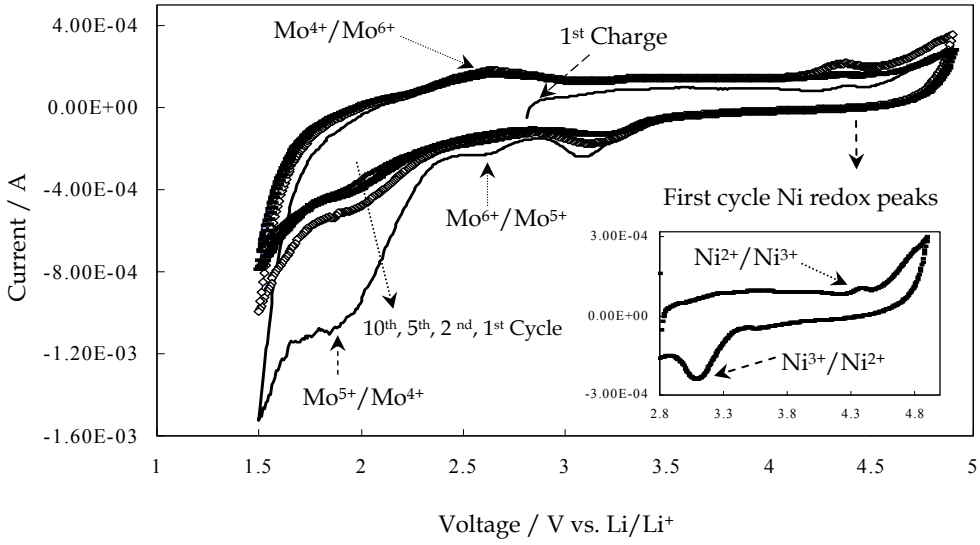

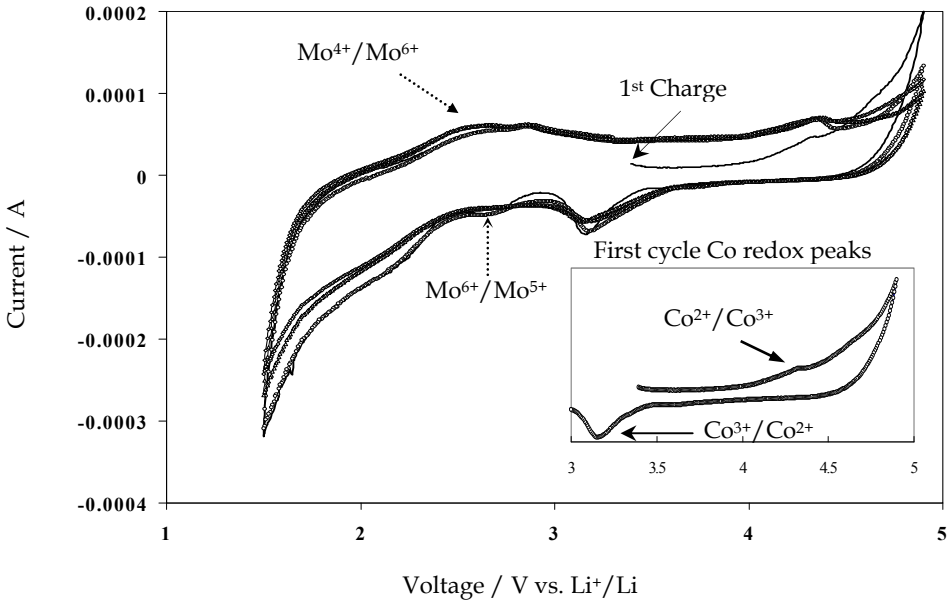

Fig. 7. Slow scan cyclic voltammetry of $Li_2M_2(MoO_4)_3$ vs. Li/Li^+. Scan rate: 0.1 mV/s; V_{max}: 4.9 V (oxidation); V_{min}: 1.5V (reduction); Inset: First cycle Ni/Co redox peaks (Prabaharan et al., 2004).

(M= transition metal) in the context of how a change in the polyanion group shifts the redox potentials of the M cations and the influence on the Li^+ insertion rate and cyclability of end member phase transitions of the lithiated and delithiated phases.

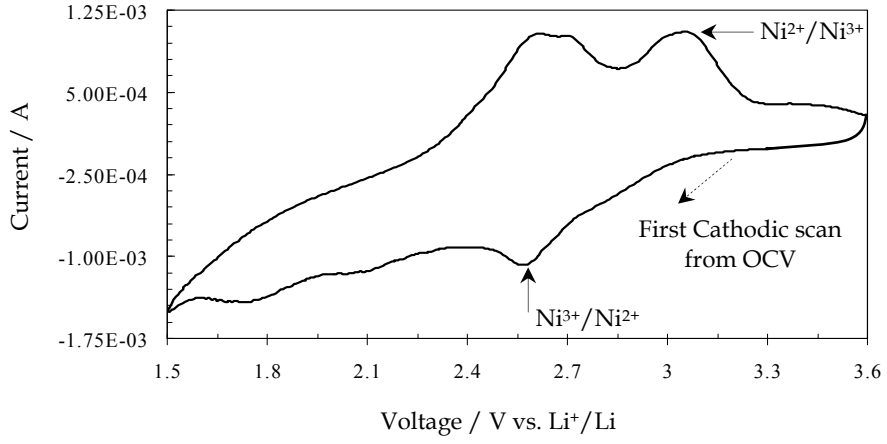

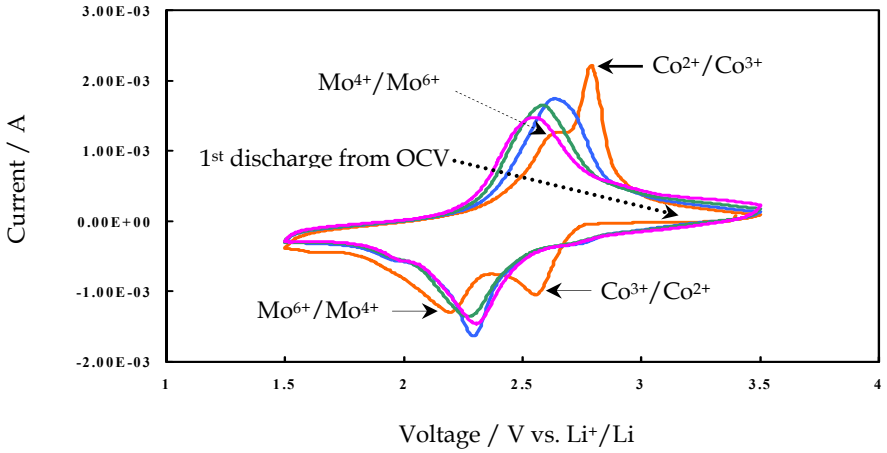

Fig. 8. Slow scan cyclic voltammetry of $Li_xM_2(MoO_4)_3$ vs. Li/Li^+. Scan rate: 0.1 mV/s; V_{max}: 3.6/3.5 V (oxidation); V_{min}: 1.5V (reduction). (Prabaharan et al., 2004, 2006).

During the continuation of the reduction process down to 1.5 V, two peaks were noticed at 2.6 and 1.9 V in the case of $Li_2Ni_2(MoO_4)_3$ and at 2.6 and 2 V for $Li_2Co_2(MoO_4)_3$ indicating the reduction of Mo^{6+} to Mo^{5+} and Mo^{4+}. During successive cycling, these two peaks were found to merge into a single broad peak in both cases, implying the slow and steady dynamics of Li^+ into the active material. Upon further cycling, we were able to observe a broad anodic peak at 2.6 V representing the Mo oxidation, followed by a high voltage peak at 4.3 V indicating the oxidation of M^{2+} cations back to 3+ state.

The slow scan cyclic voltammograms of $Li_xM_2(MoO_4)_3$ composite electrodes vs. Li/Li^+ cycled between 1.5 V and 3.6 V [for $Li_xNi_2(MoO_4)_3$] and between 1.5 V and 3.5 V [for $Li_xCo_2(MoO_4)_3$] are shown in Fig. 8. The cells were first discharged to insert lithium in $M_2(MoO_4)_3$ framework structure and then charged to extract lithium. The CV profiles demonstrate the electrochemical reversibility of the material and exhibits the reduction and oxidation peaks corresponding to the two transition metal ions M^{3+} and Mo^{6+}.

During the first discharge from OCV, the reduction of M^{3+}/M^{2+} was observed at 2.6 V and as the reduction process continues down to 1.5 V, two other broad peaks were observed at 2.1 V and 1.7 V in the case of $Li_xNi_2(MoO_4)_3$ due to the reduction of Mo^{6+} (to its lower oxidation states). On the other hand, a single reduction peak was observed at 2.2 V for $Li_xCo_2(MoO_4)_3$ indicating two-electron transfer during Mo^{6+} reduction. Upon the first charge after discharge, in lithium-free nickel molybdate, oxidation of Mo back to its higher oxidation state (6+ state) and Ni^{2+}/Ni^{3+} transitions were noticed at 2.6 V, 2.7 V and 3.1 V respectively. Whereas, in lithium-free cobalt molybdate Mo^{4+}/Mo^{6+} transition was observed in a single step at 2.65 V which was followed by oxidation of Co^{2+} to Co^{3+} at 2.8 V. These observations are similar to $Li_2M_2(MoO_4)_3$ except for a slight change in the position of the peaks and peak height. The same trend was observed during extended cycling.

Furthermore, in all the four cases, oxidation and reduction of M and Mo ions (cations and counter cations) were clearly observed during prolonged cycling. The excellent electrochemical reversibility of the new materials as evidenced from the CV profiles is an indication of the appropriateness of the new materials for application in rechargeable

lithium batteries. With a view to strengthen our findings from CV studies, we performed charge/discharge tests galvanostatically, the details of which are given in the next section.

b. Galvanostatic charge/discharge test

We conducted charge/discharge tests on the $Li_2M_2(MoO_4)_3$/Li half-cells between 4.9 and 1.5 V at low current densities: 2.5 mA/g (charge) and 1.25 mA/g (discharge). $Li_xM_2(MoO_4)_3$/Li half-cells were subjected to discharge/charge test against lithium in half-cells between 1.5 and 3.5 V at low current densities: 2.5 mA/g (discharge) and 10 mA/g (charge). From the galvanostatic charge/discharge tests conducted for the first 20 cycles, we calculated the number of Li-ions participated in the electrochemical redox reactions from the amount of electrical charges spent as a function of elapsed time on the tests and hence the discharge capacity of the polyanion electrode materials.

Fig. 9 represents the galvanostatic multiple charge-discharge curves of the half-cell $Li_2Ni_2(MoO_4)_3$/Li. It was observed that the first charge curve from OCV (2.8 V) exhibit a smooth plateau with an onset at about 4.6 V, which extends steadily with an increasing trend up to 4.9 V vs. Li/Li^+. During the first charge process of lithium extraction, one Li^+ per formula could be extracted with a charge capacity of 45 mAh/g as shown in Fig. 9. During the first discharge, 2.6 Li^+ per formula unit could be reversibly inserted down to 1.5 V with a discharge capacity of ~ 115 mAh/g. The transitions of $Ni^{3+}$to Ni^{2+} and Mo^{6+} to its lower oxidation states are visible as two-step discernible plateaus during the first discharge. These findings are consistent with the first cycle reduction peaks obtained from SSCV studies.

Even though the compound exhibited a good high voltage charge profile during the first lithium extraction, the discharge profile demonstrated poor reduction kinetics during the beginning of discharge (insertion) between 4.9 and 3.0 V. Besides this, the electrochemical insertion was limited to 0.25 lithium per formula unit between 4.9 and 2.5 V vs. Li/Li^+. This poor rate kinetics is strongly attributed to the inherent structural limitation as well as poor electronic conductivity, which is common for polyanion materials reported so far (Goodenough et al., 1997; Tarascon and Armand, 2001). Moreover, once Mo^{6+} in tetrahedral site is reduced to Mo^{5+} or Mo^{4+}, it may be difficult to oxidize it back keeping the same crystal structure, and this partly explains the poor cyclability of $Li_2Ni_2(MoO_4)_3$. It was observed that there is no change in the shape of the charge and discharge profiles after the first cycle indicating the structural stability of the host material during repeated cycling. However, there is a continuous decreasing trend in terms of the amount of Li^+ inserted into $Li_2Ni_2(MoO_4)_3$ as the cycle number increases for obvious reasons. This leads to a considerable decline in the discharge capacity of the material.

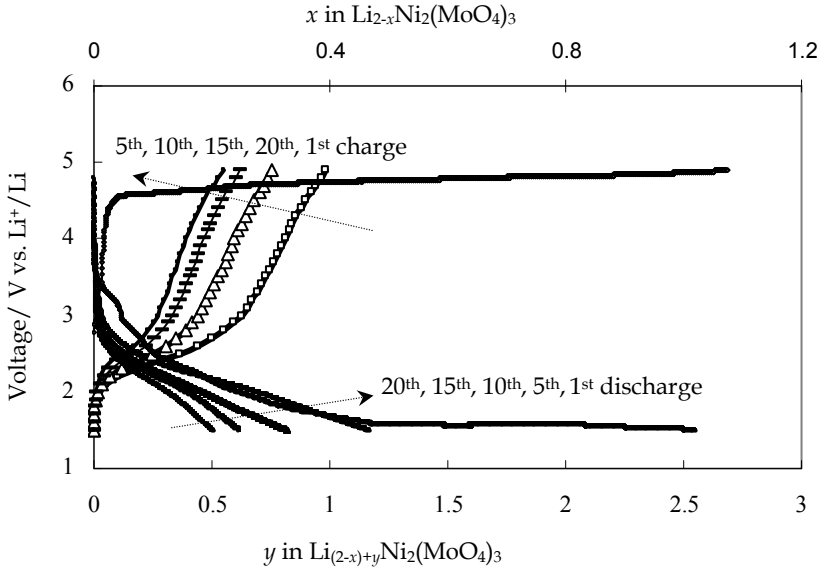

Fig. 9. Multiple charge/discharge curves of $Li_2Ni_2(MoO_4)_3$//Li cell between 4.9 and 1.5 V

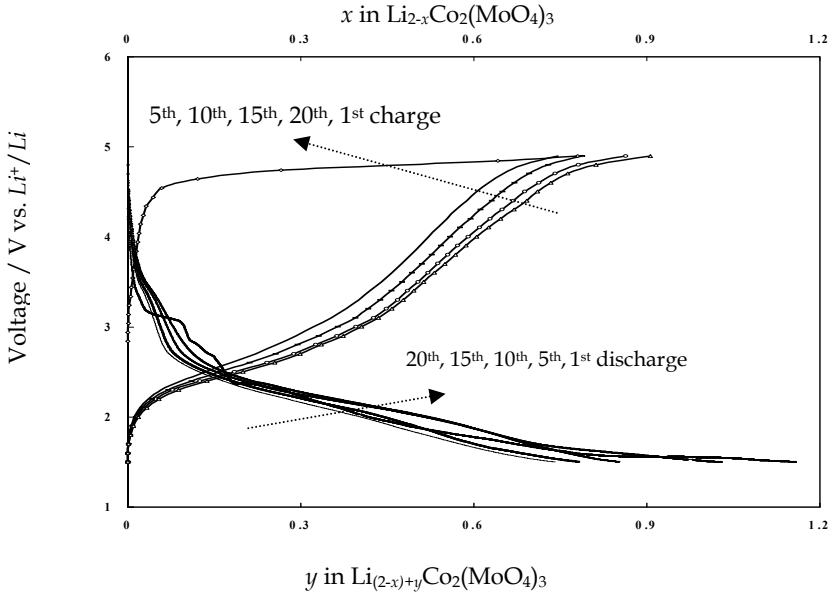

Fig. 10. Multiple charge/discharge curves of $Li_2Co_2(MoO_4)_3$//Li cell between 4.9 and 1.5 V (Prabaharan et al., 2004).

The galvanostatic multiple charge-discharge curves of the half-cell $Li_2Co_2(MoO_4)_3$/Li are shown in the following figure (Fig. 10). It is clearly seen from Fig. 10 that the

charge/discharge profiles are comparable to Fig. 9 with regard to shape, oxidation and reduction of Co^{2+} and Mo^{6+} although a slight difference was noticed in the first charge and discharge capacity values; first lithium extraction process corresponds to 0.8 Li^+ per formula leading to a charge capacity of 35 mAh/g and 1.2 Li^+ per formula unit could be reversibly inserted down to 1.5 V with a discharge capacity of ~ 55 mAh/g. Nevertheless, the performance of the cobalt-containing polyanion compound was found to be better with regard to extended cycling than its analogous nickel counterpart despite their similar structural environment. Although the extended cycling characteristics are rather better, still the material suffers from poor rate kinetics for the reasons explained above.

The galvanostatic multiple discharge-charge curves of $Ni_2(MoO_4)_3$/Li half-cells are shown in Fig. 11. It was observed that the first discharge curve from OCV (3.4 V) exhibited a sloping plateau corresponding to the reduction of nickel followed by a perceptible plateau due to the reduction of molybdenum. These observations are in good agreement with the reduction peaks found in CV studies (Fig. 8). During the first discharge process of lithium insertion down to 1.5 V, 3.6 Li^+ could be inserted which amounts to a discharge capacity of ~ 170 mAh/g. During the first charge (extraction) after discharge, 3 Li^+ per formula unit could be extracted up to 3.5 V with a charge capacity of ~ 135 mAh/g. The discharge capacity was found to slowly deteriorate upon repeated cycling similar to what was observed in the case of $Li_2M_2(MoO_4)_3$. We ascertained this as due to loss of structural integrity of the electrode-active material originating from the number (x>2) of lithium inserted in the host structure. Here it is recalled that such an effect was earlier observed in the case of an analogous material, $Li_xFe_2(XO_4)_3$ which also suffered from structural phase transition (monoclinic to orthorhombic) owing to the above mentioned cause (Manthiram and Goodenough 1987).

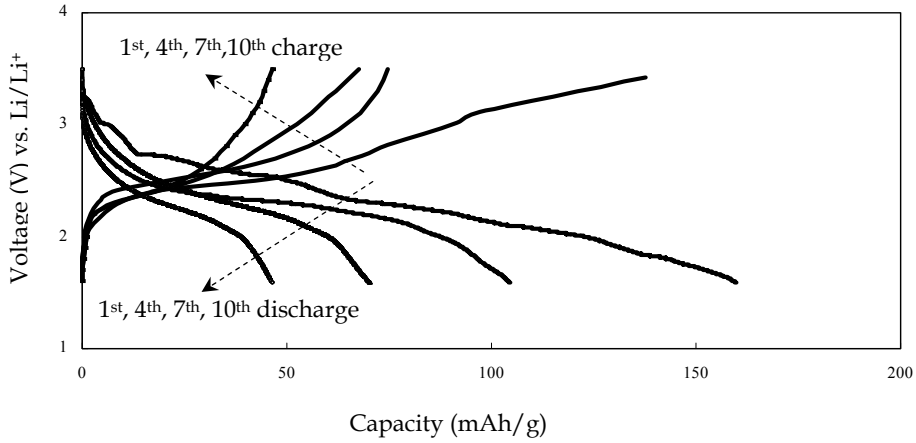

Fig. 11. Multiple discharge/charge curves of $Li_xNi_2(MoO_4)_3$//Li cell between 3.5 and 1.5 V (Prabaharan et al., 2004).

As for the half-cell $Li_xCo_2(MoO_4)_3$/Li, Fig. 12 shows the multiple discharge/charge curves. The first discharge process of Li^+ insertion began at 3.4 V (OCV) and only negligible amount of Li^+ could be inserted into $Co_2(MoO_4)_3$ until the potential decreased to 2.7 V from where the discharge curve exhibited two plateaus centered at approximately 2.6 V and 2.2 V.

These plateau regions correspond to the reduction of cobalt (Co^{3+}/Co^{2+}) and molybdenum (Mo^{6+}/Mo^{5+}) respectively. During the first discharge, ~ 2.4 Li^+ per formula unit could be inserted down to 1.5 V leading to a discharge capacity of ~ 110 mAh/g. During the first charge after discharge, 1.7 Li^+ could be extracted up to 3.5 V with a charge capacity of ~ 75 mAh/g. It is seen from Fig. 12 that the two plateau regions present during the first discharge disappeared and discharge/charge after the first cycle showed consistent potential profiles over the potential window of 3.5 – 1.5 V. These observations corroborate our findings from CV studies (Fig. 8). It is evident from Fig. 12 that the amount of lithium inserted into $Co_2(MoO_4)_3$ decreases slowly as the cycle number increases as observed in all the previous three cases for well-known reasons.

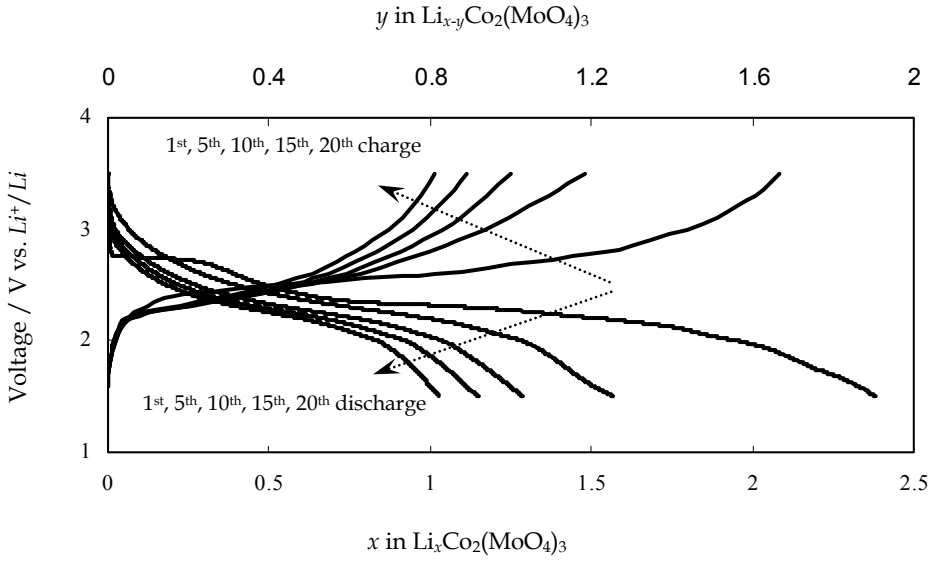

Fig. 12. Multiple discharge/charge curves of $Li_xCo_2(MoO_4)_3$//Li cell between 3.5 and 1.5 V

4.5 Limitations in using polyanion materials for lithium batteries

Although the polyanion materials examined in the present study exhibit reversible electrochemical lithium extraction/insertion properties over a considerable number of cycles, all of them invariably suffer from very low electronic conductivity which stems from their insulating nature. This ultimately resulted in poor capacity retention during prolonged cycling. As a consequence, the window of opportunity for this group of materials to be used in rechargeable lithium batteries is narrowed down.

We rectified this complexity successfully by means of a nano-composite approach wherein highly conducting nano-sized (mesoporous), high surface area activated carbon (NCB) was mixed with the electrode-active material in addition to the conventional acetylene black (AB) carbon. Interestingly, when tested against lithium in a half-cell the cycling characteristics of the materials improved as a result of an intimate contact between the active grains (grain-grain contact) and better electrolyte wetting into the pores leading to an overall enhancement in the conductivity. Accordingly, the capacity offered by the materials

followed an increasing trend. The following section gives a detailed description of the formation nano-composites and the results obtained for conductivity enhancement.

5. Formation of nano-composite electrodes and improved electrochemical properties of polyanion cathode materials

5.1 Preparation of nano-composite electrodes

Nano-composite positive electrodes (cathode) consisted of 65% active material, 5% binder (PTFE) and 30% conducting carbon mixture. The conducting carbon mixture comprised an equal proportion of acetylene black (AB) [BET surface area: 394 m^2/g; Grain size: 0.1 μm -10 μm; σ_e: 10.2 S/cm] and NCB (nano-sized particles exhibiting mesoporosity of 3-10 nm; Monarch 1400, Cabot Inc, USA, BET surface area: 469 m^2/g; Grain size: 13 nm; σ_e; 19.7 S/cm). The nano-composite electrodes were fabricated following the usual procedure.

5.2 Modification in the electrochemical properties of polyanion cathode materials

To investigate the effect of nano-sized carbon black on the electrochemical behaviour of all the four materials, nano-composite cathode/Li half-cells were tested galvanostatically under the same experimental conditions.

The first charge/discharge curves obtained using the nano-composite positive electrodes ($Li_2M_2(MoO_4)_3$) were compared to the first charge/discharge curves of the conventional electrode (without NCB) as shown in Fig. 13.

Fig. 13 shows a clear evidence for the difference between the two cases in terms of IR drop, the amount of lithium removal/insertion and shape of the discharge profiles. The reduced IR (ohmic) drop at the beginning of the discharge process after charge in the case of the nano-composite electrodes is well seen in Fig 13 (inset). But, in the conventional case, a large IR (ohmic) drop was observed. As for the $Li_2Ni_2(MoO_4)_3$ nano-composite electrode, we obtained a first discharge capacity of 86 mAh/g down to 2.0 V which is approximately a four fold excess compared to the conventional electrode where the discharge capacity was 26 mAh/g down to 2.0 V. A first discharge capacity of 55 mAh/g was obtained in the case of $Li_2Co_2(MoO_4)_3$ nano-composite electrode which is 2.5 timer higher in comparison with the conventional type $Li_2Co_2(MoO_4)_3$ electrode.

Apart from the above changes observed, a smooth discharge profile of the nano-composite electrode right from the beginning down to 2.0 V is note worthy; whereas the conventional electrode seems to exhibit two-slope feature during the first discharge that appears distinctly on the discharge plateau. These significant changes observed in the discharge profile clearly demonstrate the role of non-graphitized carbon black (nano-sized) on the electrochemical properties of the host cathode.

We compared the first discharge/charge curves obtained using the nano-composite positive electrodes ($Li_xM_2(MoO_4)_3$) with the first discharge/charge curves of the conventional electrodes as shown in Fig. 14.

It is noticeable from Fig. 14a that there is dissimilarity between the two cases in terms of IR (ohmic) drop even though the discharge/charge profiles look alike. In the usual case, IR drop at the beginning of the discharge process was large and the discharge profile was found to proceed vertically down to 2.7 V from OCV (3.5 V) without any quantitative lithium insertion reaction. This is due to a very low electronic conductivity of polyanion

materials which is a common intricacy preventing the polyanions from practical use. On the other hand, much minimized IR drop in the case of the nano-compoiste electrode is

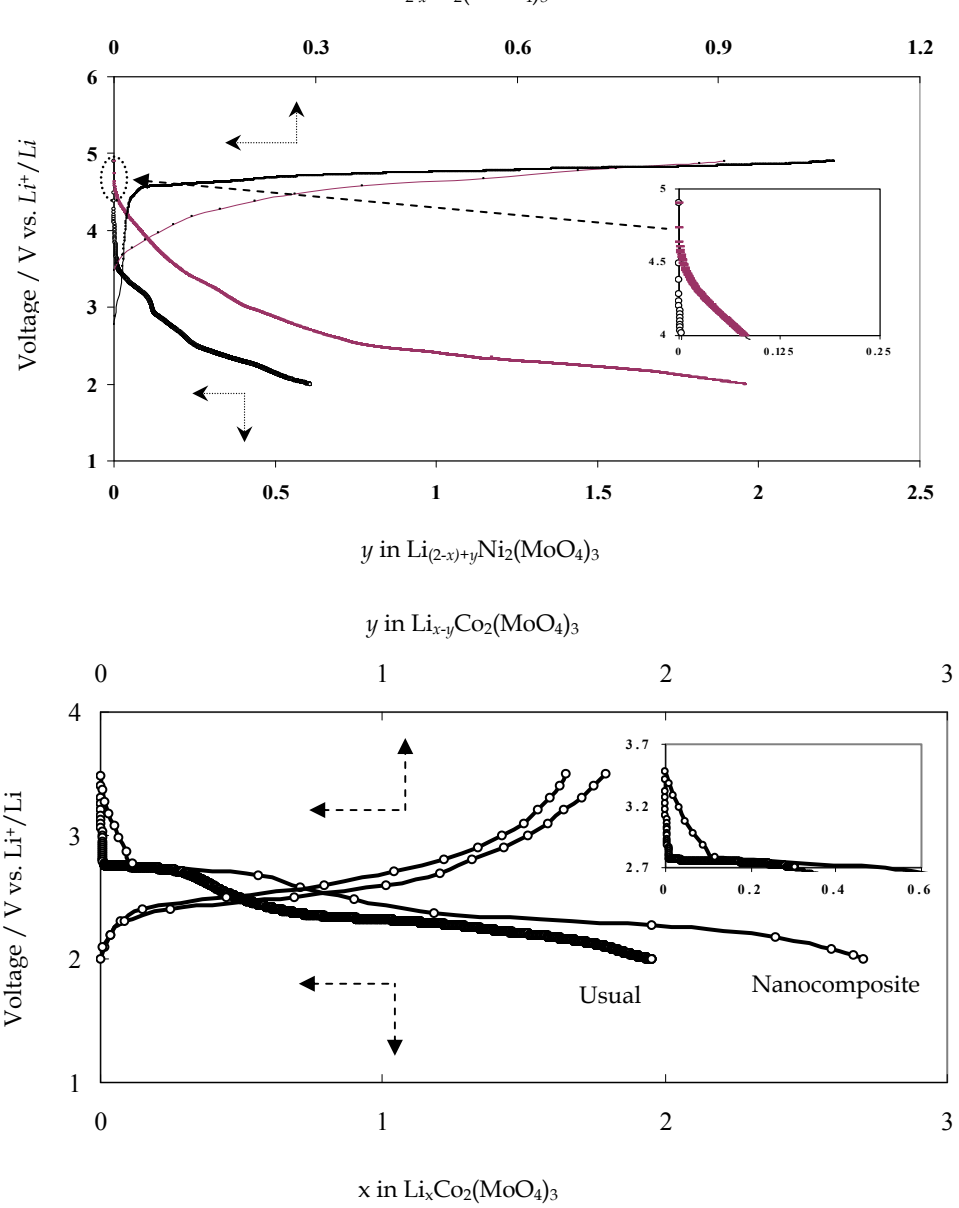

Fig. 13. Comparison of first charge/discharge of nano-composite and conventional $Li_2M_2(MoO_4)_3$ against lithium between 4.9 and 1.5 V. (Prabaharan et al., 2006).

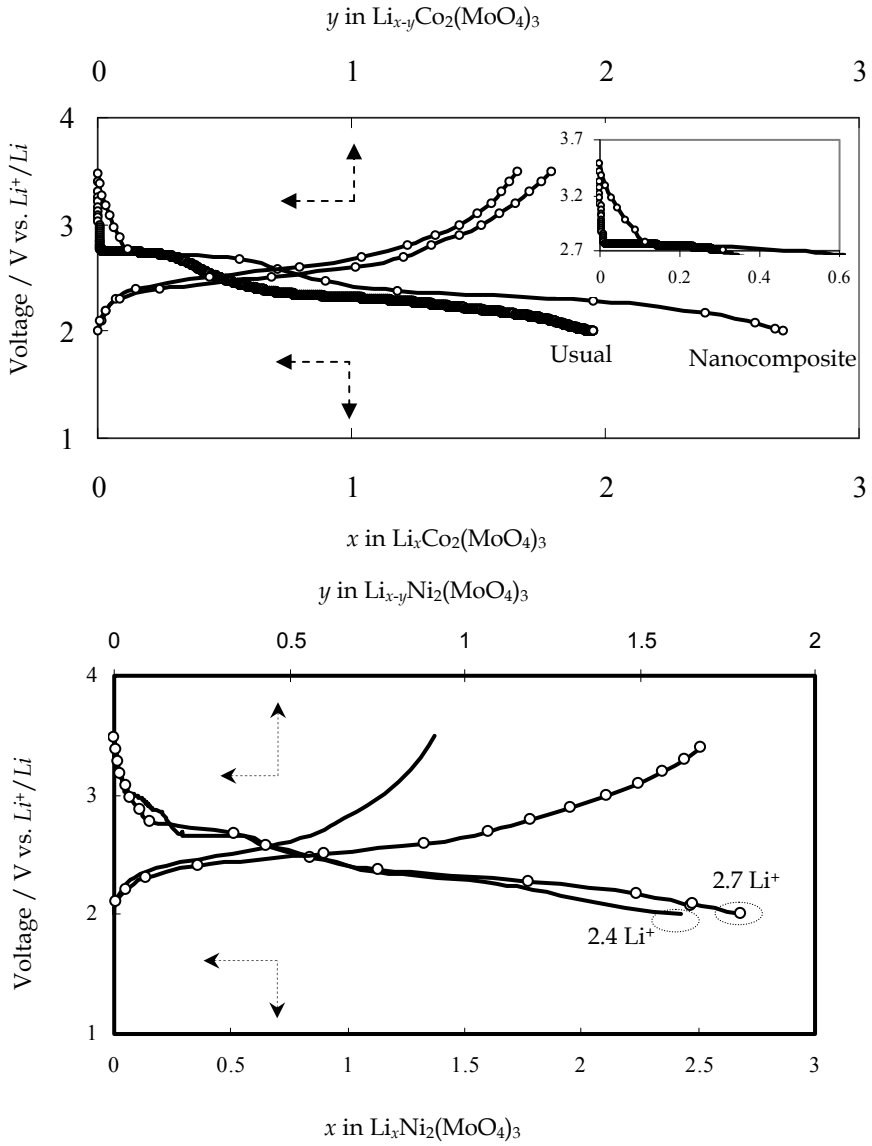

Fig. 14. Comparison of first charge/discharge of nano-composite and conventional $Li_xM_2(MoO_4)_3$ against lithium between 3.5 and 2.0 V. (Prabaharan et al., 2004, 2007, 2008).

well evident in Fig. 14a (inset) and the discharge profile was observed to exhibit an exponential decay with a progressive insertion of lithium in the electrode. Furthermore, there is a difference between the two cases in the amount of lithium insertion during discharge. About 2.7 Li^+ was inserted in the nano-composite electrode corresponding to the first discharge capacity of 121 mAh/g. This value is larger than the capacity obtained from

the conventional composite electrode added with acetylene black (87 mAh/g for 1.95 Li^+ down to 2.0 V).

As for the $Li_xNi_2(MoO_4)_3$, the first discharge/charge curves corresponding to the usual and nano-composite electrodes are distinct concerning the discharge capacity and not the IR drop (Fig. 14b). Usual $Li_xNi_2(MoO_4)_3$ delivered 108 mAh/g as its first discharge capacity, but nano-composite $Li_xNi_2(MoO_4)_3$ gave rise to a first discharge capacity of 120 mAh/g. Although the nano-composite $Li_xNi_2(MoO_4)_3$ indicated better discharge/charge characteristics than the usual $Li_xNi_2(MoO_4)_3$, we could observe that the performance is not comparable to the level of enhancement in the nano-composite $Li_xCo_2(MoO_4)_3$. We ascribed the variation in the electrochemical performance as due to the variation in the grain size.

It is apparent that the role of NCB is significant in modifying the discharge/charge profiles with much improvement. The vital role of nano-sized high surface area activated carbon in improving the electrochemical properties of the positive electrode is implicit through these prominent variations monitored in the discharge profile. Presence of NCB in the electrode increased the electronic conductivity by enhancing the intactness between the active grains.

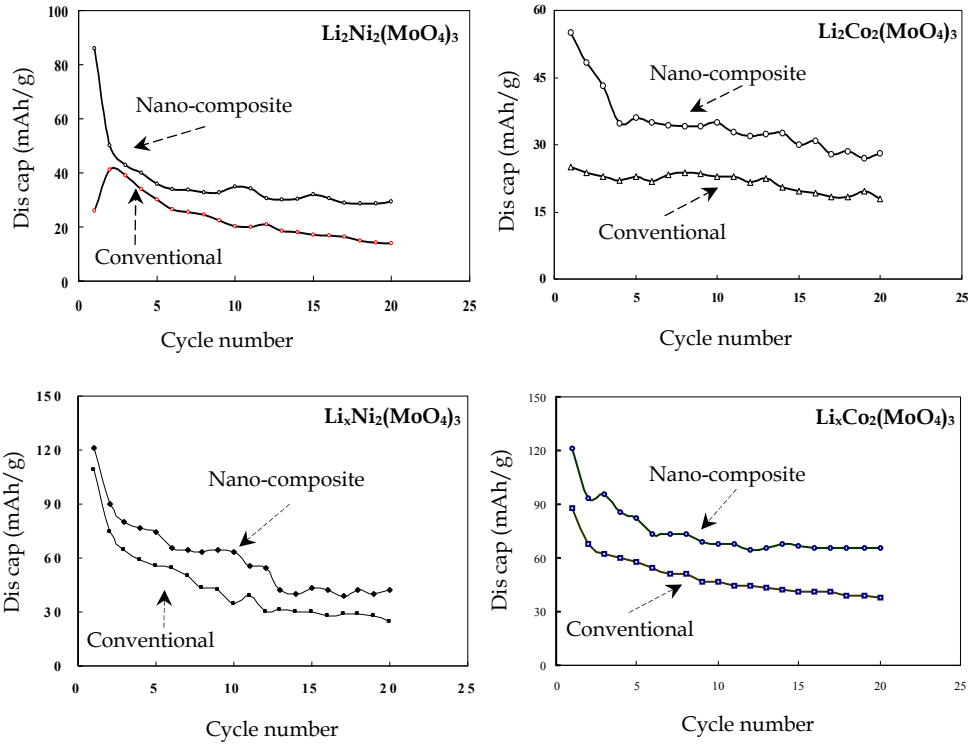

Fig. 15. Discharge capacity of conventional and nano-composite electrodes vs. cycle number

With an aspiration to examine the effect of mesoporous carbon during prolonged cycling, we carried out multiple cycling tests on the test cells for the first twenty cycles under the same experimental conditions. The amount of lithium inserted into the nano-composite

electrode during discharge was larger than that in the conventional electrode for all the twenty cycles studies in all the four cases. Besides this, the charge profiles also showed significant improvement, which would certainly help inserting more lithium in the subsequent discharge. The results are summarized in the form of variation of discharge capacity vs. cycle number. The variation in the discharge capacity with cycle number corresponding to the usual and nano-composite $Li_2M_2(MoO_4)_3$ and $Li_xM_2(MoO_4)_3$ are shown in Fig. 16.

	Electrochemical properties of $Li_2Ni_2(MoO_4)_3$ electrode			
	Conventional cathode		Nano-composite cathode	
Cycle no.	Amount of Li^+ inserted down to 2.0 V	Discharge capacity (mAh/g)	Amount of Li^+ inserted down to 2.0 V	Discharge capacity (mAh/g)
1	0.6	26	2	86
5	0.7	30	0.8	36
10	0.5	20	0.78	35
15	0.4	17	0.72	32
20	0.3	14	0.7	29

Table 1. Enhanced electrochemical properties of nano-composite $Li_2Ni_2(MoO_4)_3$ electrode compared to conventional $Li_2Ni_2(MoO_4)_3$ electrode.

	Electrochemical properties of $Li_2Co_2(MoO_4)_3$ electrode			
	Conventional cathode*		Nano-composite cathode**	
Cycle no.	Amount of Li^+ inserted down to 2.0 V	Discharge capacity (mAh/g)	Amount of Li^+ inserted down to 2.0 V	Discharge capacity (mAh/g)
1	0.53	23	1.25	55
5	0.522	22.9	0.8	36
10	0.52	22.8	0.79	35
15	0.45	19.7	0.69	30
20	0.4	17.8	0.64	28

Table 2. Enhanced electrochemical properties of nano-composite $Li_2Co_2(MoO_4)_3$ electrode compared to conventional $Li_2Co_2(MoO_4)_3$ electrode.

The observed improvement with regard to electrochemical properties of NCB added positive composite electrodes over the conventional electrodes with mere acetylene black are summarized in Tables 1, 2, 3 and 4 for all the four cases. It is obvious from the tables that NCB added positive electrodes exhibit improved extended cycling characteristics. The nano-sized grains accompanied by the presence of meso porosity in the NCB could have facilitated the enhanced grain-grain contact between the electrode active particles and provided the enhanced intactness between electrode active grains and the conductive additive carbons established via PTFE upon repeated charge/discharge cycles.

	Electrochemical properties of $Li_xNi_2(MoO_4)_3$ electrode			
	Conventional cathode*		Nano-composite cathode**	
Cycle no.	Amount of Li^+ inserted down to 2.0 V	Discharge capacity (mAh/g)	Amount of Li^+ inserted down to 2.0 V	Discharge capacity (mAh/g)
1	2.42	109	2.68	121
5	1.24	55.5	1.66	70
10	0.78	40	1.4	63
15	0.68	34	0.95	43
20	0.57	28	0.92	42

Table 3. Enhanced electrochemical properties of nano-composite $Li_xNi_2(MoO_4)_3$ electrode compared to conventional $Li_2Ni_2(MoO_4)_3$ electrode.

	Electrochemical properties of $Li_xCo_2(MoO_4)_3$ electrode			
	Conventional cathode*		Nano-composite cathode**	
Cycle no.	Amount of Li^+ inserted down to 2.0 V	Discharge capacity (mAh/g)	Amount of Li^+ inserted down to 2.0 V	Discharge capacity (mAh/g)
1	1.95	87	2.7	121
5	1.3	58	1.9	85
10	1	44	1.6	73
15	0.9	41	1.5	66
20	0.8	37	1.5	66

Table 4. Enhanced electrochemical properties of nano-composite $Li_xCo_2(MoO_4)_3$ electrode compared to conventional $Li_2Ni_2(MoO_4)_3$ electrode.

5. Conclusion

We identified a group of NASICON open framework structured polyanion materials and examined the materials for rechargeable lithium battery application. We found that the open framework structure of these materials facilitated easy insertion/extraction of lithium into/from their structure. We synthesized the materials in lithium-rich $[Li_2M_2(MoO_4)_3]$ and lithium-free $[Li_xM_2(MoO_4)_3]$ (M= Ni, Co) phases, for the first time, by means of a low temperature soft-combustion technique. The soft-combustion synthesis usually yields single-phase materials with high phase purity and is suitable for bulk preparation of battery grade electrode powders. The materials were characterized for structure, morphology and electrochemical lithium insertion/extraction kinetics and the results were presented and discussed in the light of XRD, SEM and electrochemical techniques in relation to the electrode-active character of the materials.

All the materials were found to crystallize in a single phase structure with submicron sized particles. The electrode-active behavior of the new materials was examined in a two-electrode configuration utilizing a Li^+ non-aqueous environment. Both the systems were

found to exhibit electrochemically reversibility as evidenced from Slow Scan Cyclic Voltammetry (SSCV) studies. As for the lithium-rich phases, $Li_2M_2(MoO_4)_3$, the charge-discharge profiles obtained by means of Galvanostatic cycling tests between 4.9 V and 1.5 V signified removal/reinsertion of lithium in the new materials with good discharge capacity. The Galvanostatic discharge/charge tests conducted between 3.5 and 1.5 V corresponding to the lithium-free phases, $Li_xM_2(MoO_4)_3$ also indicated the reversibility of the materials.
During extended cycling, structural disruption of the materials was evidenced from the shape of the cycling profiles regardless of the initial phase of the materials. The discharge capacity was found to decrease during prolonged cycling due to a very low lattice conductivity of the polyanaion systems.
We applied a novel and efficient nano-composite approach to boost the surface conductivity of the polyanion materials by introducing a nano-sized mesoporous carbon black (NCB). We found that the high surface area carbon could increase the intactness between the electrode-active grains much more effectively leading to increased conductivity of the electrode material on the whole. Consequently, we proved that the nano-composite approach is very effective in improving the electrochemical characteristics of the group of new materials taken for the present investigation with a substantial enhancement in discharge capacity.

6. References

Alvarez-Vega, M.; Amador, U. & Arroyo-de Dompablo, ME. (2005). Electrochemical Study of $Li_3Fe(MoO_4)_3$ as Positive Electrode in Lithium Cells. *Journal of the Electrochemical Society,* vol. 152, no. 7, pp. A1306-A1311.

Arroyo-de Dompablo, ME.; Alvarez-Vega, M.; Baehtz, C. & Amador, U. (2006). Structural Evolution of $Li_{3+x}Fe(MoO_4)_3$ upon Lithium Insertion in the Compositional Range $0 \leq x \leq 1$. *Journal of the Electrochemical Society,* vol. 153, no. 2, pp. A275-A281.

Barker, J.; Saidi, MY. & Swoyer, J.L. (2003). Electrochemical insertion properties of the novel lithium vanadium fluorophosphates. *Journal of the Electrochemical Society*, 150 (10), A1394-A1398.

Begam, KM.; Michael, MS.; Taufiq-yap, Y.H. & Prabaharan, S.R.S. (2004). New lithiated NASICON-type $Li_2Ni_2(MoO_4)_3$ for rechargeable batteries: Synthesis, structural and electrochemical properties. *Electrochemical and Solid State Letters*, vol. 7, no. 8, pp. A242-246.Begam, KM.; Michael, M.S. & Prabaharan, S.R.S. (2004). Topotactic Lithium Insertion/Extraction Properties of a New Polyanion Material, $Li_xCo_2(MoO_4)_3$ [$0 \leq x < 3$] for rechargeable lithium batteries. Proceedings of the 9th Asian Conference on Solid State Ionics, pp. 461-468, ISBN 981-238-932-6, South Korea, June 2004, World Scientific, Singapore.

Begam, KM.; Selladurai, S.; Michael, M;.S. & Prabaharan, S.R.S. (2004). Synthesis and redox behavior of a new polyanion compound, $Li_2Co_2(MoO_4)_3$ as 4-V class positive electrode material for rechargeable lithium batteries. J*ournal of Ionics*, vol. 10, pp. 77-83.

Begam, KM.; Taufiq-Yap, YH.; Michael, MS. & Prabaharan, S.R.S. (2004). A new NASCON-type polyanion, $Li_xNi_2(MoO_4)_3$ as 3-V class positive electrode material for rechargeable lithium batteries. *Solid State Ionics*, vol. 172, pp. 47-52.

Begam, KM, & Prabaharan, S.R.S. (2006). Effect of mesoporous carbon black on the cycling characteristics of $Li_2Co_2(MoO_4)_3$ for lithium batteries. Proceedings of the 10th Asian Conference on Solid State Ionics, pp. 313-320, ISBN 981-256-877-8, Srilanka, June 2006, World Scientific, Singapore.

Begam, KM, & Prabaharan, S.R.S. (2006). Improved cycling performance of nano-composite $Li_2Ni_2(MoO_4)_3$ as a lithium battery cathode material. *Journal of Power Sources*, vol. 159, pp. 319-322.

Begam, KM.; Michael, M.S. & Prabaharan, S.R.S. (2007). Enhancd cycling properties of transition metal molybdates, $Li_xM_2(MoO_4)_3$ {0≤x<3} [M = Co, Ni]: a nono-composite appraoch for lithium batteries. *Journal of Ionics*, vol. 13, pp. 467-471.

Begam, KM.; Michael, M.S. & Prabaharan, S.R.S. (2008). Nanostructured lithium-free oxyanion cathode, $Li_xCo_2(MoO_4)_3$ [0≤x<3] for 3 V class lithium batteries. *J Solid State Electrochem.* Vol. 12, pp. 971-977.

Bykov, AB.; Chirkin, AP.; Demyanets, LN.; Doronin, S.N. & Muradyan, L.N. (1990). Superionic conductors $Li_3M_2(PO_4)_3$ (M=Fe, Sc, Cr): Synthesis, structure and electrophysical properties. *Solid State Ionics*, vol. 38, no. 1-2, pp. 31-52.

Chung, SY.; Blocking, JT. & Chiang, Y.M. (2002). Electronically conductive phospho-olivines as lithium storage electrodes. *Nature materials*, vol. 1, pp. 123-128.

Davis, RJ.; Hobson, MJ.; Macklin, WJ. & Neat, RJ. (2004). Vanadium phosphate glasses. Effect of composition on their structure and performance as cathodes in high-temperature lithium polymer-electrolyte cells. *J. Mater. Chem.* Vol. 4, pp. 113-118.

Gaubicher, J.; Wurm, C.; Goward, G.; Masquelier, C. & Nazar, L.F. (2000). Rhombohedral form of $Li_3V_2(PO_4)_3$ as a cathode in Li-ion batteries. *Chemistry of Materials,* vol. 12, no. 11, pp. 3240-3242.

Goodenough, JB.; Hong, HYP. & Kafalas, JA. (1976). Fast Na^+ ion transport in skeleton structures. *Materials Research Bulletin*, vol. 11, no. 2, pp. 203-247.

Harrison, WTA.; Chowdary, U.; Machiels, CJ.; Sleight, AW. & Cheetam, AK. (1985). Preparation of ferric tungstate and its catalytic behavior toward methanol. *Journal of Solid State Chemistry*, vol. 60, no. 1, pp. 101-106.

Hirano, A.; Kanno, R.; Takeda, Y. & Yamaguchi, Y. (1995). Relationship between non-stoichiometry and physical properties in $LiNiO_2$. *Solid State Ionics*, vol. 78, pp. 123-131.

Hong, HYP. (1976). Crystal structure and crystal chemistry in the system $Na_{1+x}Zr_2Si_xP_{3-x}O_{12}$. *Materials Research Bulletin*, vol. 11, no. 2, pp. 173-182.

Huang, H.; Yin, SC. & Nazar, LF. (2001). Approaching theoretical capacity of $LiFePO_4$ at room temperature at high rates. *Electrochemical and Solid-State Letters*, vol. 4, no. 10, pp. A170-A172.

Huang, H.; Yin, SC.; Kerr, T; Taior, N. & Nazar, LF. (2002). Nanostructured Composites: A High Capacity, Fast Rate $Li_3V_2(PO_4)_3$/Carbon Cathode for Rechargeable Lithium Batteries (p 1525-1528)*Adv. Mater.* Vo. 14, pp. 1525-1528.

Koboyashi, H.; Shigemura, H.; Tabuchi, M.; Sakaebe, H.; Ado, K. & Kagayama, H. (2000). Electrochemical properties of hydrothermally obtained $LiCo_{1-x}Fe_xO_2$ as a positive electrode material for rechargeable lithium batteries. *Journal of the Electrochemical Society,* vol. 147, no. 3, pp. 960-969.

Long GJ.; Longworth G.; Battle P.; Cheetham AK.; Thundathil RV. & Beveridge D. (1979). A study of anhydrous iron (III) sulfate by magnetic susceptibility, Mossbauer and neutron diffraction techniques. *Inorganic Chemistry*, vol. 18, no. 3, pp. 624-632.

Manthiram, A. & Goodenough, JB. (1987). Lithium insertion into $Fe_2(MoO_4)_3$ frameworks: Comparison of M=W with M=M*. *Journal of Solid State Chemistry,* vol. 71, pp. 349-360.

Manthiram, A. & Goodenough, JB. (1989). Lithium insertion into $Fe_2(SO_4)_3$ frameworks. *Journal of Power Sources*, vol. 26, pp. 403-409.

Morcrette, M.; Leriche, JB.; Patoux, S.; Wurm, C. & Masquelier, C. (2003). In situ X-ray diffraction during lithium extraction from rhombohedral and monoclinic $Li_3V_2(PO_4)_3$. *Electrochemical and Solid State Letters,* vol. *6*, no. 5, pp. A80-A84.

Moshtev, RV.; Zlatilova, P.; Manev, P. & Sato, A. (1995). The $LiNiO_2$ solid solution as a cathode material for rechargeable lithium batteries. *Journal of Power Sources*, vol. 54, pp. 329-333.

Nadiri, A.; Delmas, C.; Salmon, R. & Hagenmullar, P. (1984). J. Rev. Chim.Miner, vol. 21, pp. 83.

Nanjundasamy, KS.; Padhi, AK.; Goodenough, JB.; Arai, H. & Yamaki, J. (1996). Synthesis, redox potential evaluation and electrochemical characteristics of NASICON-related-3D framework compounds. *Solid State Ionics*, vol. 92, pp. 1-10.

Nazar, L.; Huang, H.; Yin, S.C. & Kerr, T. (2002). Transition metal phosphates as positive electrodes for Li-ion batteries-Structure, microstructure and properties.

Proceedings of 11th International meeting on lithium batteries, 212, Monterey, CA.

Okada, S. (1996). *International Symposium on lithium batteries*, P19. Tokyo.

Ozima, M.; Sato, S. & Zoltai, T. (1977). The crystal structure of a lithium-nickel molybdate, $Li_2Ni_2Mo_3O_{12}$, and the systematics of the structure type. Acta Crystallographica, vol. B33, pp. 2175-2181.

Padhi, AK.; Nanjundasamy, KS, & Goodenough, JB. (1997). Phospho-olivines as positive electrode materials for rechargeable lithium batteries. *Journal of the Electrochemical Society*, vol. 144, no. 4, pp. 1188-1194.

Padhi, AK.; Nanjundasamy, KS.; Masquelier, C. & Goodenough, JB. (1997). Mapping of transition metal redox energies in phosphates with NASICON structure by lithium intercalation. *Journal of the Electrochemical Society*, vol. 144, no. 8, pp. 2581-2586.

Padhi, AK.; Manivannan, V. & Goodenough, J.B. (1998). Tuning the position of the redox couples in materials with NASICON structures by anionic substitution. *Journal of the Electrochemical Society,* vol. 145, no. 5, pp. 1518-1520.

Patoux, S.; Wurm, C.; Morcrette, M.; Rousse, G. & Masquelier, C. (2003). A comparative structural and electrochemical study of monoclinic $Li_3Fe_2(PO_4)_3$ and $Li_3V_2(PO_4)_3$. Journal of Power Sources, vol. 119-121, pp. 278-284.

Prabaharan, SRS.; Ramesh, S.; Michael, MS. & Begam, KM. (2004). Characterization of soft-combustion-derived NASICON-type $Li_2Co_2(MoO_4)_3$ for lithium batteries. *Materials Chemistry and Physics*, vol. 87, pp. 318-326.

Prabaharan, SRS.; Fauzi, A.; Michael, MS. & Begam, KM. (2004). New NASICON-type $Li_2Ni_2(MoO_4)_3$ as a positive electrode material for rechargeable lithium batteries. *Solid State Ionics*, vol. 171, pp. 157-165.

Prabaharan, SRS.; Michael, MS.; Ramesh, S., & Begam, K.M. (2004). Synthesis and redox properties of $Li_xNi_2(MoO_4)_3$: a new 3-V class positive electrode material for rechargeable lithium batteries. *Journal of Electroanalytical Chemistry,* vol. 570, pp. 107-112.

Prabaharan, SRS.; Michael, MS. & Begam, K.M. (2004). Synthesis of a polyanion cathode material, $Li_2Co_2(MoO_4)_3$ and its electrochemical properties for lithium batteries. *Electrochemical and Solid State Letters*, vol. 7, no. 11, pp. A416-A420.

Reiff, WM.; Zhang, JH. & Torardi, CC. (1986). Topochemical lithium insertion into $Fe_2(MoO_4)_3$: structure and magnetism of $Li_2Fe_2(MoO_4)_3$. *Journal of Solid State Chemistry*, vol. 62, pp. 231-240.

Reimers, J.N. & Dahn, J.R. (1992). Electrochemical and in situ X-ray diffraction studies of lithium intercalation in Li_xCoO_2. *Journal of the Electrochemical Society,* vol. 139, no. 8, pp. 2091-2096.

Saidi, MY.; Barker, J.; Huang, H.; Swoyer, J.L. & Adamson, G. (2002). Performance characteristics of lithium vanadium phosphate as a cathode material for lithium-ion batteries. *Journal of Power Sources,* vol. 119-121, pp. 266-272.

Saidi, MY.; Barker, J.; Huang, H.; Swoyer, J.L. & Adamson, G. (2002). Electrochemical properties of lithium vanadium phosphate as a cathode material for lithium-ion batteries. *Electrochemical and Solid State Letters,* vol. 5, no. 7, pp. A149-A151.

Sato, M.; Ohkawa, H.; Yoshida, K.; Saito, M. & Toda, K. (2000). Enhancement of discharge capacity of $Li_3V_2(PO_4)_3$ by stabilizing the orthorhombic phase at room temperature. *Solid State Ionics,* vol. 135, no. 1-4, pp. 137-142.

Tarascon, JM. & Armand, M. (2001). Issues and challenges facing rechargeable lithium batteries. *Nature,vol*. 414, pp. 359-367.

Torardi, CC. & Prince, A. (1986). Structure of the lithium insertion compound $Li_2Fe_2(MoO_4)_3$ from neutron powder diffraction data. *Materials Research Bulletin*, vol. 21, no. 6, pp. 719-726.

Wang, GX.; Bradhurst, DH.; Dou, SX. & Liu, HK. (2003). $LiTi_2(PO_4)_3$ with NASICON-type structure as lithium-storage materials. Journal of Power Sources, vol. 124, pp. 231-236.

Yang, S.; Song, Y.; Zavali, PY. & Whittingham, M.S. (2002). Reactivity, stability and electrochemical behavior of lithium iron phosphate. *Electrochemistry Communications*, vol. 4, pp. 239-244.

Yin, SC.; Grondey, H.; Strobel, P.; Huang, H. & Nazar, LF. (2003). Charge ordering in lithium vanadium phosphates: Electrode materials for lithium ion batteries. J. Am. Chem.Soc. vol. 125, pp. 326-327.

Zhang, D.; Tong, Z.; Xu, G.; Li, S. & Ma, J. (2009). Template fabrication of $NiFe_2O_4$ nanorods; Characterization, magnetic and electrochemical properties. *Solid State Sciences*, vol. 11, pp. 113-117.

Zhu, XJ.; Liu, YX.; Geng, LM. & Chen, LB. (2008). Synthesis and performance of lithium vanadium phosphate as cathode materials for lithium ion batteries by a sol-gel method. *Journal of Power Sources*, vol. 184, pp. 578-582.

6

Development of contact-wireless type railcar by lithium ion battery

Takashi Ogihara
University of Fukui
Japan

1. Introduction

As energy-saving and global warming countermeasures, the use of new energy systems such as rechargeable batteries, fuel cells and super capacitor that reduce carbon dioxide discharge are expected. The transportation section in particular occupies 24% of energy consumption and also 20% of carbon dioxide discharge. So far, lead and nickel hydrogen batteries have been used for hybrid electric vehicles (HEVs) and electric cars or vehicles (EVs). However, these batteries are characterized by low power density and low energy density and are very heavy. Among the rechargeable batteries, lithium ion batteries have the highest energy density and power density and are also the lightest. Therefore, the lithium ion battery is suitable as a power source of certain forms of transportation, including the EV, electric bus and railway. However, Co type lithium ion battery is not suitable because of high cost, low thermal stability, toxicity. Mn type lithium ion battery overcame the demerit of Co type lithium ion battery. Therefore, Mn type lithium ion battery is the mainstream of EV and HEV.

Recently, the rechargeable battery (lithium ion or nickel hydrogen) and fuel cell have been applied on the running of contact-wireless type of railcar (Sameshima, et.al, 2004, Ogasa, et.al, 2006). Lithium ion battery is expected as the driving source of it because of highest energy density and power density among the rechargeable. Some following advantages of contact-wireless type railcar with lithium ion batteries are expected.

(1) The townscape is improved and the maintenance cost of overhead contact wire is reduced.

(2) It is possible to utilize as an emergency power source in the overhead contact wire supply failure by disaster and accident.

(3) The discharge of carbon dioxide, nitrogen oxides and sulhur oxides can be drastically reduced compared with diesel car.

(4) The energy-saving effect for running of railcar is improved by charging regenerative energy with rechargeable batteries.

We have been tried the running test of DC 600V and VVVF (Variable Voltage Variable Frequency) inverter type railcar by using large Mn type lithium ion battery at the business line of local railway (Ozawa, et.al, 2007, 2008) in Japan.

Now, new VVVF inverter type railcars use the regenerative brake which the kinetic energy of railcar converts to electricity that is fed back into contact-wire. However, the regenerative braking loses its effectiveness when there are no other railcars running nearby that railcar immediately use the regenerated electricity. VVVF inverter has been used in the new railcar to raise the energy saving in the running. It was well-known that the loss of regenerative energy often occurred because the regenerative energy was not charged to other railcar which ran nearby. To solve the problem, it is considered that the use of lithium ion battery is effective for the charge of regenerative energy. In this chapter, the performance and energy-saving effect of a railcar which is run by a large Mn type lithium ion battery is described.

2. Lithium ion battery

Homogeneous Al (5mol%) doped lithium manganate powders (LMP) were used as cathode materials. LMP were continuously large produced by spray pyrolysis technique (The flame type spray pyrolysis equipment) using the aqueous solution of lithium nitrate and manganese nitrate (Mukoyama, et.al, 2007). Powder preparation by spray pyrolysis potentially offers the following advantages. (1) The obtained cathode particles are spheres of submicrometer size with a narrow size distribution and have porous microstructure.
(2) Chemical homogeneity of cathode materials is enhanced as compared with those prepared with solid state reaction.
(3) The cathode precursors can be prepared in much shorter time than that required for solid state reaction or the sol-gel method.
Figure 1 show the flame type spray pyrolysis equipment used. It is consisted of two-fluid nozzle, flame furnace with gas burner and powder collector with bag filter. The starting aqueous solution was atomized by a two-fluid nozzle with diameter of 20μm (a) and introduced to flame furnace, in which the temperature of flame was set to 700°C (b). The flame was generated by gas burner with city-gas. LMP was continuously collected with a bag filter (c). Few hundred kg of aluminium doped LMP was successfully produced. It was known that the addition of aluminium ion led to the high stability of life cycle of lithium manganate cathode and avoid the dissolution of manganese ion from LMP. The optimum concentration of aluminium ion was 5mol% from the past experimental results.

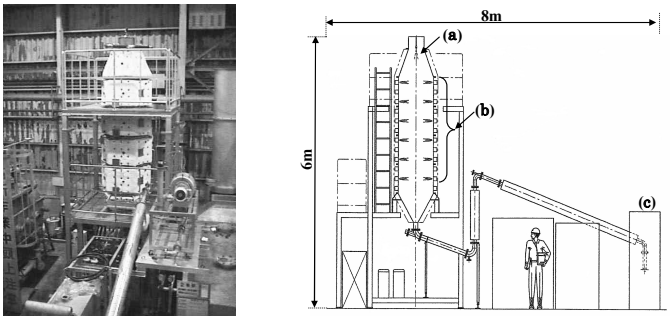

Fig. 1. Flame type spray pyrolysis apparatus

Typical SEM photograph and X-ray diffraction pattern of LMP is shown in Fig.2. SEM photograph showed that LMP had the spherical morphology with non-aggregation and consisted of primary particles with about 100nm. The average particle size and geometrical standard deviation of LMP was about 2μm and 1.3, respectively. Specific surface area of LMP measured by BET method was about $10m^2/g$. X-ray diffraction patterns showed that LMP was well crystallized to spinel structure with a space group (Fd3m). The diffraction lines of impurities except for spinel phase were not observed. Atomic absorption spectrometry analysis showed that the molar ratio of Li/Mn was kept to starting solution composition. The content of aluminium was 4.9mol%.

The electrochemical properties of LMP were investigated using 2032 type coin cell. LMP was well calcined for 12h at 800°C before the use of cathode. It is necessary for use of LMP to reduce the specific surface area to less than $1m^2/g$ because the crack or lamination often occur on the surface of cathode. The cathode was prepared using 88wt% LMP, 6wt% acetylene black and 6wt% fluorine resin (PVDF). LMP was mixed with acetylene black and a fluorine resin to obtain slurry and then coated on an aluminum sheet using a doctor blade. Lithium metal sheet was used as the anode. A porous polypropylene sheet (Cellgard 2400) was used as the separator. As the electrolyte, $1mol/dm^3$ $LiPF_6$ in ethylene carbonate / 1,2-dimethoxyethane (EC : DME = 1:1 in volume ratio) was used. The rechargeable properties of lithium manganate cathode were examined with 2032 type coin cell.

Figure 3 shows the typical rechargeable curves of lithium manganate cathode at rate 1C ($1mA/cm^2$) and the cycle performance at rate of 10C ($10mA/cm^2$). The addition of aluminium ion led to S type of rechargeable curve and the voltage jump which is observed in the rechargeable of lithium manganate at about 4V is disappeared. This suggests that the electrochemical reaction is a homogeneous solid state reaction and the cycle stability of lithium manganate cathode is improved. The first discharge capacity of lithium manganate cathode was 120mAh/g at rate of 1C. The discharge capacity of lithium manganate cathode was retained at about 110mAh/g after 1000th cycle. When the rechargeable rate increased to 10C, the rechargeable capacity decreased to 90mAh/g. However, 90% of first discharge capacity was retained after the 1000th cycle at rate of 10C. It was found that lithium manganate cathode also exhibited high cycle stability at a high rate.

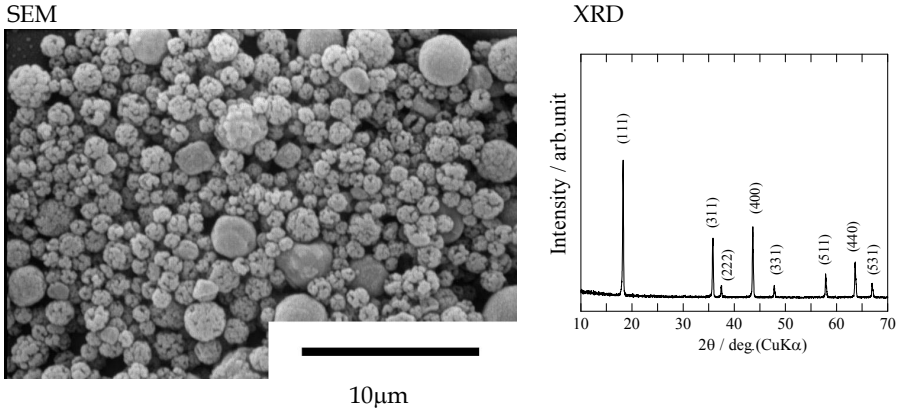

Fig. 2. SEM photograph and XRD patterrn of LMP

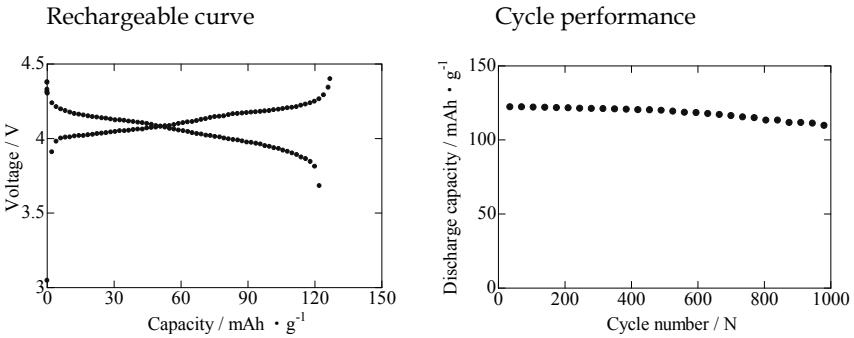

Fig. 3. Rechargeable curve and cycle performance of cathode

A laminate sheet type lithium ion cells (170mm x 160mm x 5mm, 250g, 7Ah, 3.8V) were produced using LMP and a mixture of hard carbon and graphite (volume ratio was 1:1) in a glove box under an argon atmosphere. The rechargeable capacity of laminate sheet type lithium ion cell was 110mAh/g at rate of 1C. The rechargeable capacity of LMP synthesized by classic solid state reaction was about 90mAh/g. The use of LMP derived from spray pyrolysis improved 22% of rechargeable capacity. This result led to high energy and power density of lithium ion cell. The energy and power densities of the lithium ion cell were about 120Wh/kg and 4500W/kg, respectively. The power density was obtained as follows. The voltage in the 10s of applying pulsed current for 10s to 1C was plotted for the current value and power density at state of charge (SOC) 50% was obtained from the linear relationship. This may be resulted in nanostructure of LMP. The charge and discharge among cathode and anode is carried out by fast diffusion rate of Li ion.

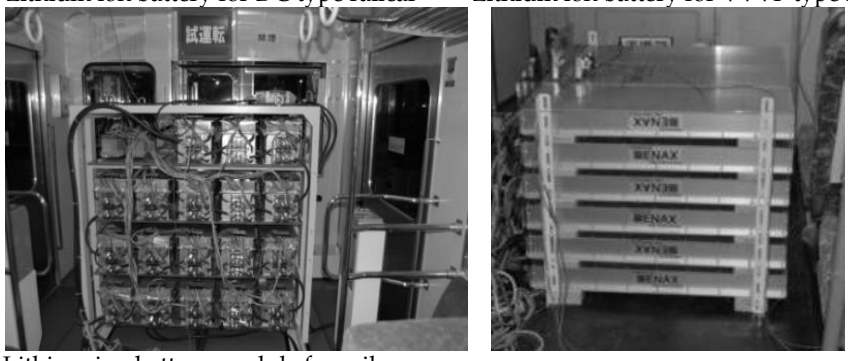

Fig. 4. Lithium ion battery module for railcar

Figure 4 shows large lithium ion battery module for DC type railcar and VVVF type railcar. Lithium ion battery module was consisted of 18 submodules. The submodule (200mm × 150mm × 700mm, 30kg, 84Ah, 34.2V) was made for DC type railcar. Laminate sheet cells which were connected in 9 series were connected in 12 parallels. The aluminium case was used to release a heat from the laminate sheet cell during the charge and discharge. Figure 5

shows the protection circuit and battery management system (BMS). The protection circuits and BMS were installed in all submodules to avoid the overcharge and overdischarge because the high safety must be kept during the running. The change of voltage in all cells was monitored by BMS and then the balance of voltage was adjusted. 18 submodules were connected in series to obtain 45kWh (84Ah, 615.6V) of lithium ion battery module with a weight of 540kg. The submodule (200mm × 50mm × 700mm, 10kg, 28Ah, 34.2V) was consisted of 36 laminate sheet cells for VVVF type railcar. Laminate sheet cells which were connected in 9 series were connected in 4 parallels. Similarly, the aluminium case was used to release a heat from the laminate sheet cells and the protection circuits were installed in all submodules. 18 submodules were connected in series to obtain 15kWh (28Ah, 615.6V) of lithium ion battery module with a weight of 180kg.

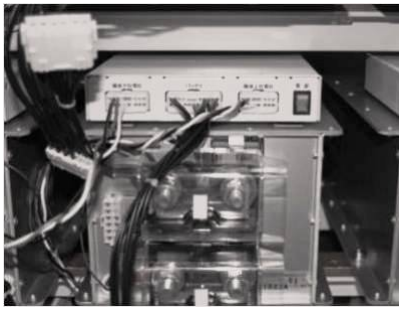

Fig. 5. BMS for lithium ion battery

3. Contact-wireless type railcar

3.1 DC type railcar

Various types of DC 600V type railcars (Echizen railway, Japan) with mechanical breaking system were used. Figure 6 (a) shows DC 600V type railcars with weight of 40t used in the running test. Lithium ion battery module was installed in the centre or front of the railcar and fixed in the exclusive rack in order to stand the vibration during the running. 45kWh and 60kWh of lithium ion battery module were used. Lithium ion battery module was directly connected with the motor of the railcar.

DC type railcar VVVF type railcar

Fig. 6. DC and VVVF type Railcar used for running test

3.2 VVVF type railcar

VVVF type railcar (Fukui railway, Japan) with the weight of 25t was used to examine the regenerative effect by lithium ion battery. Figure 6 (b) shows VVVF 600V type railcar with both regenerative breaking and mechanical breaking system. The regenerative breaking action changes to mechanical breaking at 40km/hr. 15 kWh of lithium ion battery module was installed in the front of the railcar and fixed in the wooden rack. Lithium ion battery module was connected with the inverter of the railcar.

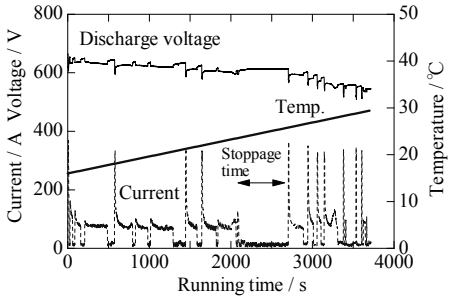

Fig. 7. Relations between running time and voltage, current, and temperature

4. Running test

4.1 Running test by DC type railcar

The running test of railcar with 45kWh lithium ion battery module was examined at Mikuni and Katsuyama business line of Echizen railway (Fukui city) in Japan. Mikuni business line was about 20km full length with a flat course and then railcar ran the one way only by lithium ion battery. Figure 7 shows the relations between running time and voltage, current and temperature on the flat course of the Mukuni line. The railcar ran for 20km when lithium ion battery module was discharged between 660V and 540V and this running included coasting and stopping several times. A current of 350A flowed to lithium ion battery module when the railcar was quickly accelerated. After accelerating, the current drastically decreased to about 80A, which was maintained continuously during running. After 3600s, the temperature of lithium ion battery module reached to 30°C. It was found that lithium ion battery module exhibited higher safety for the running.

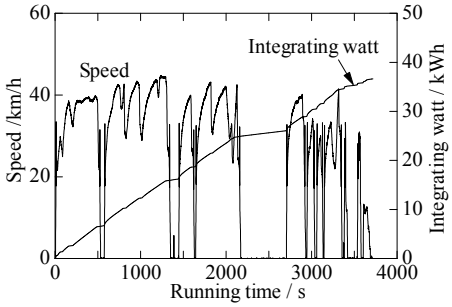

Fig. 8. Relation between running time and speed and integrating watt

Figure 8 shows the relation between running time and speed and integrating watt. On the running test, 37kWh electric power was consumed over 3600s of running and mileage was 0.54km/kWh.

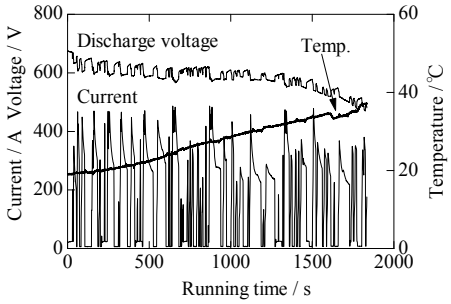

Fig. 9. Relations between running time and voltage, current, and temperature

By contrast, on an identical running test of a contact-wire railcar, 66kWh of electric power was consumed. The mileage was 0.3km/kWh. This poorer performance may result from not only loss of energy generated under power transmission from the substation but also power loss due to contact resistance between the contact-wire and pantograph. The use of the battery appeared to solve these problems. The running test of the railcar driven by a lithium ion battery indicated that its performance was comparable to that of contact-wire type railcar and that mileage was improved about two fold. Using the lithium ion battery, a running test under a condition of high load was also carried out on the Katsuyama line, which rises 150m on a sloping course with a 4% gradient. This running test used a 60kWh lithium ion battery module to which a 15kWh lithium ion battery module was added.

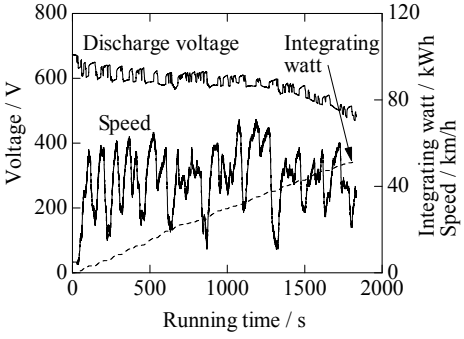

Fig. 10. Relation between running time and speed and integrating watt

Figure 9 shows the relations between running time and voltage, current and temperature on the Katsuyama business line. The railcar ran for 23km when lithium ion battery module was discharged between 660V and 490V. The current flowed at more than 400A when the railcar was quickly accelerated. After running for 23km, the temperature increased to around 40°C. Lithium ion battery module also exhibited higher safety for running with higher load.

Figure 10 shows the relations between running time and voltage, current, and temperature. On the test, 50kWh electric power was consumed over 1800s and mileage was 0.45km/kWh. 65km/h of maximum speed was recorded by the driving of lithium ion battery. For the contact-wire railcar, however, after running the same 23km course, 55kWh electric power was consumed and mileage was 0.41km/kWh. On this sloping course, the use of lithium ion battery module showed a 9% improvement in mileage. These results of running test suggest that lithium ion battery was expected as driving system of diesel car.

4.2 Running test by VVVF type railcar

Figure 11 shows the relation between running time and voltage, current and temperature after the running of VVVF type railcar with lithium ion battery. VVVF type railcar ran for 1.5km, while the power running, coasting and stopping were repeated in three times. A current of 300A flowed to lithium ion battery and the voltage was dropped when the railcar was quickly accelerated. When the current decreased down to about 200A, the rapid speed down was tried by using regenerative brake from 50km/hr to 40km/hr.

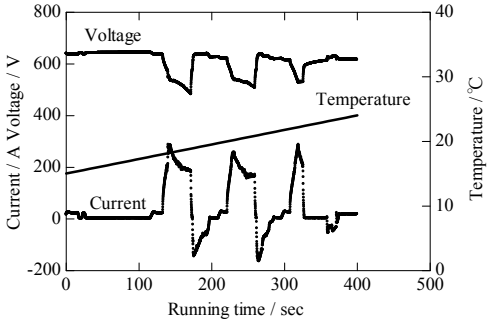

Fig. 11. Relations between running time and voltage, current, and temperature

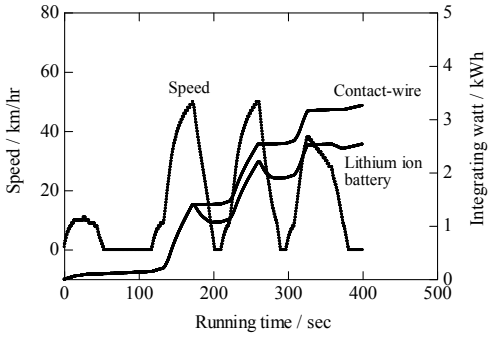

Fig. 12. Relation between running time and speed and integrating watt

The current of about -150A was obtained as regenerative energy. This suggested that 150A of regenerative energy was quickly charged to lithium ion battery by the regenerative brake. This means that lithium ion battery is charged at rate of 4.68C because 1C is equivalent to

32A. The temperature of lithium ion battery module increased from 17 to 25°C. It was found that the safety of lithium ion battery module could be maintained if the railcar was only used for the running of few km.
Figure 12 shows the change of speed and integrating watt after the running of VVVF type railcar by lithium ion battery and contact-wire. The maximum speed of 60km/hr was achieved in this work when VVVF type railcar was only derived by lithium ion battery. The integrating watt of lithium ion battery was 2.54kWh when VVVF type railcar ran for 1.5km while it repeatedly decelerated from 50km/hr by the regenerative brake. On the other hand, the electric power of 3.24kWh was consumed without lithium ion battery for the running of 1.5km. It was found that the energy-saving effect was about 22%.

4.3 Charging test from contact-wire

The quick battery charger apparatus (84Ah) which was received electric power from 600V contact-wire was developed. For charging test at constant current, lithium ion battery module which 80kWh of electric power was consumed after the running was used. The voltage of charge ranged from 550V to 660V. 80kWh of lithium ion battery module was charged up to SOC of 100% at 1C. Figure 13 the relation between charging time and voltage, current, temperature and integrating watt. After charging, the temperature of lithium ion battery module increased from 25°C to 33°C. It was found that 84Ah of lithium ion battery module could be charged at 600V safely.

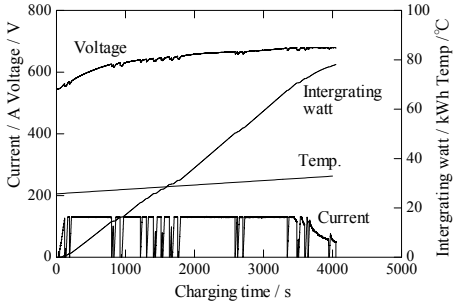

Fig. 13. Relation between charging time and voltage, current, temperature and intergrating watt

4.4 Rechargeable performance of lithium ion battery module

The rechargeable characteristics of lithium ion battery submodules were also examined after the running test for three years. The submodules were regularly charged for three years and 34V of voltage was maintained at room temperature. Figure 14 shows the relation between voltage and discharge capacity of lithium ion battery submodule at a rate of 1C. The initial discharge capacity of it was 34.2Ah, but decreased to 23.9Ah after three years. It was found that the discharge capacity of lithium ion battery submodule decreased to about 70% of initial discharge capacity. Lithium ion battery submodule had relatively high retention. The cycle performance of used submodule was examined at a rate of 1C under the charge condition on SOC of 80% and SOC of 100%.

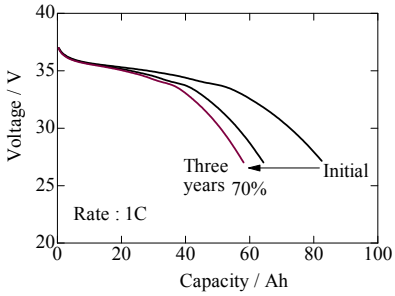

Fig. 14. Relation between voltage and capacity of submodule

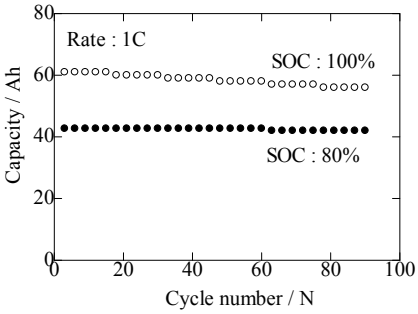

Fig. 15. Relation between capacity and cycle number of submodule at a rate of 1C

Figure 15 shows the relation between capacity and cycle number of used submodule. The capacity of submodule gradually decreased when the charge was carried out at SOC of 100%. On the other hand, the submodule exhibited high cycle stability at SOC of 80%. This result suggests that the full rechargeable is unfavourable to maintain high stability for large lithium ion battery module. The electric capacity may be lost to some extent, but the rechargeable of about 80% is desirable for the longer life cycle.

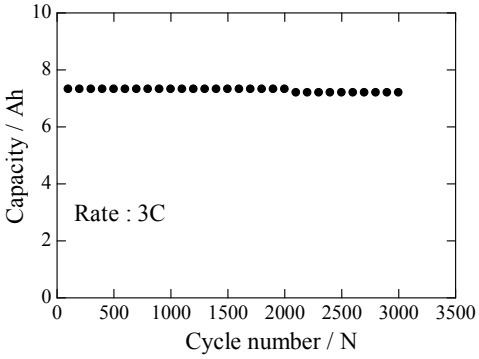

Fig. 16. Relation between capacity and cycle number of submodule at a rate of 3C (DOD 20%)

Figure 16 shows the cycle performance of used submodule was also examined by assuming the running of LRT with lithium ion battery in the road area. The distance of road area was 2km. 3000 times of cycle test was examined at room temperature. This means that 20% of DOD (depth of discharge) was continuously charged for 20min (3C) at every day for 24 month if lithium ion battery is charged at 4 times for one day from the service diagram of local railway. It was clear that the module had high stability for rechargeable. In the present circumstances, it was considered that the use of lithium ion battery was effective for the service diagram of local railway without high frequency.

5. Conclusion

Large lithium ion battery was developed for the running of railcar. Mn type lithium ion battery was used because of low cost and higher safety. LMP with high rechargeable performance were produced by large flame type spray pyrolysis. The laminate sheet type lithium ion cell was made using LMP. Various type large lithium ion battery modules consisted of submodule, in which laminate sheet type lithium ion cells were connected in series and parallel, were constructed.

The running test of DC and VVVF type railcar was carried out by using Mn type lithium ion battery at two business line of local railway in Japan. The results were obtained as follows;

(1) The running performance of railcar with lithium ion battery was equivalent to that of railcar which the electric power was supplied from contact-wire.

(2) Lithium ion battery had also the high running performance under a condition of high load.

(3) The high safety of lithium ion battery was maintained for the running of railcar.

(4) 22% of mileage was improved when the regenerative energy was charged by lithium ion battery during the running of VVVF inverter type railcar.

(5) The combination of lithium ion battery and VVVF inverter was effective for energy-saving of the railcar.

(6) The charge was performed at 600V safely by quick battery charger apparatus.

(7) The initial capacity of lithium ion battery decreased to 30% after the running test for three years.

(8) The used submodule exhibited excellent cycle stability.

6. References

Sameshima, H., Ogasa, M. & Yamamoto, T. (2004). On-board Characteristics of Rechargeable Lithium Ion Batteries for Improving Energy Regenerative Efficiency, *Quarterly Report of RTRI*, 45, 45-52

Ogasa, M. & Taguchi, Y. (2007). Power Flow Control for Hybrid Electric Vehicles Using Trolley Power and On-board Batteries, *Quarterly Report of RTRI*, 48, 30-36

Ozawa, H., Ogihara, T., Mukoyama, I., Myojin, K., Aikiyo, H., Okawa, T. & Harada, A. (2007). Synthesis of Lithium Manganate Powders by Spray Pyrolysis and its Application to Lithium Ion Battery for Tram, *W.E.V.A. J.*, 1, 19-22

Ozawa, H. & Ogihara, T., (2008). Running Test of Contactwire-less Tramcar Using Lithium Ion Battery, *IEEJ Trans.*, 3, 360-362

Mukoyama, I., Myojin, K., Ogihara, T., Ogata, N., Uede, M., Ozawa, H. & Ozawa, K. (2006). Large-Scale Synthesis and Electrochemical Properties of $LiAl_XMn_{2-X}O_4$ Powders by Internal Combustion Type Spray Pyrolysis Apparatus Using Gas Burner, *Electroceramics in Japan*, 9, 251-24